Supplementary Information for:

A framework for accessing elusive intermediate-sized Pd_nL_{2n} (n = 8, 9) metal-organic cages

Connor P. Bergin, [‡a] Daniel J. C. Murchie, [‡a] Stephen P. Argent,[a] Soumalya Bhattacharyya,[a*] and Ben S. Pilgrim[a*]

[a]*School of Chemistry, University of Nottingham, University Park, Nottingham, NG7 2RD, UK*

*E-mail: soumalya.bhattacharyya@nottingham.ac.uk
ben.pilgrim@nottingham.ac.uk

Contents

S1 Reagents and general materials

All chemicals and dry solvents were purchased from Sigma-Aldrich or Fluorochem. Commercial solvents and reagents were used without further purification unless specified. Bottles of $Pd(NO_3)_2•2H_2O$ were observed to degrade slightly over time, even when stored in a desiccator since it is highly hydroscopic; best results were obtained with fresh bottles of $Pd(NO_3)_2•2H_2O$. Flash column chromatography was performed using silica gel high purity grade (pore size 60 Å, 230–400 mesh particle size, Sigma-Aldrich). Automated flash column chromatography was performed using a CombiFlash NextGen 300 Automated Flash Chromatography System, with a UV-Vis detector 200-800 nm with PeakTrak software control, with a flow rate range of 1-300 mL min^{-1} and a maximum pressure limit of 160 psi (11 bar). RediSep silver disposable flash silica columns were used to purify compounds. TLC analyses were performed on Merck TLC silica gel 60 F_{254} plates. Product spots were visualised under UV light (λ_{max} = 254 nm). Centrifugation was carried out on a Grant-bio LMC-3000 or a Corning Mini Microcentrifuge. All reactions were stirred with magnetic followers.

S2 Characterisation and analysis methods

S2.1 NMR spectroscopy

NMR spectra were recorded at 298 K using Bruker Avance(III) 500 or 400 spectrometers (^{1}H, 500 / 400 MHz; ^{13}C[^{1}H] and ^{13}C[^{19}F], 125 / 101 MHz; ^{19}F, 376 MHz). Spectrometers were automatically tuned and matched to the correct operating frequencies. Routine ^{1}H NMR characterisation was carried out using a zg30 pulse program (30° pulse). ^{1}H and ^{13}C spectra were referenced to the residual solvent peaks for DMSO (^{1}H: 2.50 ppm, ^{13}C: 39.53 ppm) or CH_3CN (^{1}H: 1.94 ppm, ^{13}C: 1.30 ppm and 118.30 ppm). ^{19}F spectra were referenced using a sealed capillary of C_6F_6 in DMSO-d_6 added to the NMR tube (^{19}F: −164.90 ppm). Deuterated dimethylsulfoxide (DMSO-d_6) was obtained from Fluorochem and used without any further purification. Deuterated acetonitrile (CD_3CN) was obtained from Sigma Aldrich and used without any further purification. NMR signals are reported in terms of chemical shift (δ) in parts-per-million (ppm), multiplicity, coupling constants (in Hz), and relative integral in that order. The following abbreviations for multiplicity are used: s, singlet; d, doublet; t, triplet; qu, quartet; qn, quintet; m, multiplet; br, broad. Where spectra have been assigned this has been done on accompanying figures. Spectra were digitally processed (phase and baseline corrections, integration, peak analysis) using Mestrenova. DOSY NMR experiments were performed on 5 mm BBO probe and Standard QUAD Probe on a Bruker Avance(III) 500 MHz NMR spectrometer. Gradient strength was between 1.73 and 17.5 G/cm. DOSY measurements were performed using the standard pulse program, dstebpgp3s, employing a stimulated echo and longitudinal eddy-current delay (LED) using bipolar gradient pulses for diffusion using two spoil gradients. SinE.100 gradients were used. Diffusion times Δ = 200 ms and δ = 2000 µs were used for the experiments. The size of fid = 32. Raw DOSY data were processed using the Peak fit DOSY transform programme in Mestrenova.

S2.2 Mass spectrometry

High resolution electrospray ionisation (ESI) mass spectra were obtained on a Bruker ESI-TOF MicroTOF II spectrometer or a Bruker Impact II. The exported raw data were processed on Data Analysis software to access them in a .csv format, which then was used to plot in OriginPro. For the cage samples in DMSO, the solution was diluted with CH_3CN up until 8:1, CH_3CN:DMSO (v/v) was reached before subjecting them to ESI.

S2.3 Access to raw data

Raw data are available upon reasonable request to the corresponding author Dr Ben Pilgrim ben.pilgrim@nottingham.ac.uk.

S3 Ligand reference chart

S3.1 Ligand reference chart

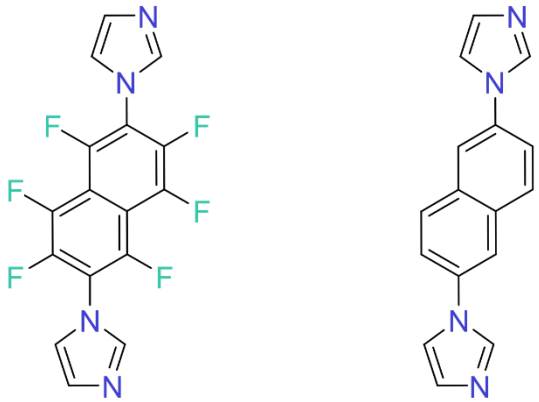

L^1 L^2

Figure S1: Ligand reference chart

S4 Ligand synthesis and characterisation

S4.1 Synthesis of 1,1'-(perfluoronaphthalene-2,6-diyl)bis(1H-imidazole), L^1

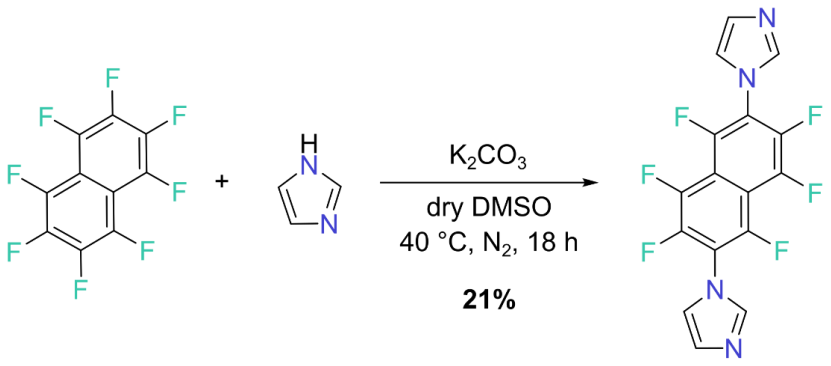

L^1

Under a nitrogen atmosphere, octafluoronapthalene (544 mg, 2.00 mmol), imidazole (340 mg, 5.00 mmol) and potassium carbonate (691 mg, 5.00 mmol) were suspended in dry DMSO (25 mL). The reaction mixture was heated at 40 °C for 18 h then filtered. The filtrate was poured onto crushed ice (10 g). After the ice had melted, the mixture was extracted with CH_2Cl_2 (300 mL) and the organics washed with brine (100 mL) to remove the remaining DMSO. The organics were dried over Na_2SO_4, filtered, and the solvent removed *in vacuo*. The crude mixture was purified by flash column chromatography using gradient elution from CH_2Cl_2 to CH_2Cl_2:THF (4:1) to yield ligand **L^1** as a white powder (157 mg, 0.426 mmol, 21%).

^{1}H NMR (400 MHz, DMSO-d_6) δ_H: 8.16 (s, 2H), 7.69 (s, 2H), 7.26 (s, 2H).

^{19}F NMR (376 MHz, DMSO-d_6) δ_F: −131.58 (m, 2F), −145.62 (m, 2F), −148.88 (m, 2F).

^{1}H NMR (400 MHz, CD_3CN) δ_H: 7.89 (s, 2H), 7.44 (s, 2H), 7.25 (s, 2H).

^{19}F NMR (376 MHz, CD_3CN) δ_F: −130.52 (m, 2F), −145.45 (m, 2F), −147.74 (m, 2F).

^{13}C[^{1}H] NMR (125 MHz, DMSO-d_6) δ_C: 146.4 (d, J = 258.3 Hz), 142.4 (dd, J = 251.9, 14.3 Hz), 140.7 (dm, J = 253.5 Hz), 138.5, 129.5, 121.2, 116.5 (t, J = 14.9 Hz), 109.8 (m)

^{13}C[^{19}F] NMR (125 MHz, DMSO-d_6) δ_C: 146.4, 142.4, 140.7, 138.5 (ddd, J = 216.2, 10.7, 6.2 Hz), 129.5 (dt, J = 191.2, 10.9 Hz), 121.2 (ddd, J = 196.0, 17.2, 3.0 Hz), 116.5, 109.8.

ESI-MS (ESI, MeOH), *m/z*: calculated for $[M+H]^+$, $[C_{16}H_6F_6N_4]^+$, 369.0569 found 369.0563.

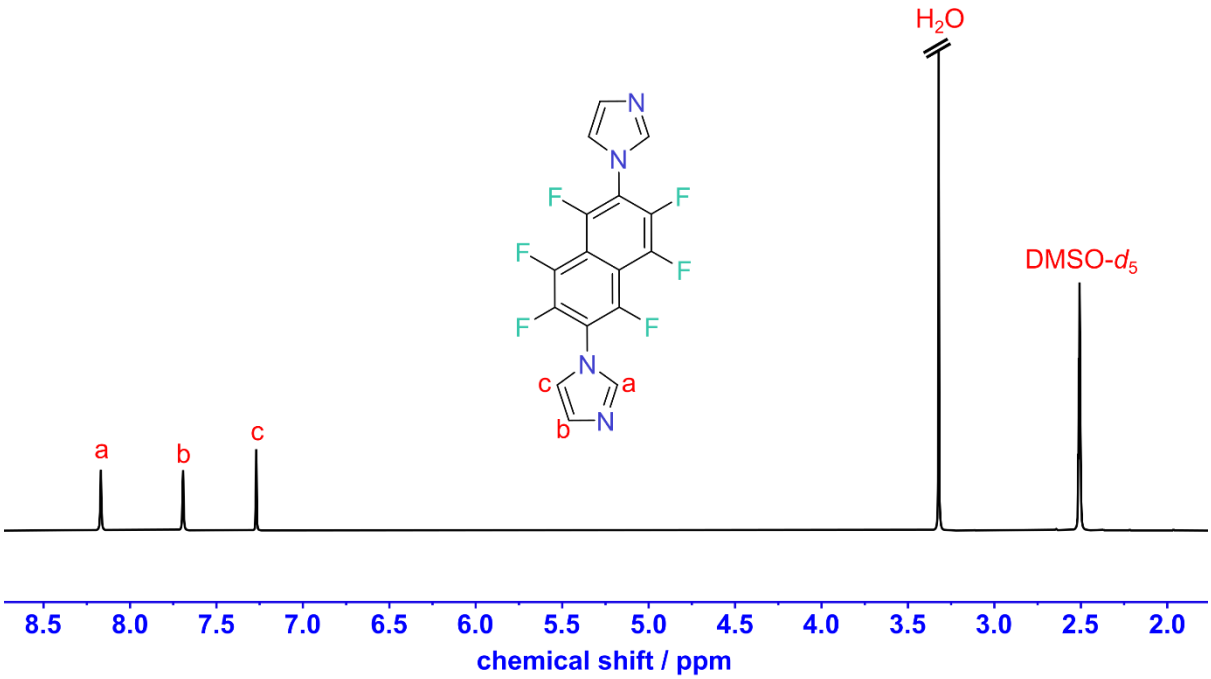

Figure S2: ^{1}H NMR spectrum of **L^{1}**
(400 MHz, 298 K, DMSO-d_6)

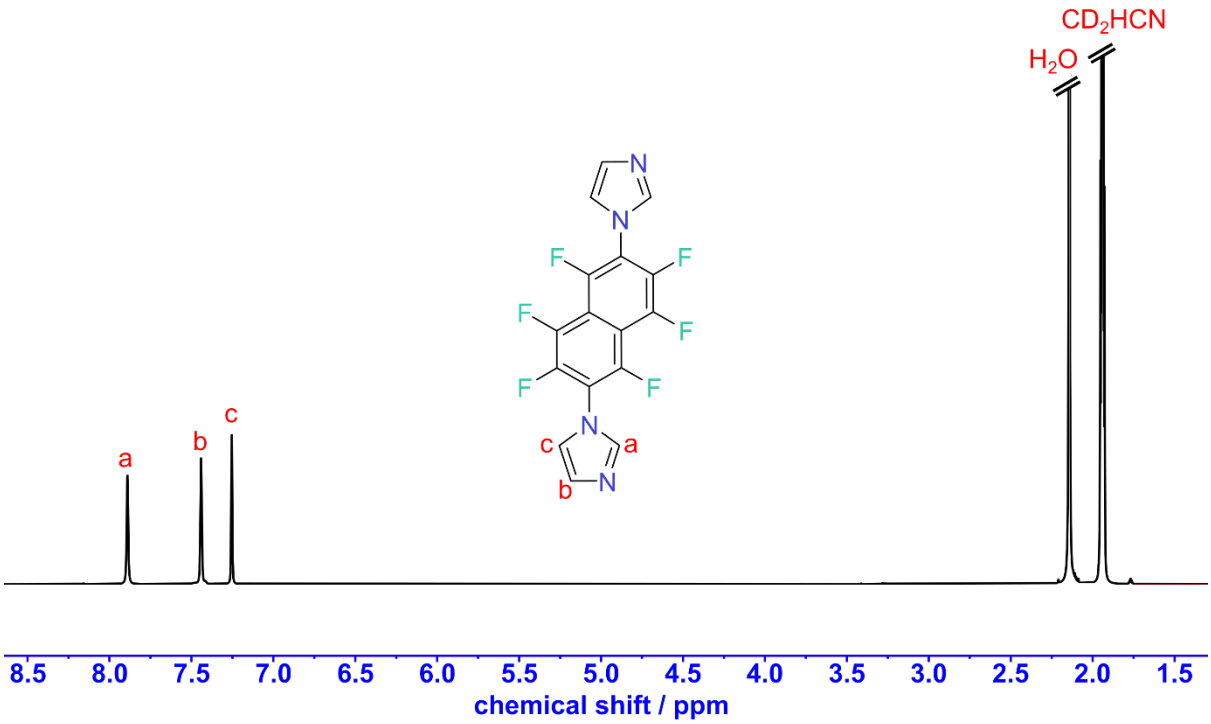

Figure S3: ^{1}H NMR spectrum of **L^{1}**
(400 MHz, 298 K, CD_3CN)

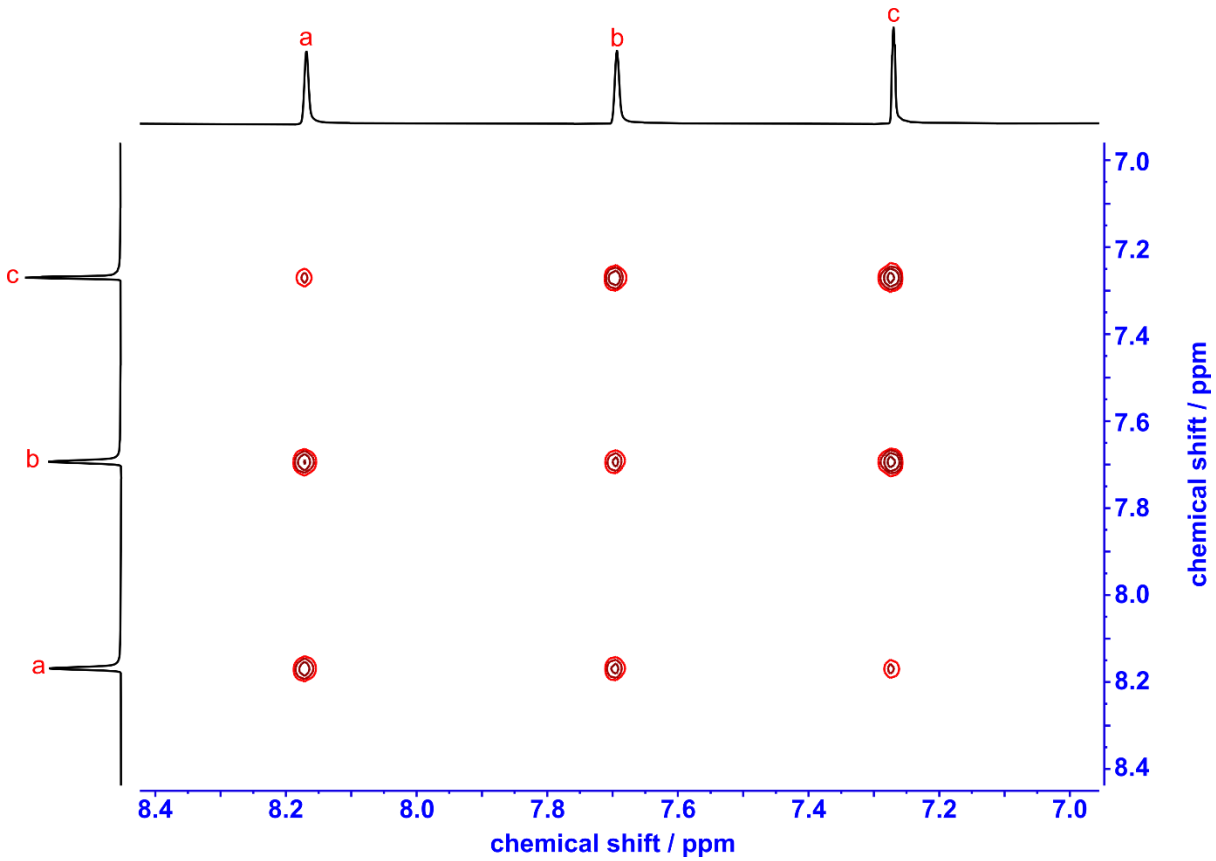

Figure S4: ^{1}H-^{1}H COSY spectrum of **L^{1}**
(500 MHz, 298 K, DMSO-d_6)

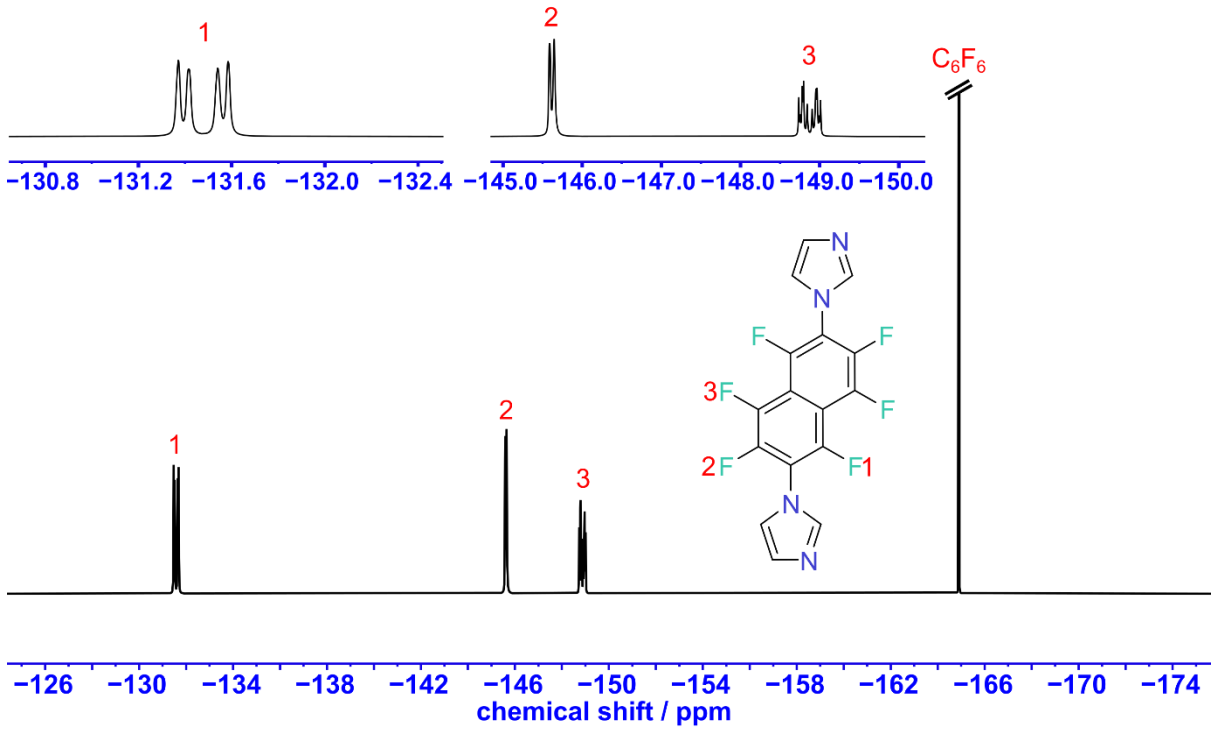

Figure S5: ^{19}F NMR spectrum of **L^{1}**
(376 MHz, 298 K, DMSO-d_6)

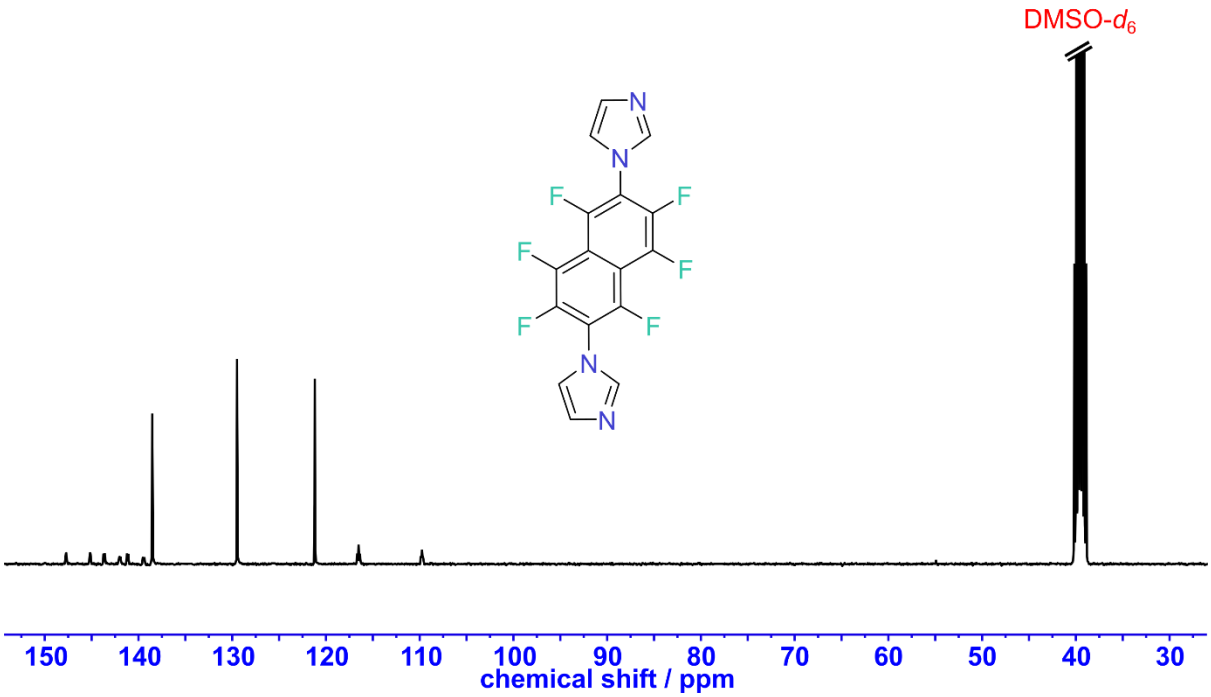

Figure S6: $^{13}C[^{1}H]$ NMR spectrum of **L¹**
(125 MHz, 298 K, DMSO-d_6)

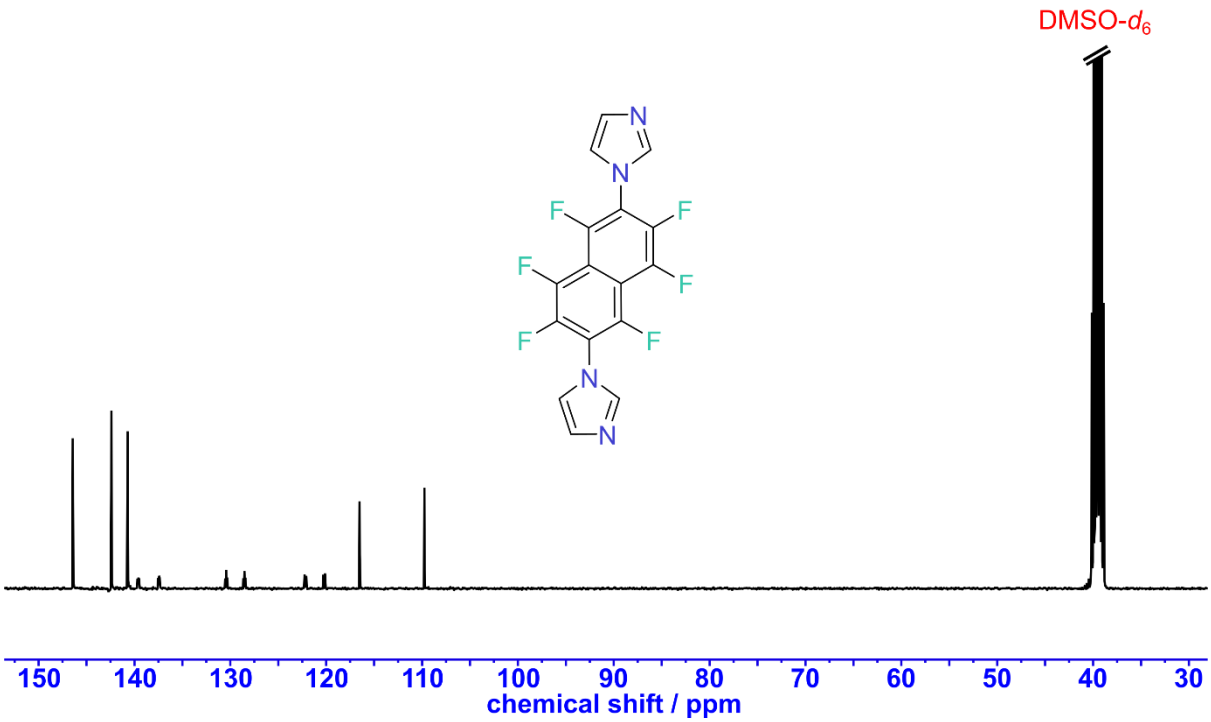

Figure S7: $^{13}C[^{19}F]$ NMR spectrum of **L¹**
(101 MHz, 298 K, DMSO-d_6)

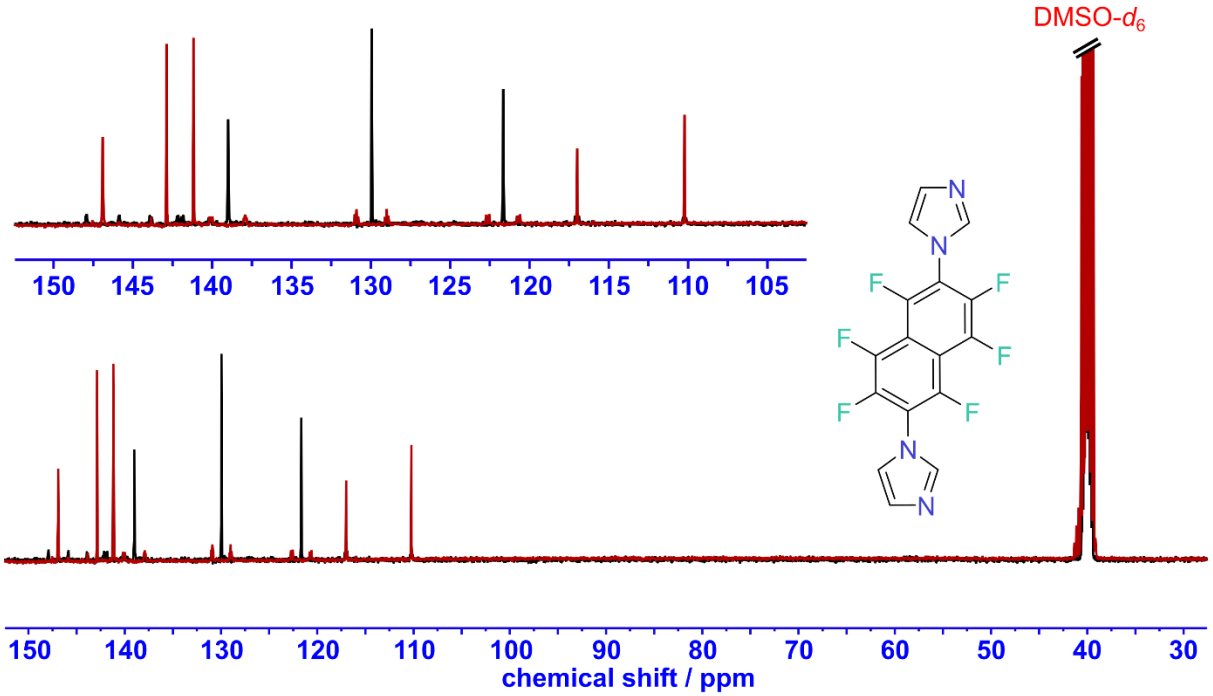

Figure S8: Superimposed plot of $^{13}C[^{19}F]$ NMR spectrum (red) (101 MHz, 298 K, DMSO-d_6) and $^{13}C[^{1}H]$ NMR spectrum (black) (125 MHz, 298 K, DMSO-d_6) of **L^1**

S4.2 Synthesis of 2,6-di(1H-imidazol-1-yl)naphthalene, L^2

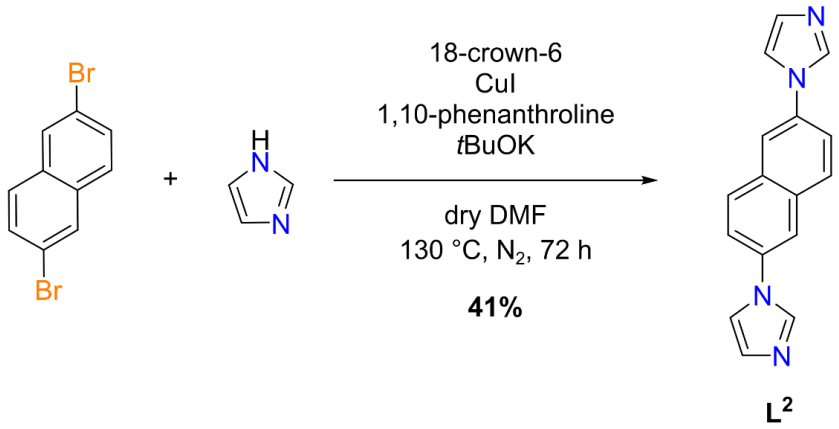

L^2

A flame-dried 100 mL two-necked round bottom flask was charged with CuI (133 mg, 0.70 mmol), 1,10-phenanthroline (252 mg, 1.40 mmol), and dry DMF (12 mL). The mixture was degassed via freeze-pump-thaw degassing. The brown solution was heated to 120 °C and stirred for 5 min under a nitrogen atmosphere. 2,6-Dibromonapthalene (1.00 g, 3.50 mmol), imidazole (1.90 g, 28.0 mmol), potassium *tert*-butoxide (3.45 g, 28.0 mmol) and a pinch of 18-crown-6 were added, and the mixture was heated at 130 °C for 72 h under a nitrogen atmosphere. After completion, the brown residue was stirred with 100 mL of ice-cold water for 10 min before being filtered. The residue was extracted with 300 mL of CH_2Cl_2 and washed with brine. The organics were collected over Na_2SO_4, filtered, and the solvent removed *in vacuo*. The crude mixture was purified by Flash silica gel column chromatography with CH_2Cl_2:MeOH (95:5) as the eluent. Finally, the solid was washed Et_2O (15 mL × 3) to remove excess 18-crown-6 to afford 2,6-di(1H-imidazol-1-yl)naphthalene, **L^2**, as a pale-brown coloured solid (375 mg, 1.44 mmol, 41%).

^{1}H NMR (500 MHz, DMSO-d_6) δ_H: 8.43 (s, 2H), 8.29 (d, J = 2.3 Hz, 2H), 8.13 (d, J = 8.8 Hz, 2H), 7.96 (dd, J = 8.7, 2.3 Hz, 2H), 7.91 (s, 2H), 7.19 (s, 2H).

^{1}H NMR (500 MHz, CD_3CN) δ_H: 8.12 (s, 2H), 8.11-8.10 (m, 4H), 7.80 (dd, J = 8.8, 2.2 Hz, 2H), 7.63 (s, 2H), 7.20 (s, 2H).

^{13}C NMR (125 MHz, DMSO-d_6) δ_C: 136.2, 135.0, 132.2, 130.6, 130.2, 121.3, 118.6, 117.8.

HRMS (ESI, MeOH), *m/z*: calc for $[M+H]^+$, $[C_{33}H_{27}N_7]^+$, 261.1096, found 261.1140.

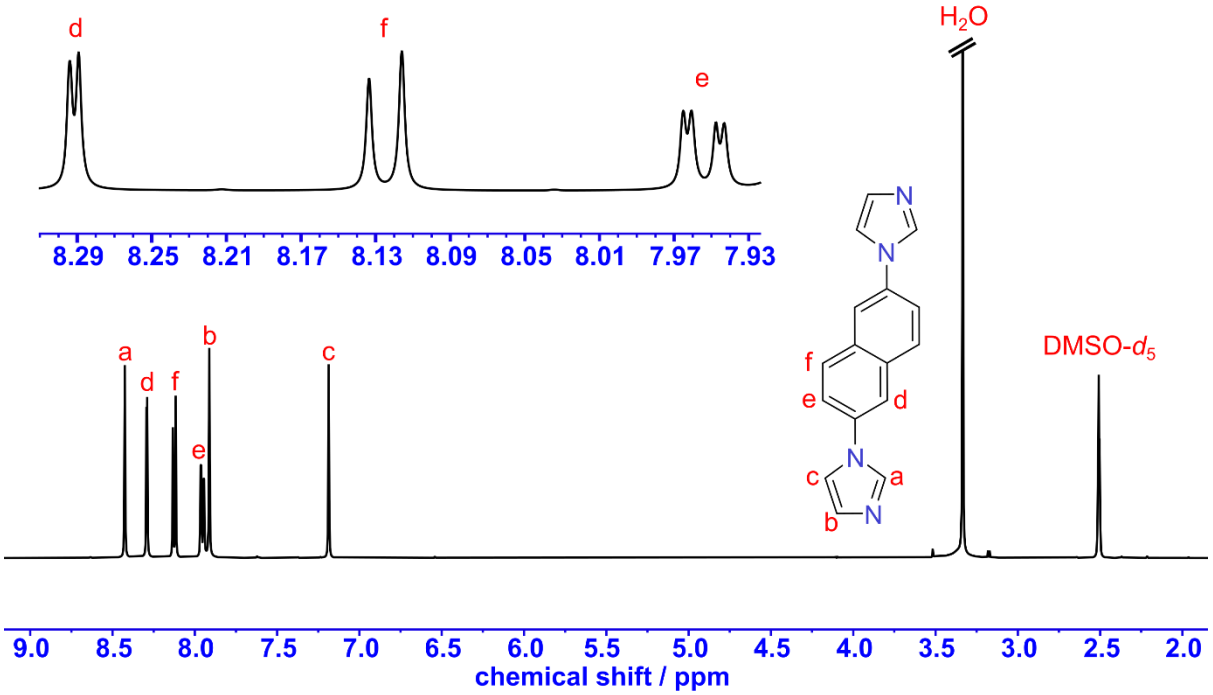

Figure S9: ^{1}H NMR spectrum of **L²**
(500 MHz, 298 K, DMSO-d_6)

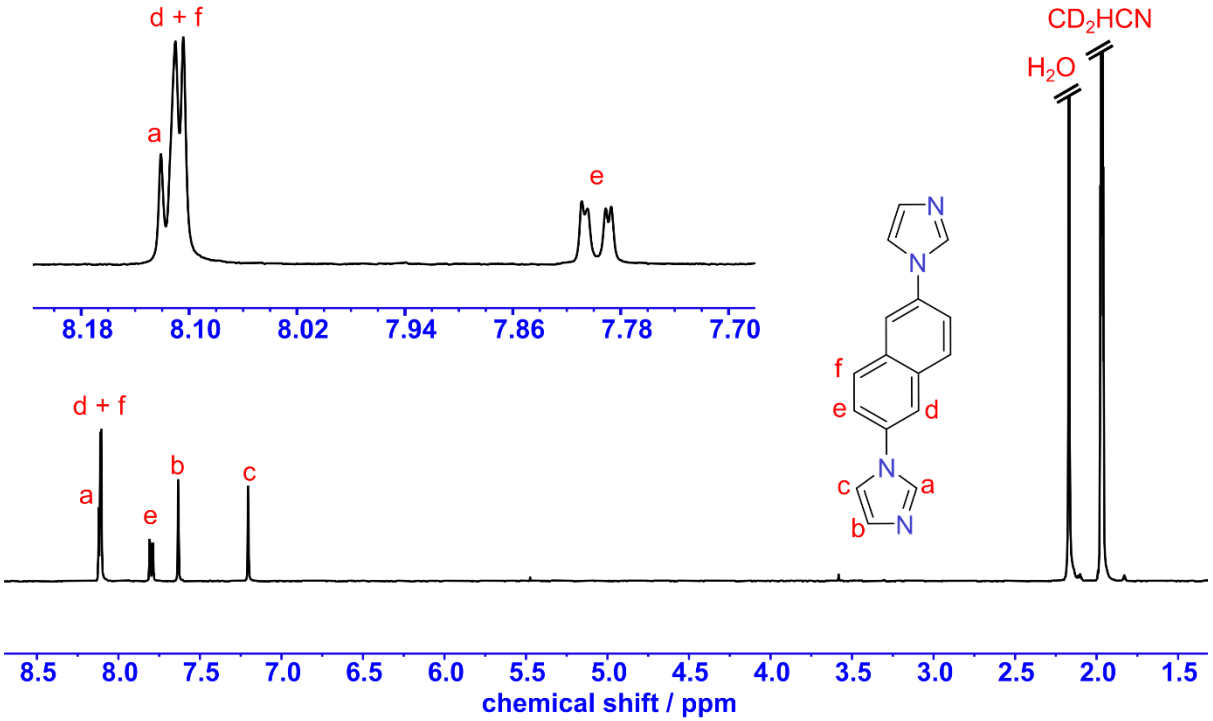

Figure S10: ^{1}H NMR spectrum of **L²**
(500 MHz, 298 K, CD_3CN)

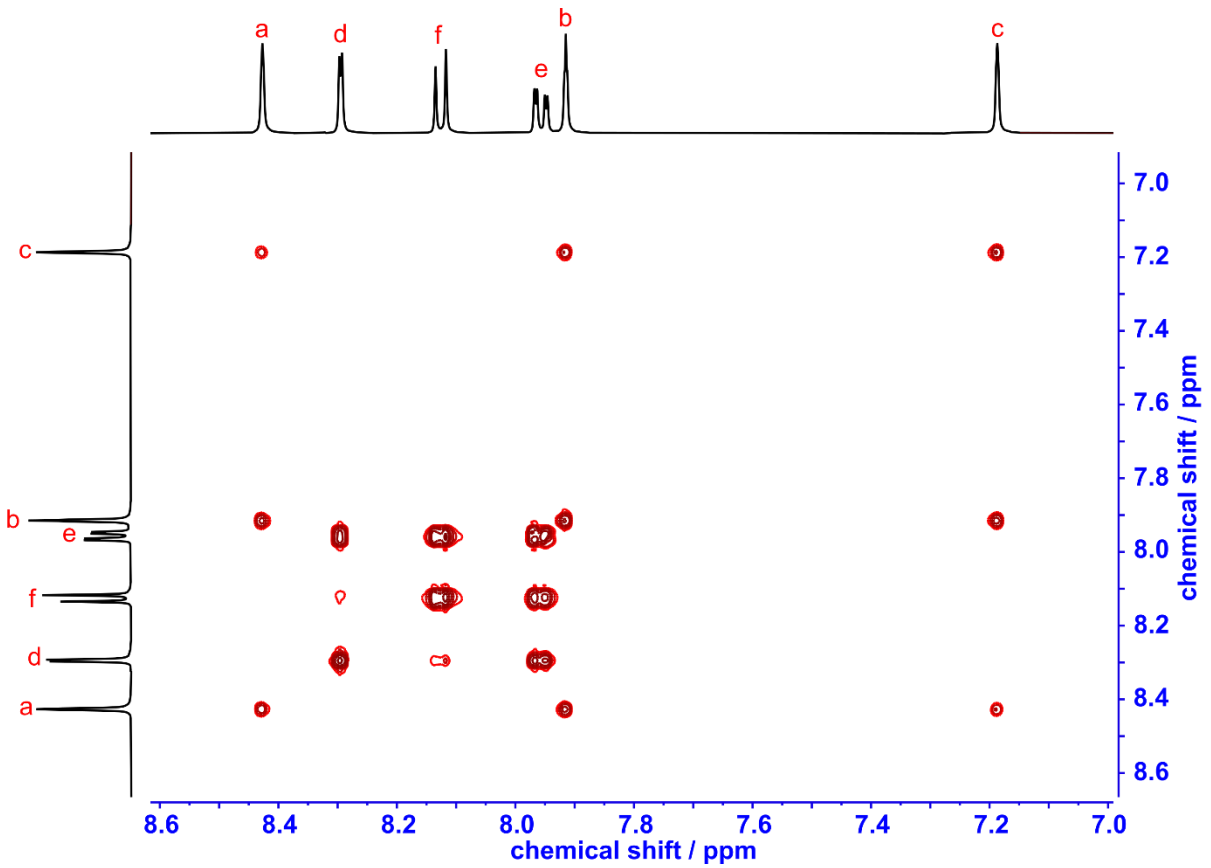

Figure S11: ^{1}H-^{1}H COSY spectrum of **L²**
(500 MHz, 298 K, DMSO-d_6)

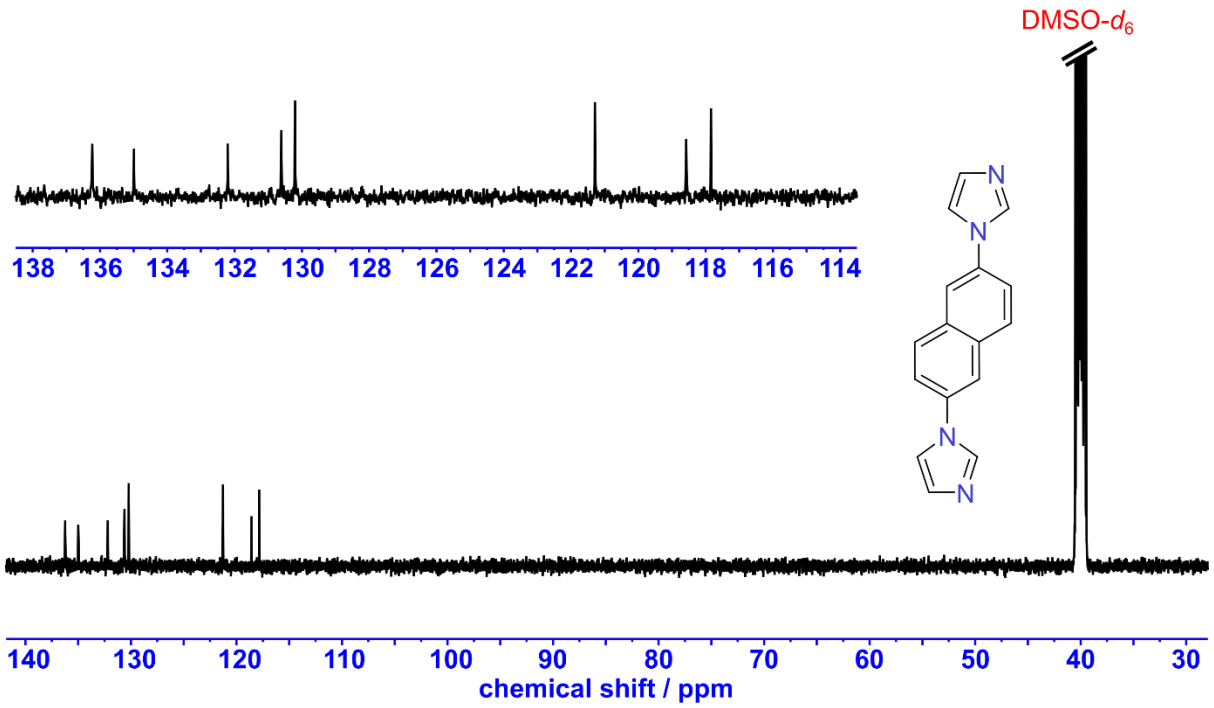

Figure S12: ^{13}C[^{1}H] NMR spectrum of **L²**
(125 MHz, 298 K, DMSO-d_6)

S5 Synthesis and characterisation of metal-organic cages

S5.1 Self-assembly of $Pd_8L^1_{16}$ square antiprism 1

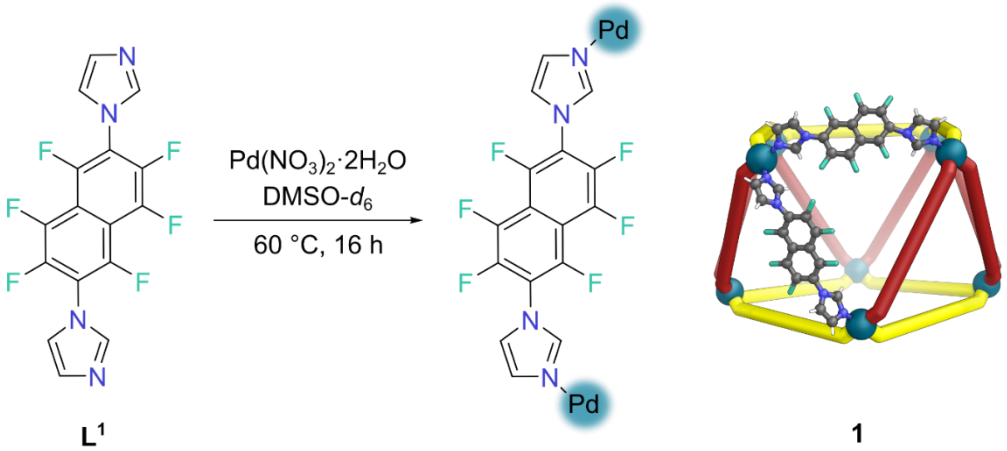

L[1] **1**

1,1'-(Perfluoronaphthalene-2,6-diyl)bis(1H-imidazole) (**L**[1]) (5.00 mg, 0.0136 mmol) and $Pd(NO_3)_2{\cdot}2H_2O$ (1.81 mg, 0.00679 mmol) were placed in a 1-dram (4.00 mL) vial and 0.60 mL DMSO-d_6 was added. This mixture was then stirred at 60 °C for 16 h. The resulting reaction mixture was centrifuged (3000 rpm, 5 min) and the supernatant decanted to obtain a pale-yellow solution of cage **1**.

^{1}H NMR (400 MHz, DMSO-d_6) δ_H: 9.13 (s, 16H, a), 8.90 (s, 16H, a'), 8.08 (s, 16H, b'), 7.96 (s, 16H, c'), 7.95 (s, 16H, b), 7.60 (s, 16H, c).

^{19}F NMR (376 MHz, DMSO-d_6) δ_F: −129.96 to −130.48 (m, 32F), −144.87 to −145.67 (m, 32F), −148.26 to −149.12 (m, 32F).

ESI-MS (ESI, DMSO), *m/z*: [**1**$(NO_3)_{11}]^{5+}$ calculated 1484.9811, found 1484.9844 [**1**$(NO_3)_{10}]^{6+}$ calculated 1227.1530, found 1227.1576; [**1**$(NO_3)_9]^{7+}$ calculated 1042.9900, found 1042.9929; [**1**$(NO_3)_8]^{8+}$ calculated 904.8678, found 904.8710; [**1**$(NO_3)_7]^{9+}$ calculated 797.4394, found 797.4420.

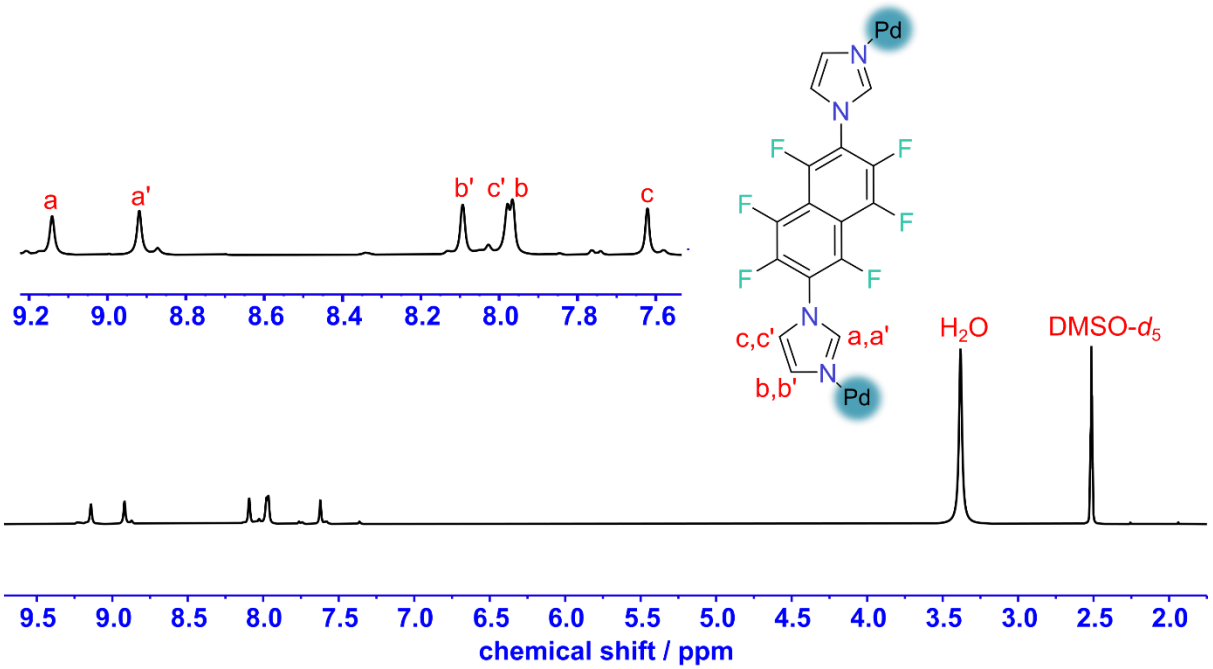

Figure S13: ^{1}H NMR spectrum of cage **1**
(400 MHz, 298 K, DMSO-d_6)

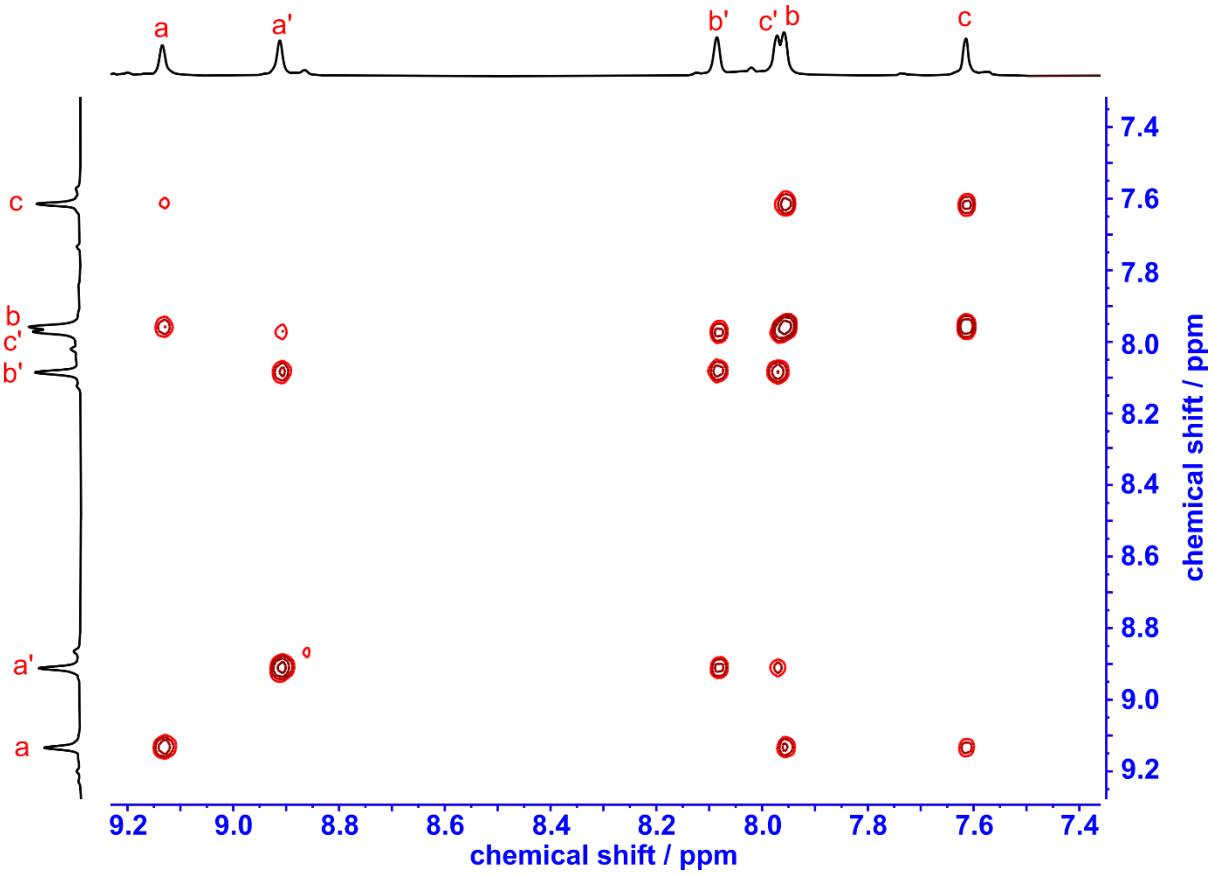

Figure S14: ^{1}H-^{1}H COSY spectrum of cage **1**
(400 MHz, 298 K, DMSO-d_6)

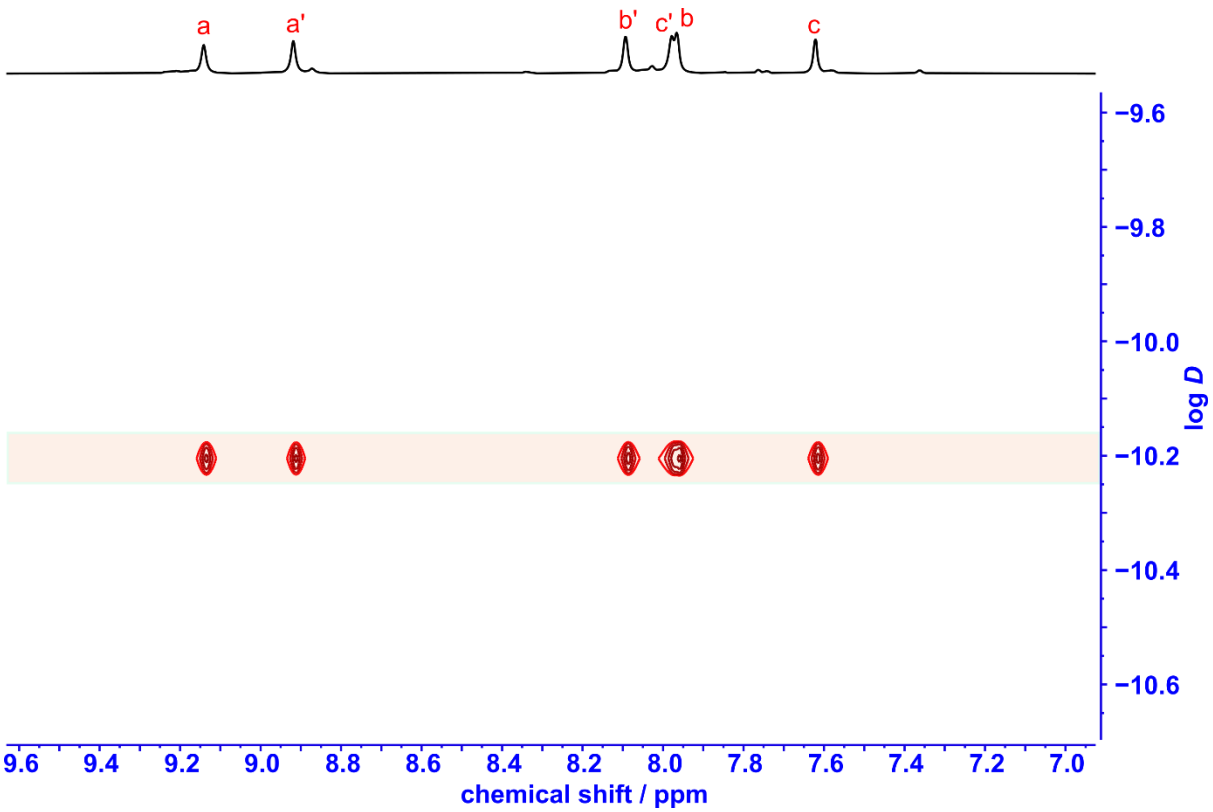

Figure S15: ^{1}H DOSY spectrum of cage **1**
(400 MHz, 298 K, DMSO-d_6)

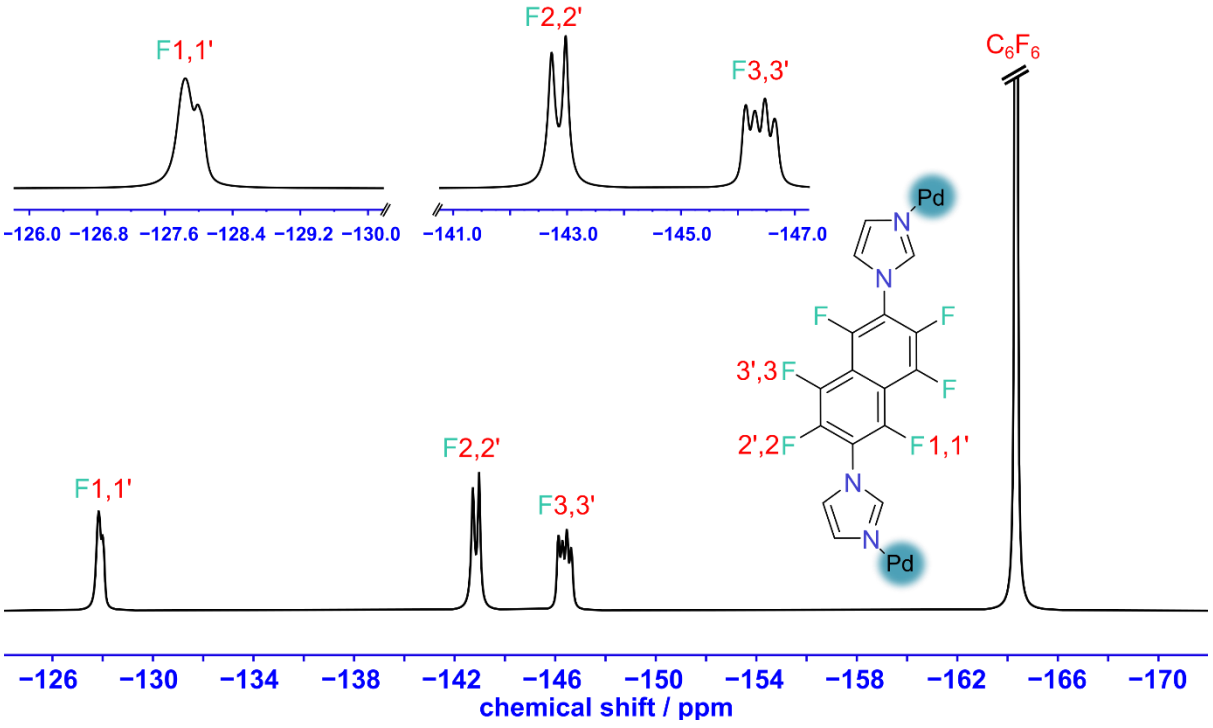

Figure S16: ^{19}F NMR spectrum of cage **1**
(376 MHz, 298 K, DMSO-d_6)

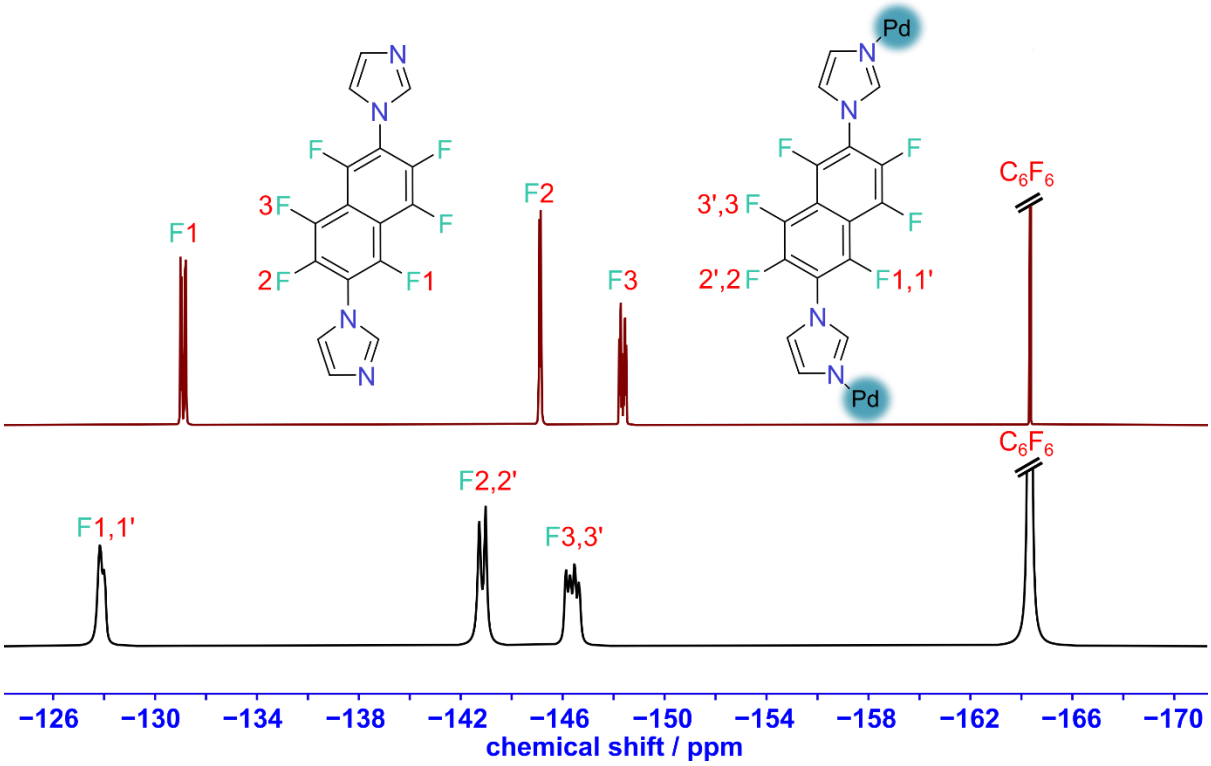

Figure S17: Stack plot of ^{19}F NMR spectra of ligand **L**^{1} (maroon) and cage **1** (black) (376 MHz, 298 K, DMSO-d_6)

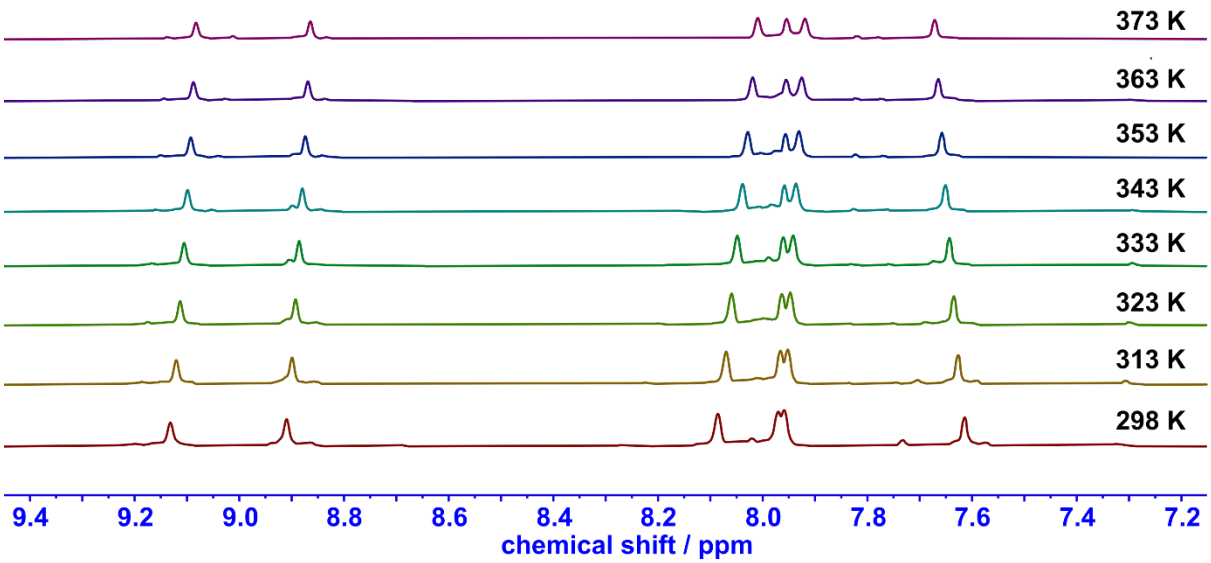

Figure S18: Variable temperature ^{1}H NMR spectra of a sample of cage **1**, which had settled to an equilibrium composition after 1 week. (400 MHz, 298 K, DMSO-d_6)

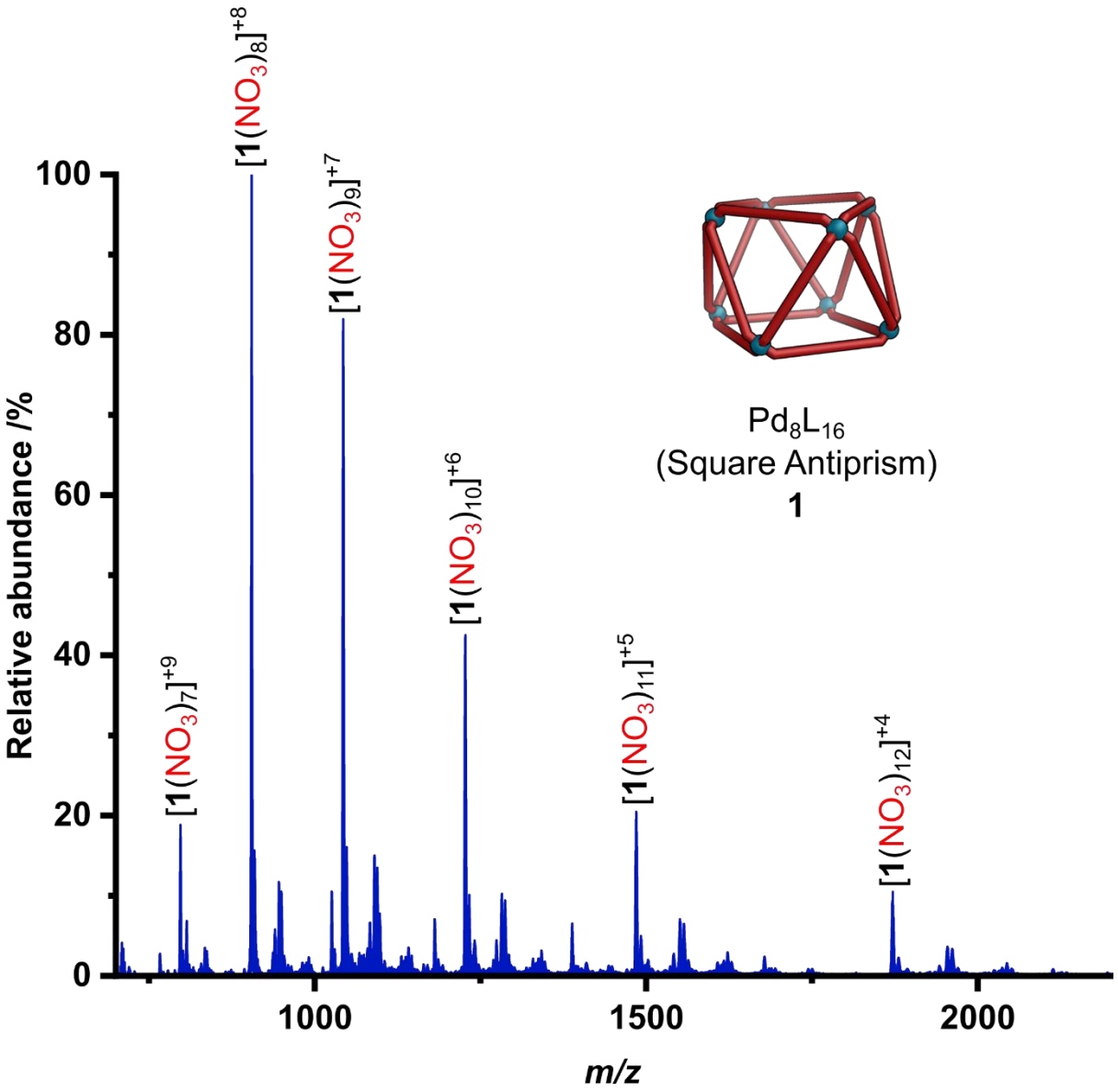

Figure S19: ESI-MS of cage **1**

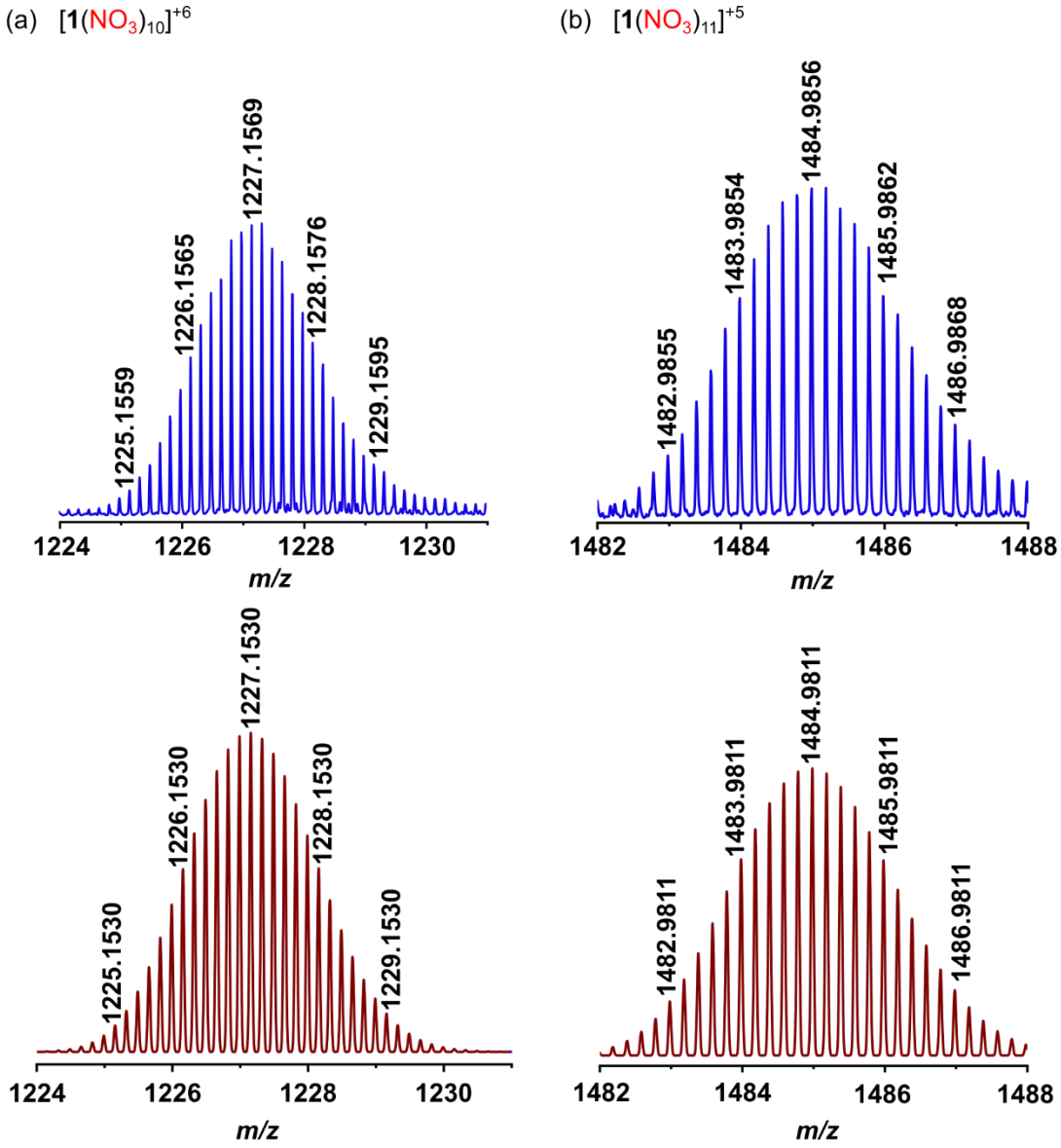

Figure S20: Isotopic distribution of selected peaks from cage **1** showing match between experimentally observed (blue) and predicted (red) patterns
(a) $[\mathbf{1}(NO_3)_{10}]^{+6}$, (b) $[\mathbf{1}(NO_3)_{11}]^{+5}$

S5.2 Self-assembly of $Pd_8L^2_{16}$ square antiprism 2 and $Pd_9L^2_{18}$ tricapped trigonal prism 2'

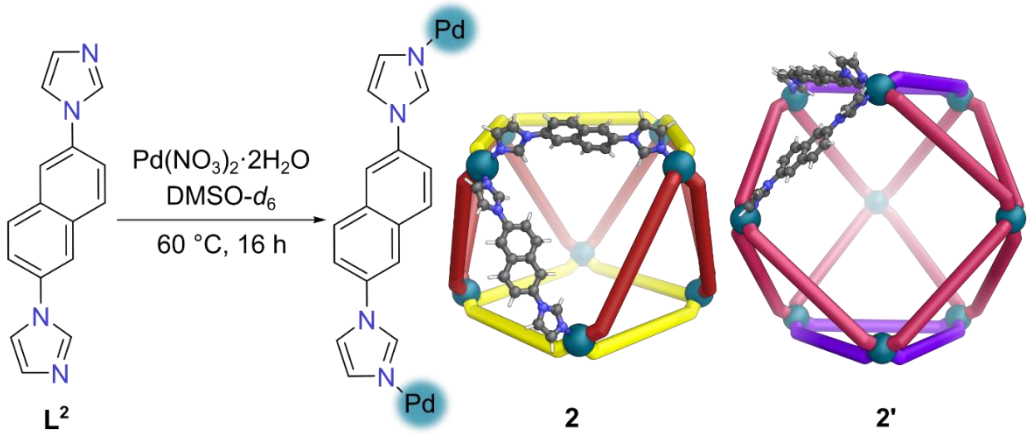

2,6-Di(1H-imidazol-1-yl)naphthalene (**L²**) (5.00 mg, 0.0192 mmol) and $Pd(NO_3)_2{\cdot}2H_2O$ (2.56 mg, 0.00961 mmol) were placed in a 1-dram (4.00 mL) vial and 0.60 mL DMSO-d_6 was added. This mixture was then stirred at 60 °C for 16 h. The resulting reaction mixture was centrifuged (3000 rpm, 5 min) and the supernatant decanted to obtain a brown solution of cages **2** and **2'**.

Cage 2:

^{1}H NMR (500 MHz, DMSO-d_6) δ_H: 9.42 (s, 16H, a), 9.23 (s, 16H, a'), 8.43-7.95 (m, 96H, naphthalene), 8.24 (s, 16H, b'), 8.03 (s, 16H, b), 7.88 (s, 16H, c'), 7.50 (s, 16H, c).

ESI-MS (ESI, DMSO), *m/z*: [**2**$(NO_3)_{11}]^{5+}$ calculated 1139.5620, found 1139.5657; [**2**$(NO_3)_{10}]^{6+}$ calculated 939.3037, found 939.3047; [**2**$(NO_3)_9]^{7+}$ calculated 796.2621, found 796.2655; [**2**$(NO_3)_8]^{8+}$ calculated 688.9808, found 688.9928.

Cage 2':

^{1}H NMR (500 MHz, DMSO-d_6) δ_H: 9.42 (s, 12H, a), 9.25 (s, 12H, a'), 9.15 (s, 12H, a*), 8.43-7.95 (m, 108H, naphthalene), 8.20 (s, 12H, b*), 8.17 (s, 12H, b'), 8.15 (s, 12H, b), 7.87 (s, 12H, c*), 7.63 (s, 12H, c), 7.63 (s, 12H, c').

ESI-MS (ESI, DMSO), *m/z*: [**2'**$(NO_3)_{13}]^{5+}$ calculated 1289.7808, found 1289.7843; [**2'**$(NO_3)_{12}]^{6+}$ calculated 1064.4860, found 1064.4902; [**2'**$(NO_3)_{11}]^{7+}$ calculated 903.5612, found 903.5638; [**2'**$(NO_3)_{10}]^{8+}$ calculated 782.8675, found 782.8697.

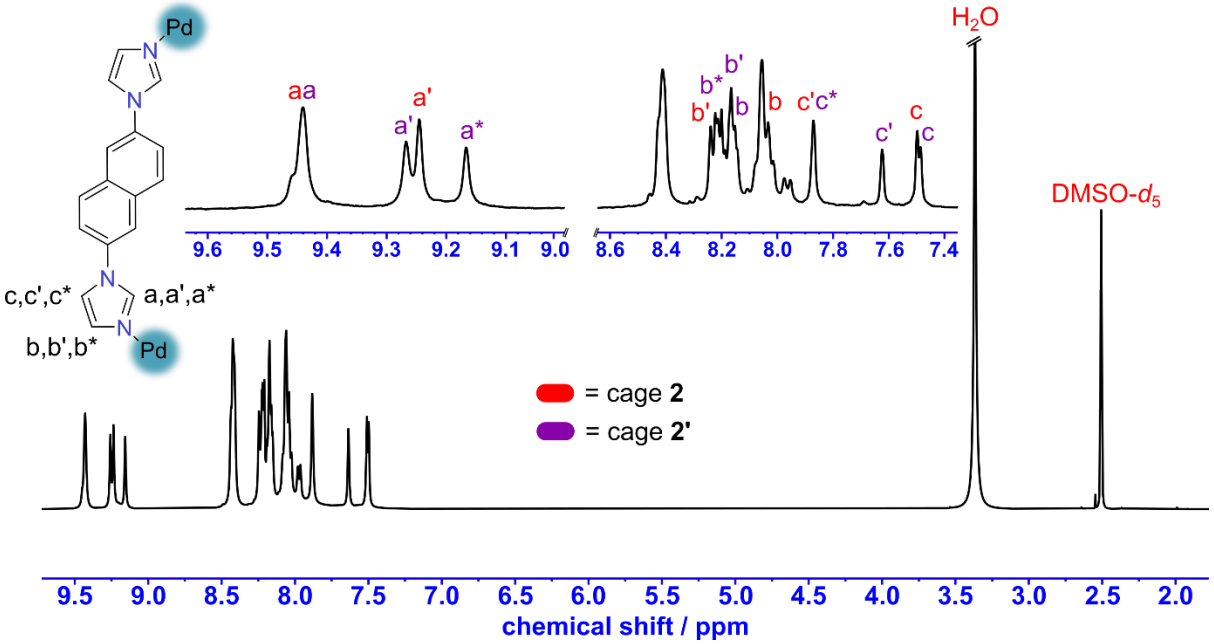

Figure S21: ^{1}H NMR spectrum of cages **2** and **2'**
(500 MHz, 298 K, DMSO-d_6)

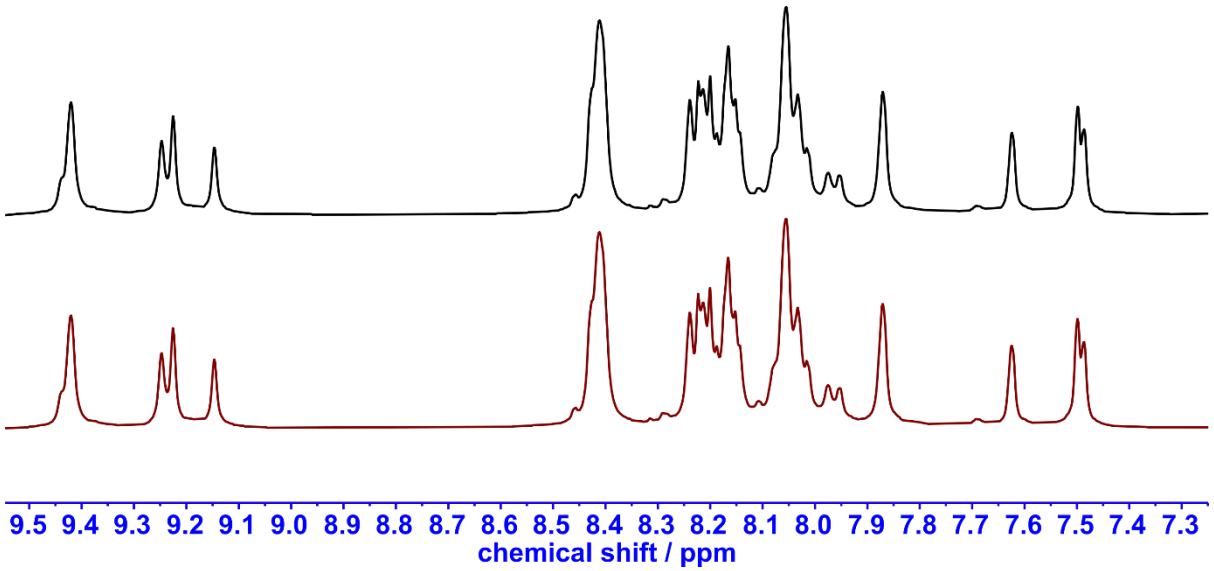

Figure S22: ^{1}H NMR spectra of cages **2** and **2'**: (a) initial (black); (b) after seven days at 22 °C (maroon)
(400 MHz, 298 K, DMSO-d_6)

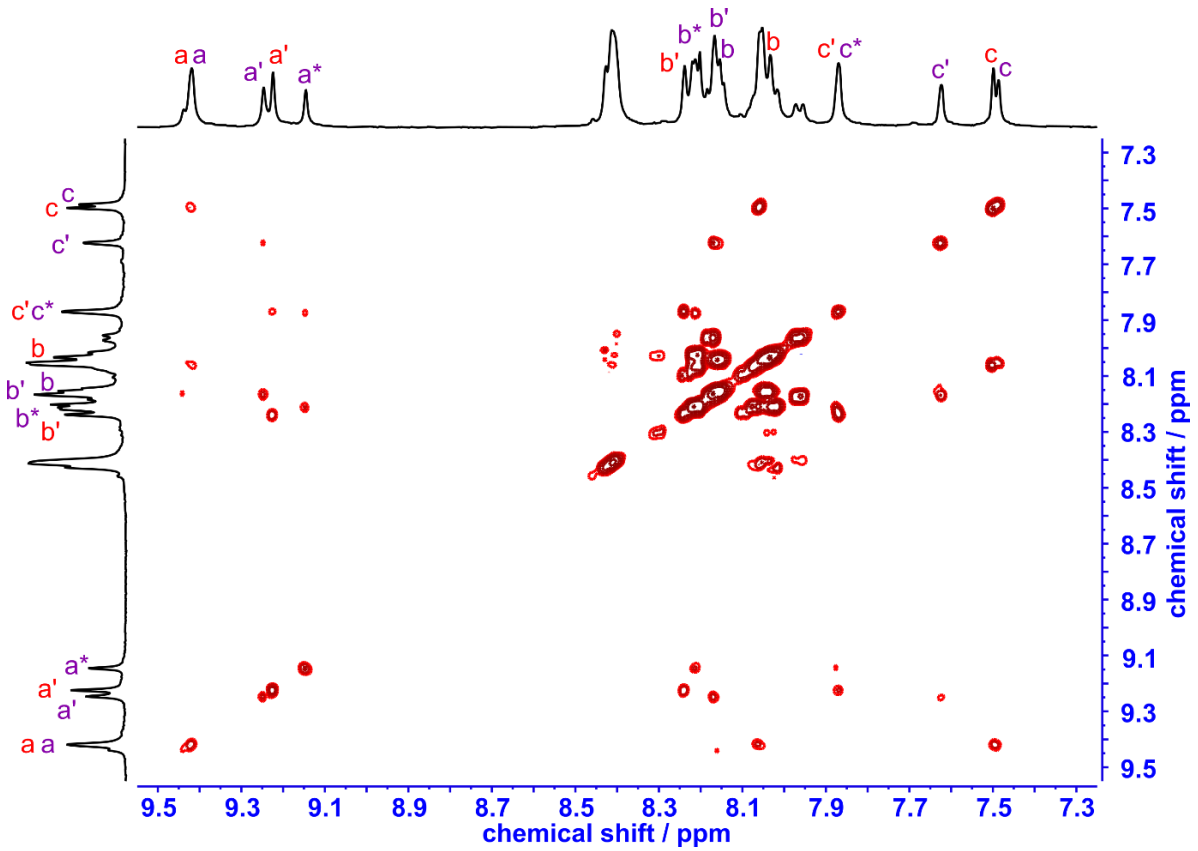

Figure S23: ^{1}H-^{1}H COSY spectrum of cages **2** and **2'**
(500 MHz, 298 K, DMSO-d_6)

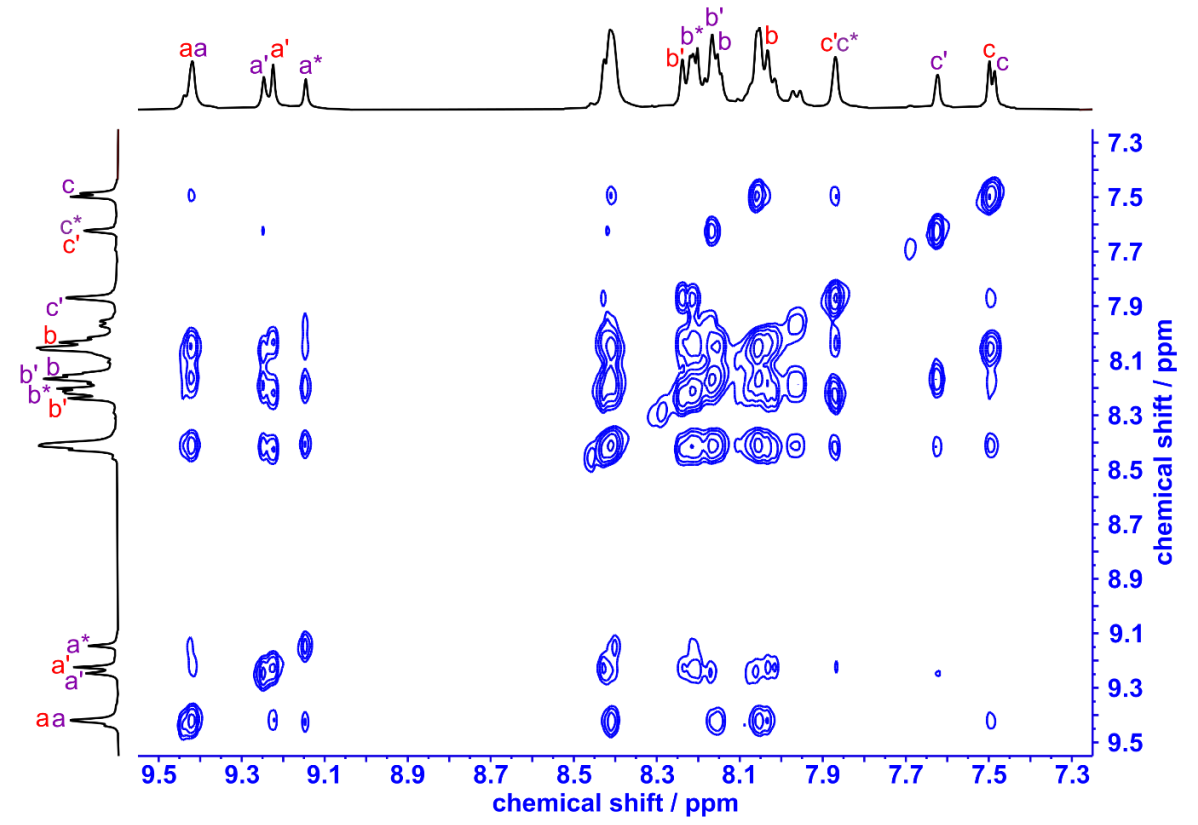

Figure S24: ^{1}H-^{1}H NOESY spectrum of cages **2** and **2'**
(500 MHz, 298 K, DMSO-d_6)

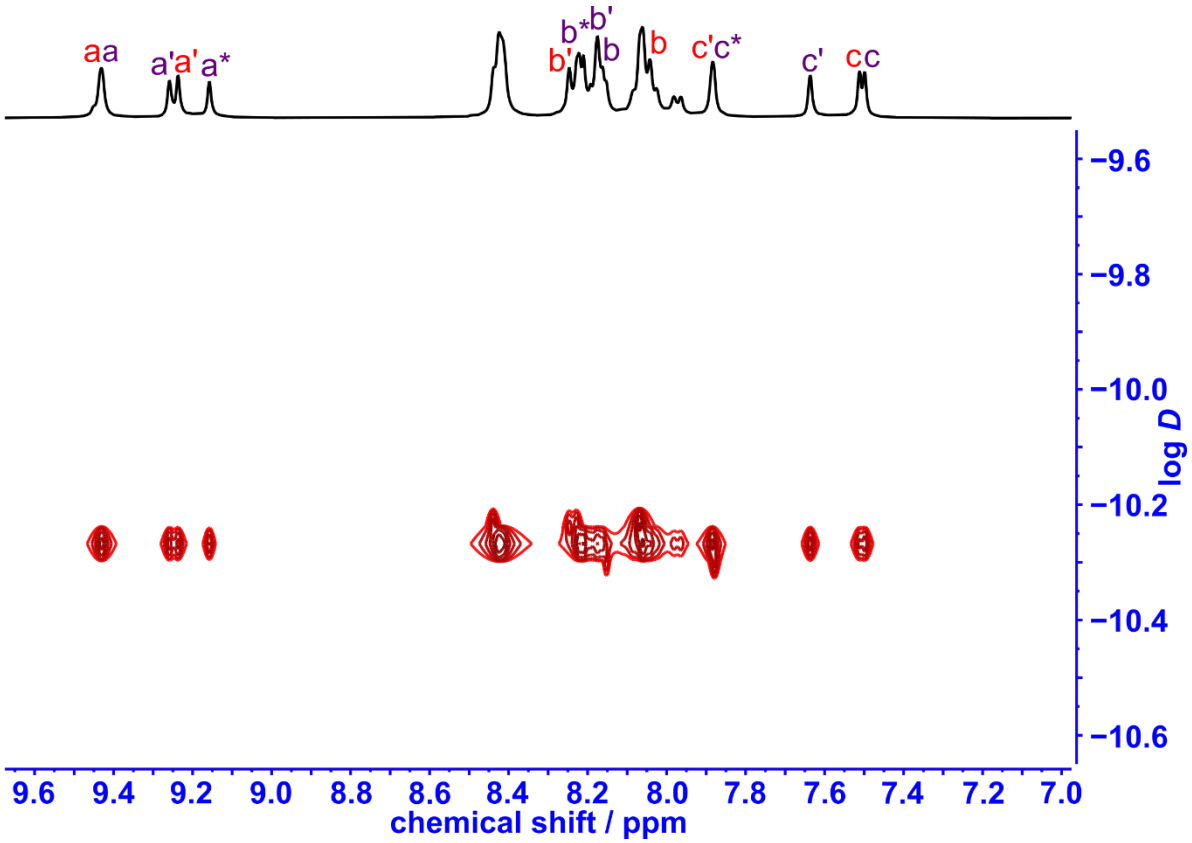

Figure S25: ^{1}H DOSY spectrum of cages **2** and **2'**
(500 MHz, 298 K, DMSO-d_6)

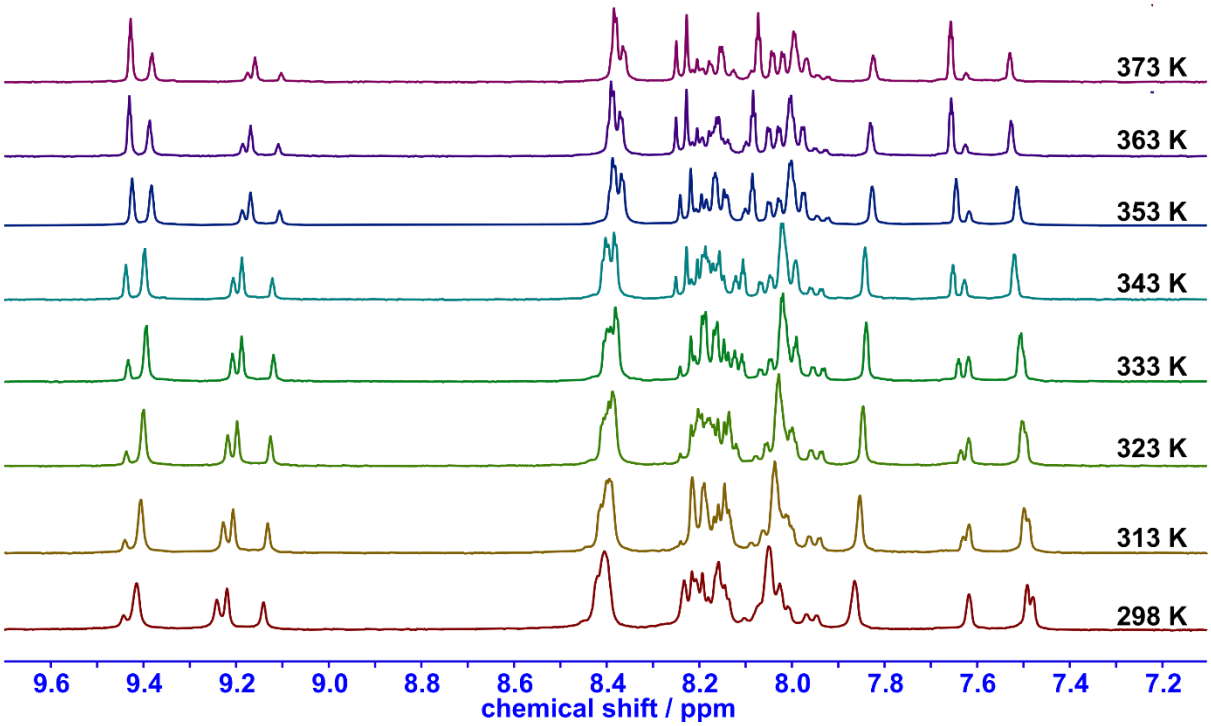

Figure S26: Variable temperature ^{1}H NMR spectra of a sample of cages **2** and **2'**, which had settled to an equilibrium composition after 1 week.
(400 MHz, 298 K, DMSO-d_6)

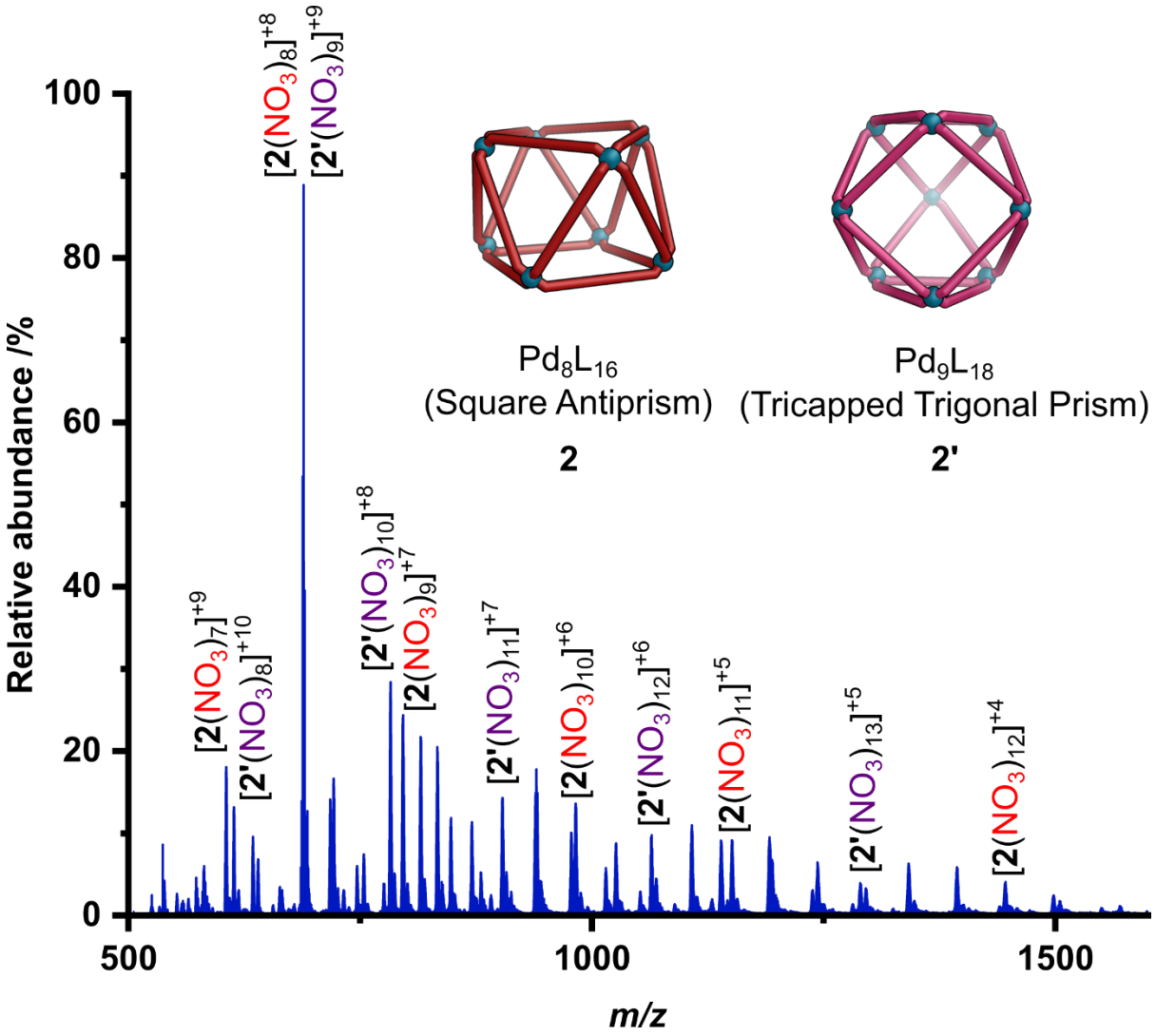

Figure S27: ESI-MS of cages **2** and **2'**. The other peaks observed (not labelled for clarity) correspond to cages **2** and **2'** flying with variable amounts of excess ligand.

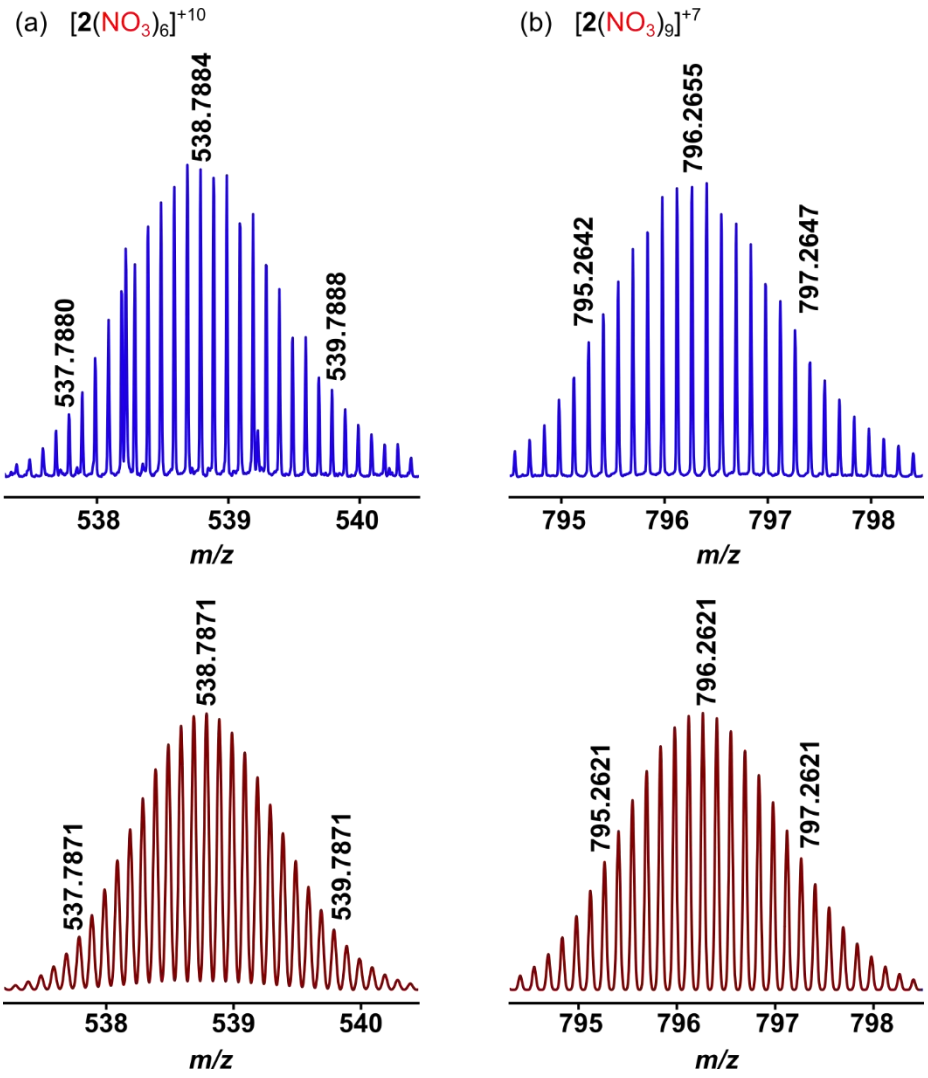

Figure S28: Isotopic distribution of selected peaks from cage **2** showing match between experimentally observed (blue) and predicted (red) patterns (a) $[\mathbf{2}(NO_3)_6]^{+10}$, (b) $[\mathbf{2}(NO_3)_9]^{+7}$

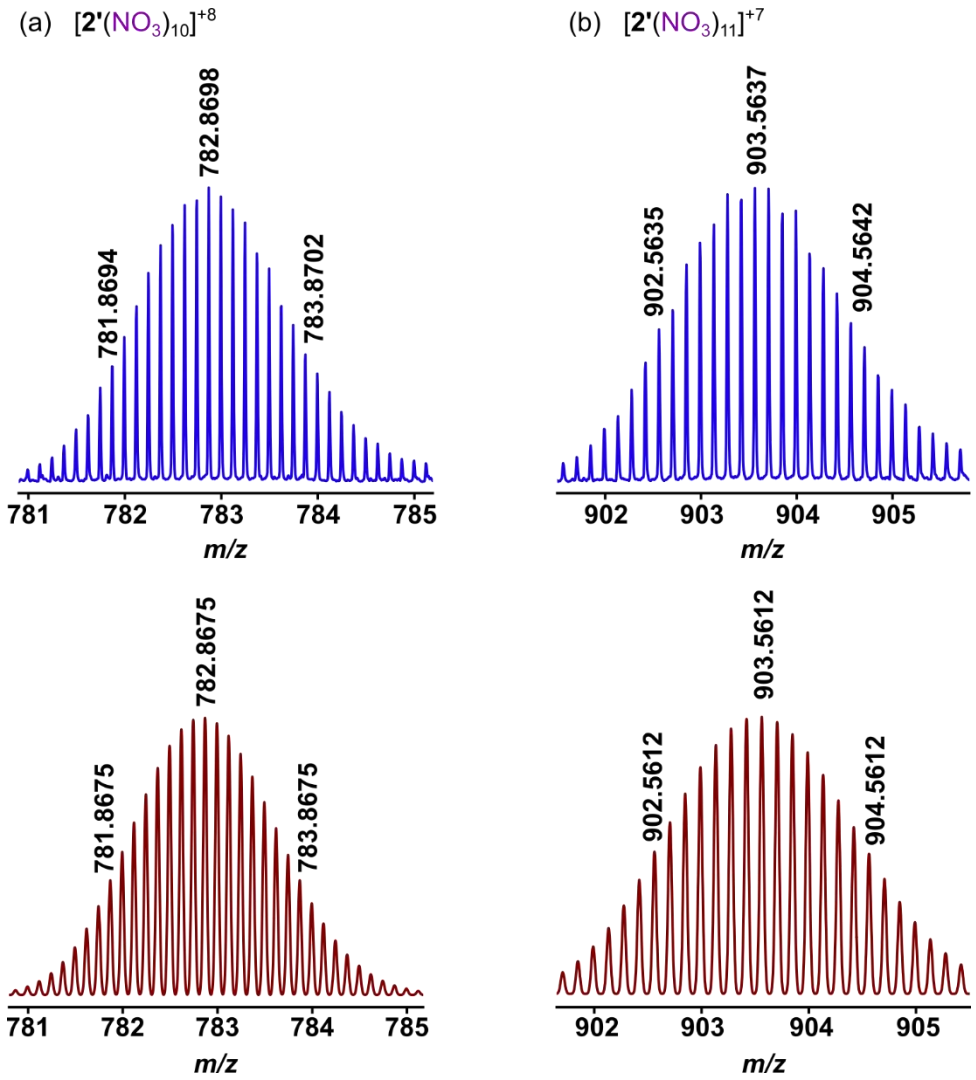

Figure S29: Isotopic distribution of selected peaks from cage **2'** showing match between experimentally observed (blue) and predicted (red) patterns
(a) [**2'**$(NO_3)_{10}]^{+8}$, (b) [**2'**$(NO_3)_{11}]^{+7}$

S5.3 Self-assembly of $Pd_9L^2_{18}$ tricapped trigonal prism 3

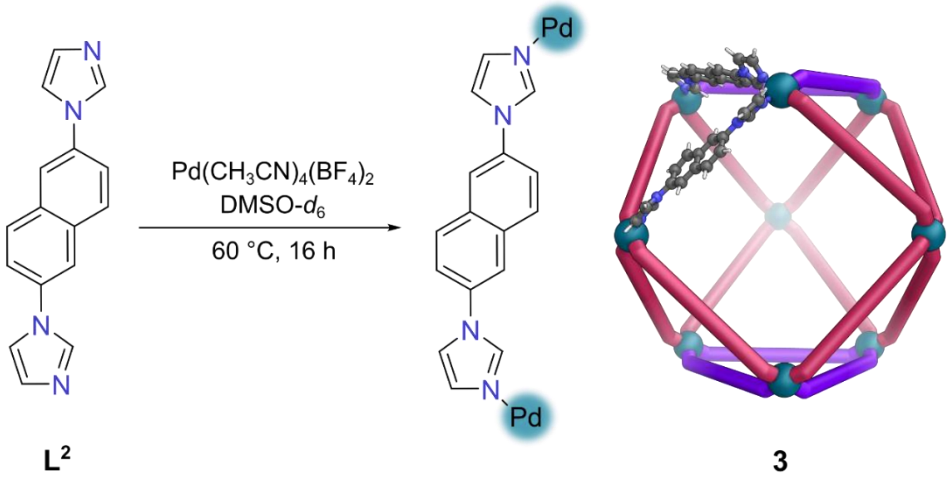

L² **3**

2,6-Di(1H-imidazol-1-yl)naphthalene **L²** (5.00 mg, 0.0192 mmol) and $Pd(CH_3CN)_4(BF_4)_2$ (4.26 mg, 0.00960 mmol) were placed in a 1-dram (4.00 mL) vial and 0.60 mL DMSO-d_6 was added. This mixture was then stirred at 60 °C for 16 h. The resulting reaction mixture was centrifuged (3000 rpm, 5 min) and the supernatant decanted to obtain a pale-yellow solution of cage **3**. On a few occasions it was observed that the initial ^{1}H NMR spectrum of this solution contained a moderate amount of the $Pd_8\mathbf{L^2}_{16}$ assembly. Over time this always settled to almost exclusively $Pd_9\mathbf{L^2}_{18}$ cage **3** (**Figure S32**).

^{1}H NMR (500 MHz, DMSO-d_6) δ_H: 9.31 (s, 12H, a), 9.11 (s, 12H, a'), 9.02 (s, 12H, a*), 8.36-7.93 (m, 108H, naphthalene), 8.20 (s, 12H, b*), 8.16 (s, 12H, b'), 8.06 (s, 12H, b), 7.82 (s, 12H, c*), 7.55 (s, 12H, c'), 7.47 (s, 12H, c).

ESI-MS (ESI, DMSO), *m/z*: $[\mathbf{3}(BF_4)_{13}]^{5+}$ calculated 1354.2294, found 1354.2266; $[\mathbf{3}(BF_4)_{12}]^{6+}$ calculated 1114.0234, found 1114.0201; $[\mathbf{3}(BF_4)_{11}]^{7+}$ calculated 942.4477, found 942.4440; $[\mathbf{3}(BF_4)_{10}]^{8+}$ calculated 813.8909, found 813.8894.

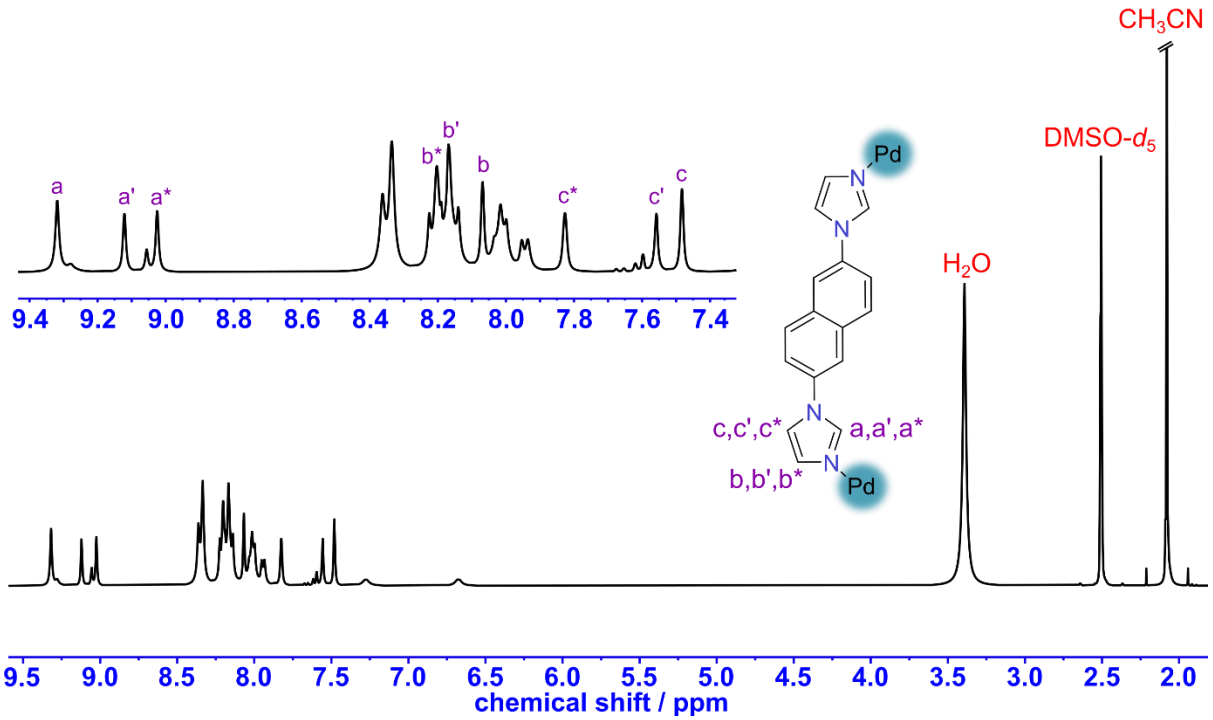

Figure S30: Equilibrated ^{1}H NMR spectrum of cage **3**
(500 MHz, 298 K, DMSO-d_6)

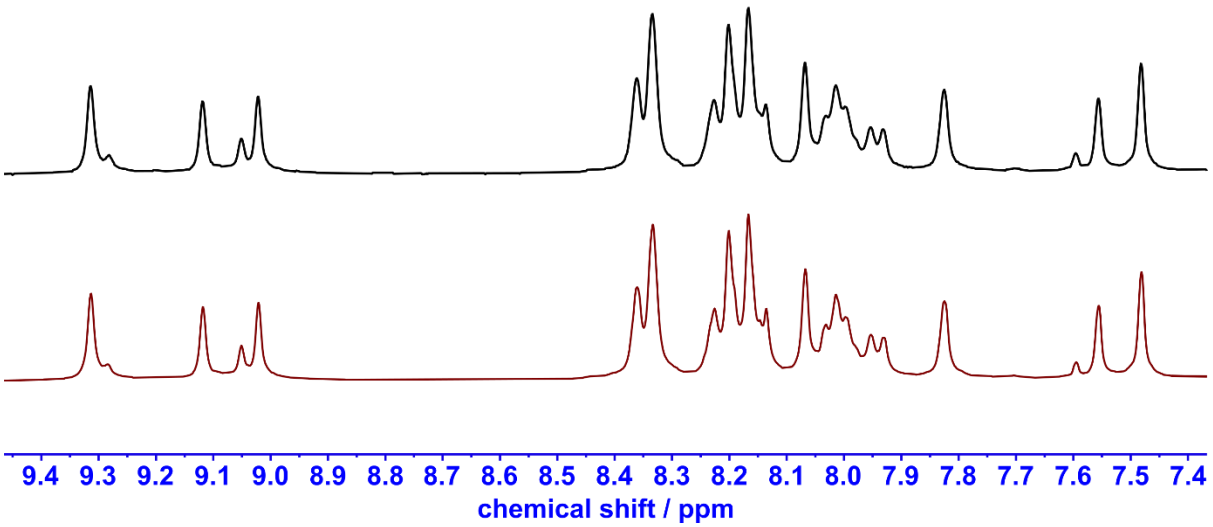

Figure S31: ^{1}H NMR spectra of cage **3**: (a) initial (black); (b) settled after seven days at 22 °C (maroon)
(400 MHz, 298 K, DMSO-d_6)

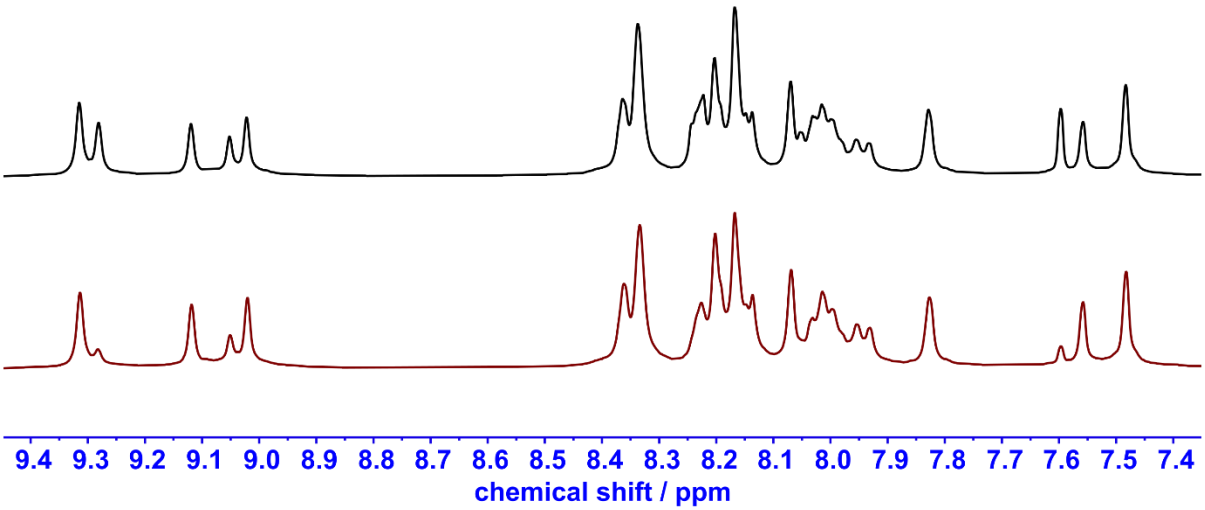

Figure S32: ^{1}H NMR spectra of cage **3** occasionally observed with a moderate amount of a $Pd_8\mathbf{L}^{\mathbf{2}}_{16}$ assembly which then settles back to almost exclusively $Pd_9\mathbf{L}^{\mathbf{2}}_{18}$ cage **3**: (a) initial (black); (b) settled after 14 days (maroon)
(400 MHz, 298 K, DMSO-d_6)

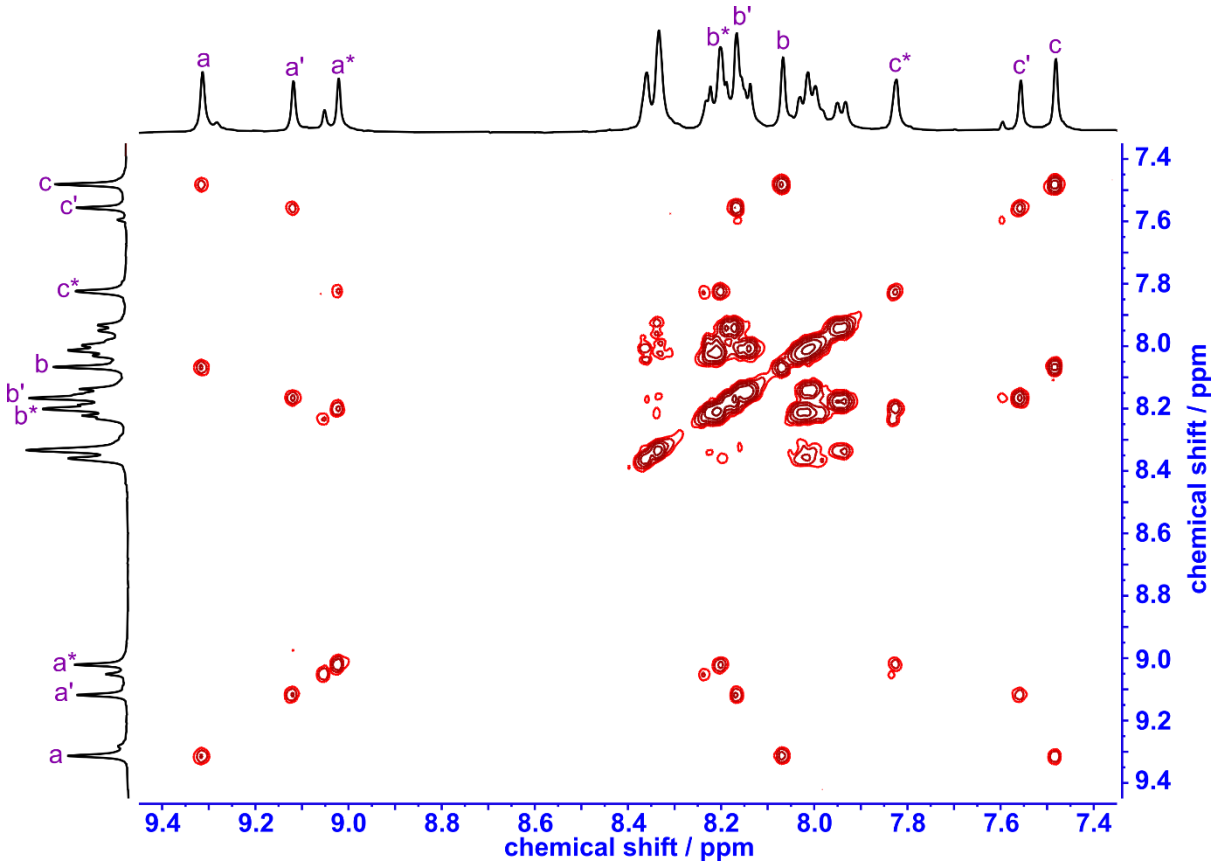

Figure S33: ^{1}H-^{1}H COSY spectrum of cage **3**
(500 MHz, 298 K, DMSO-d_6)

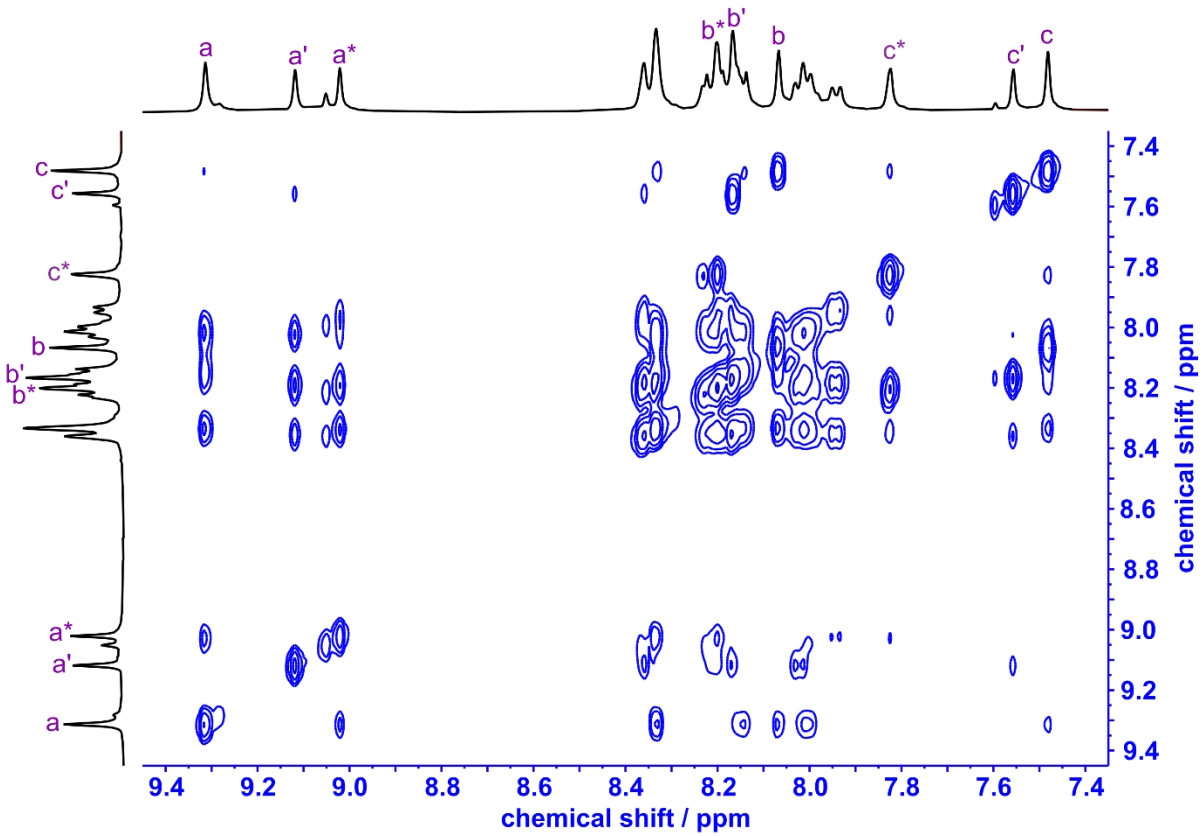

Figure S34: ^{1}H-^{1}H NOESY spectrum of cage **3**
(500 MHz, 298 K, DMSO-d_6)

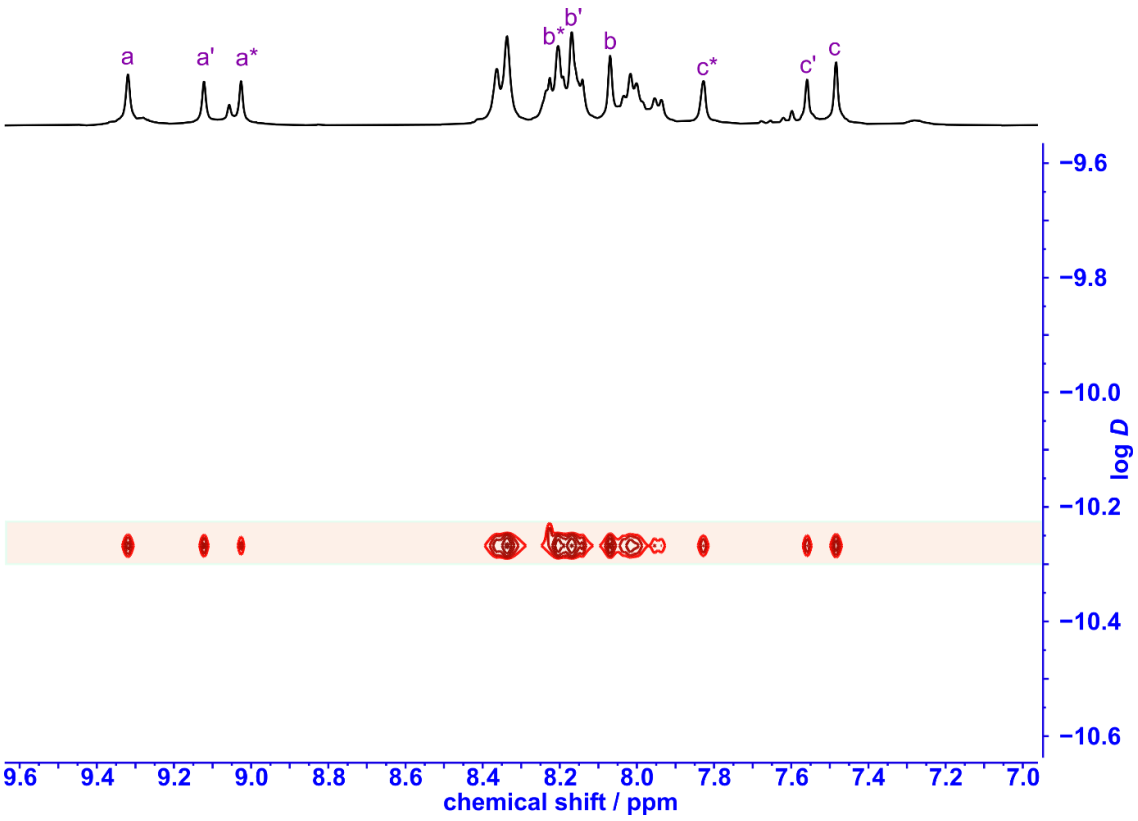

Figure S35: ^{1}H DOSY spectrum of cage **3**
(500 MHz, 298 K, DMSO-d_6)

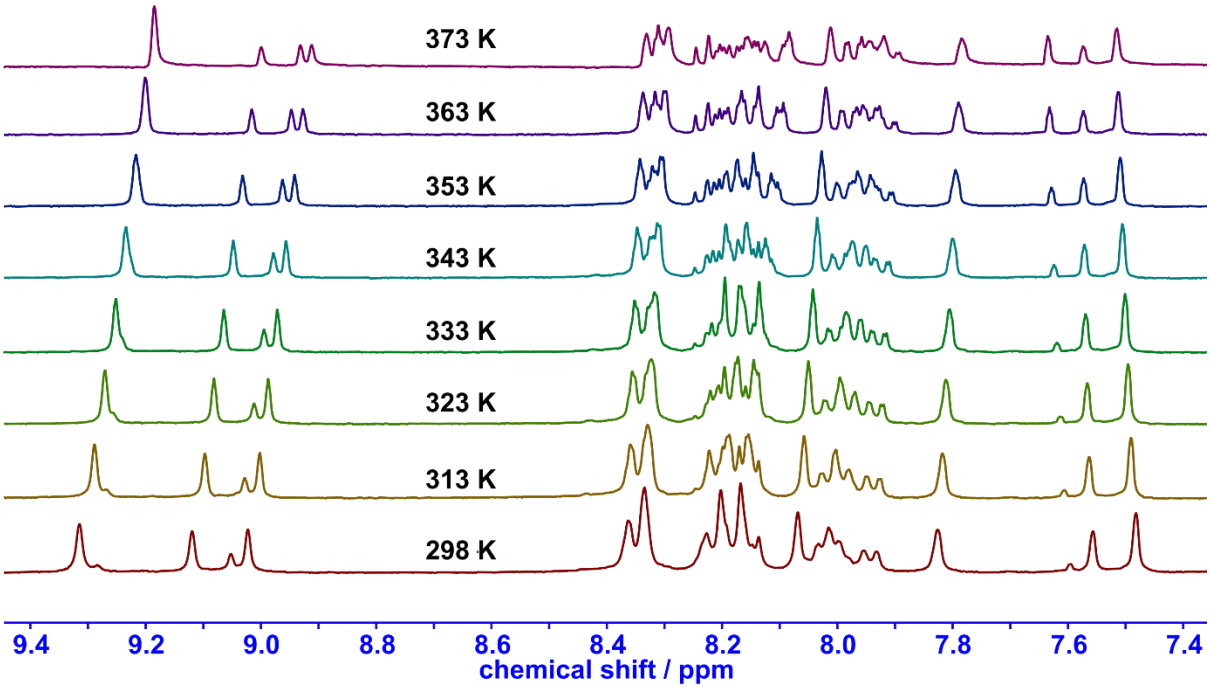

Figure S36: Variable temperature ^{1}H NMR spectra of a sample of cage **3**, which had settled to an equilibrium composition after seven days.
(400 MHz, 298 K, DMSO-d_6)

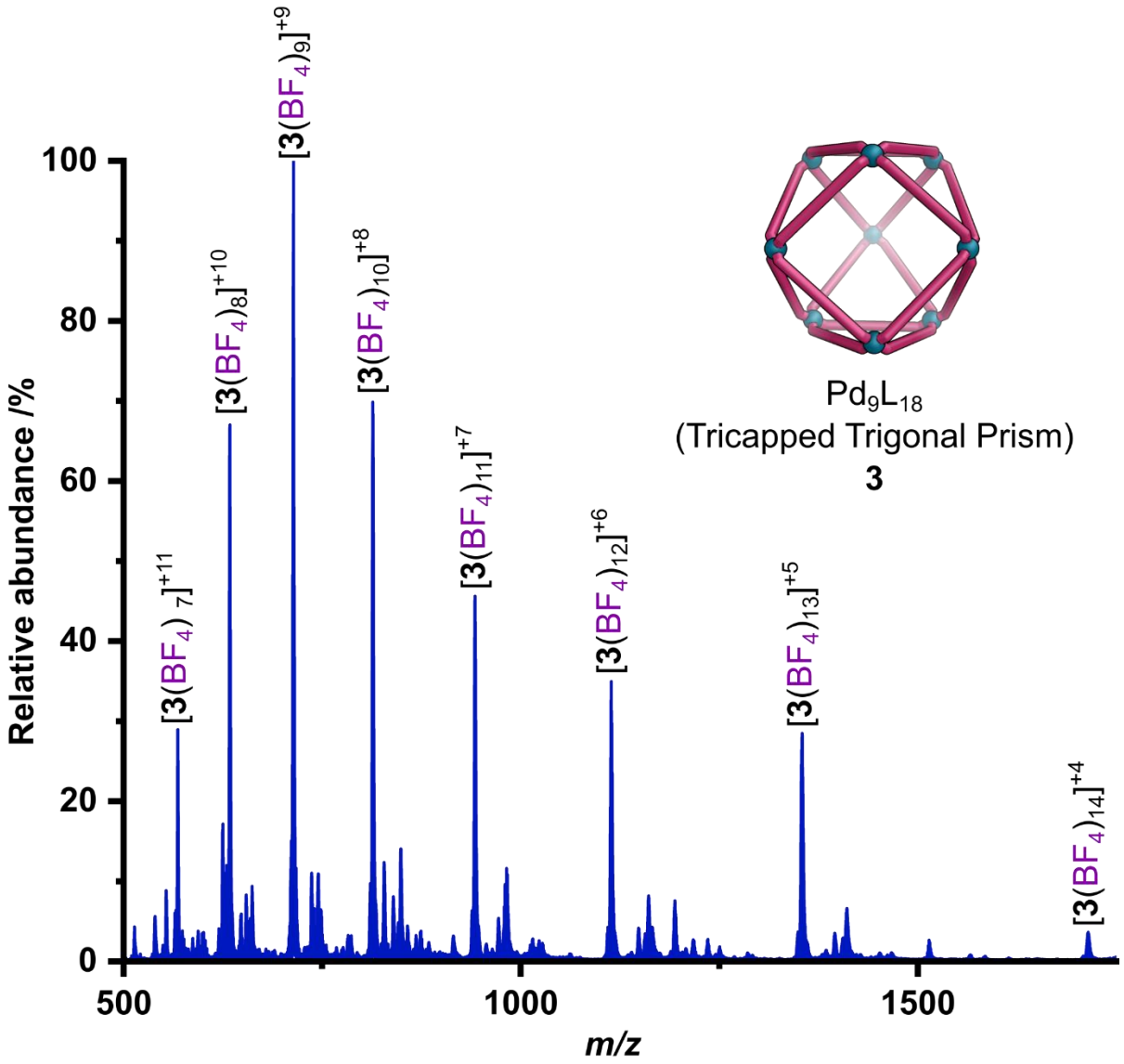

Figure S37: ESI-MS of cage **3**

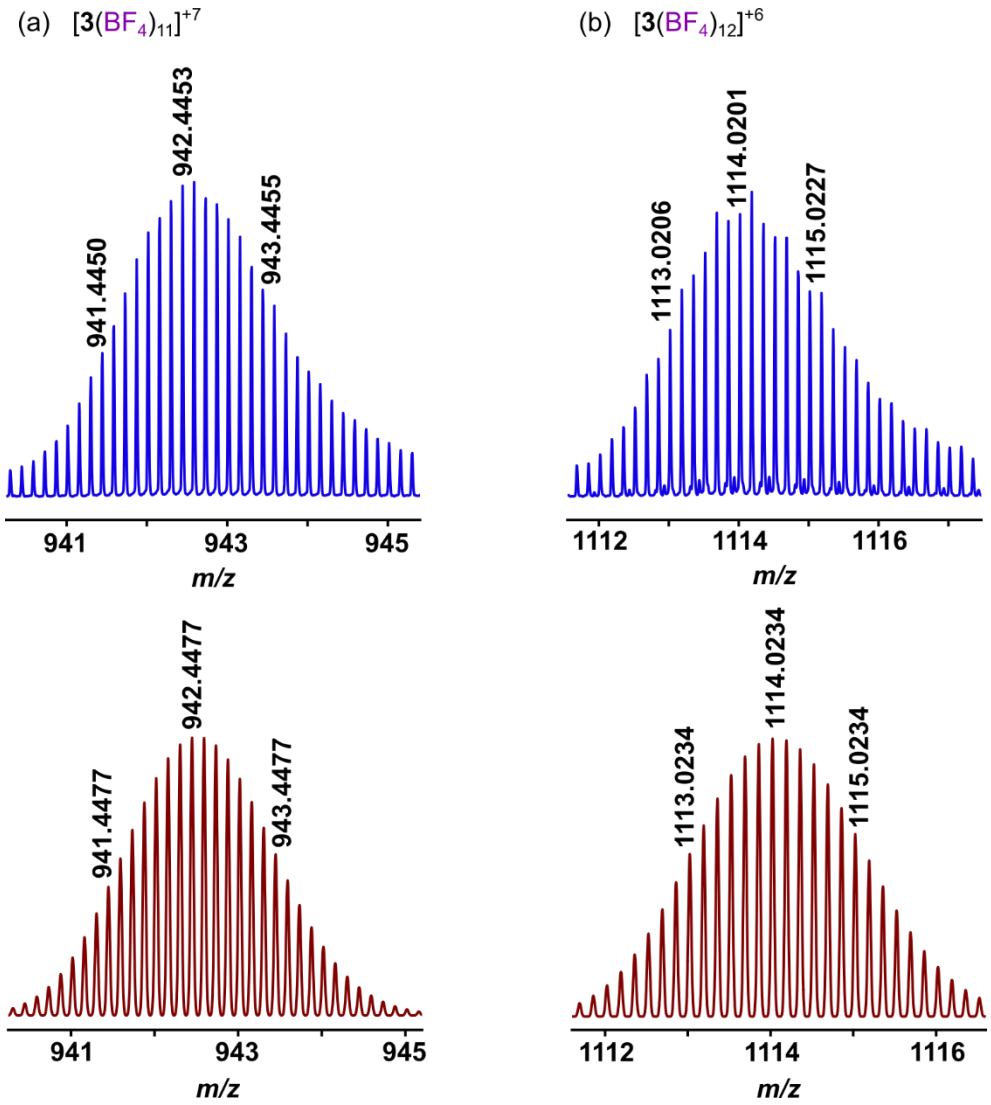

Figure S38: Isotopic distribution of selected peaks from cage **3** showing match between experimentally observed (blue) and predicted (red) patterns
(a) $[\mathbf{3}(BF_4)_{11}]^{+7}$, (b) $[\mathbf{3}(BF_4)_{12}]^{+6}$

S5.4 Self-assembly of $Pd_6L^2_{12}$ octahedron 4 and $Pd_8L^2_{16}$ square antiprism 4'

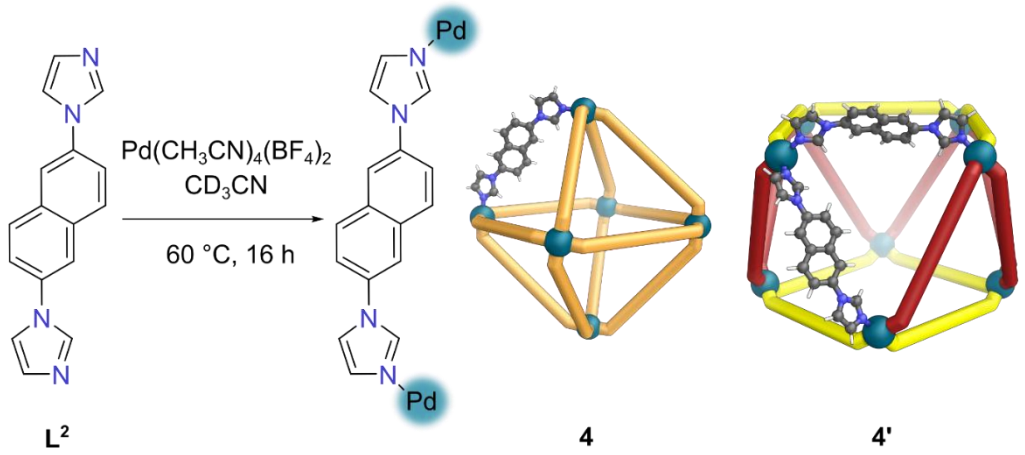

2,6-Di(1H-imidazol-1-yl)naphthalene **L²** (5.00 mg, 0.0192 mmol) and $Pd(CH_3CN)_4(BF_4)_2$ (4.26 mg, 0.00960 mmol) were placed in a 1-dram (4.00 mL) vial and 0.60 mL CD_3CN was added. This mixture was then heated at 60 °C for 16 h. The resulting reaction mixture was centrifuged (3000 rpm, 5 min) and the supernatant decanted to obtain a colourless solution of cages **4** and **4'**.

Cage 4:

^{1}H NMR (500 MHz, CD_3CN) δ_H: 8.99 (s, 24H, a), 8.20-8.11 (m, 48H, naphthalene), 7.83-7.78 (m, 24H, naphthalene), 7.72 (s, 24H, b), 7.57 (s, 24H, c).

ESI-MS (ESI, CH_3CN), *m/z*: [**4**$(BF_4)_7$]$^{5+}$ calculated 873.9507, found 873.9485; [**4**$(BF_4)_6$]$^{6+}$ calculated 713.7912, found 713.7893; [**4**$(BF_4)_5$]$^{7+}$ calculated 599.3915, found 599.3905; [**4**$(BF_4)_4$]$^{8+}$ calculated 513.5918, found 513.5909.

Cage 4':

^{1}H NMR (500 MHz, CD_3CN) δ_H: 8.92 (s, 16H, a), 8.71 (s, 16H, a'), 8.20-8.11 (m, 64H, naphthalene), 7.83-7.78 (m, 32H, naphthalene), 7.79 (s, 16 H, b'), 7.65 (s, 16H, b), 7.64 (s, 16H, c'), 7.41 (s, 16H, c).

ESI-MS (ESI, CH_3CN), *m/z*: [**4'**$(NO_3)_{11}$]$^{5+}$ calculated 1194.2032, found 1194.1953; [**4'**$(NO_3)_{10}$]$^{6+}$ calculated 980.6682, found 980.6631; [**4'**$(NO_3)_9$]$^{7+}$ calculated 828.1433, found 828.1411; [**4'**$(NO_3)_8$]$^{8+}$ calculated 713.7495, found 713.7477.

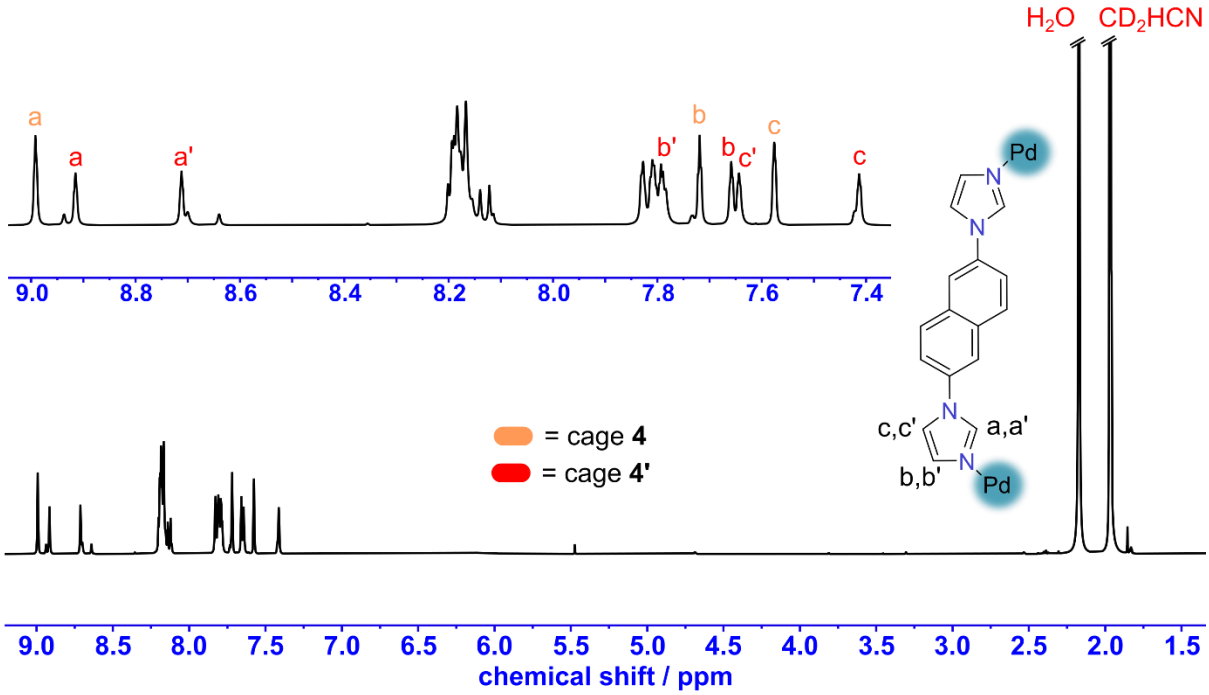

Figure S39: Initial ^{1}H NMR spectrum of cages **4** and **4'**
(500 MHz, 298 K, CD_3CN)

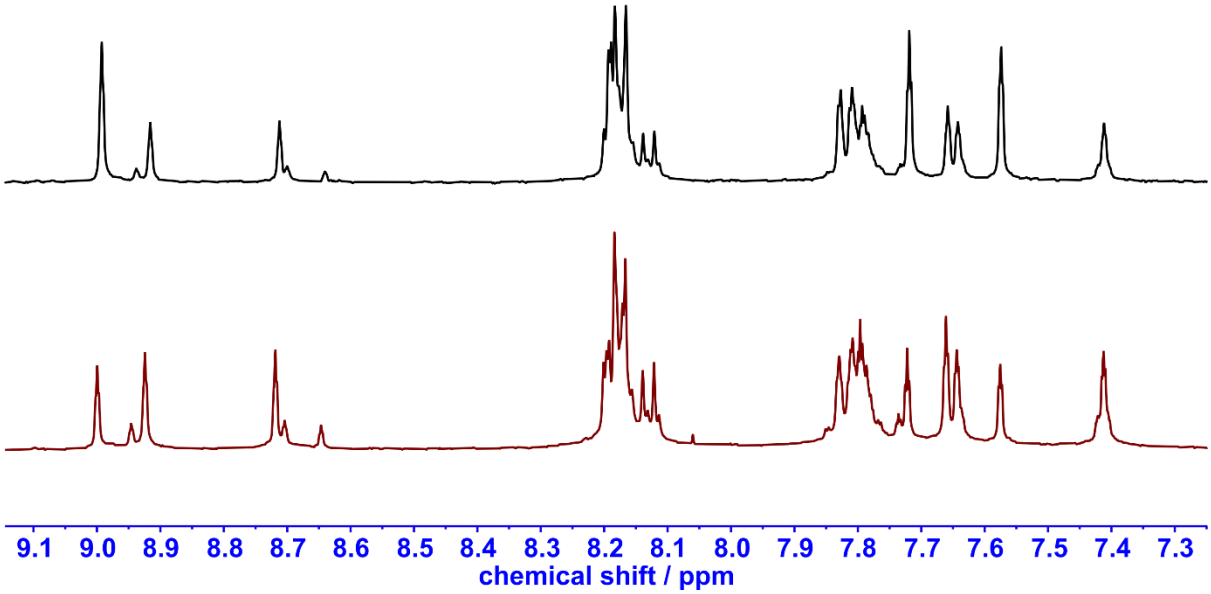

Figure S40: ^{1}H NMR spectra of cages **4** and **4'**: (a) initial (black); (b) settled after 21 days at 22 °C (maroon)
(500 MHz, 298 K, CD_3CN)

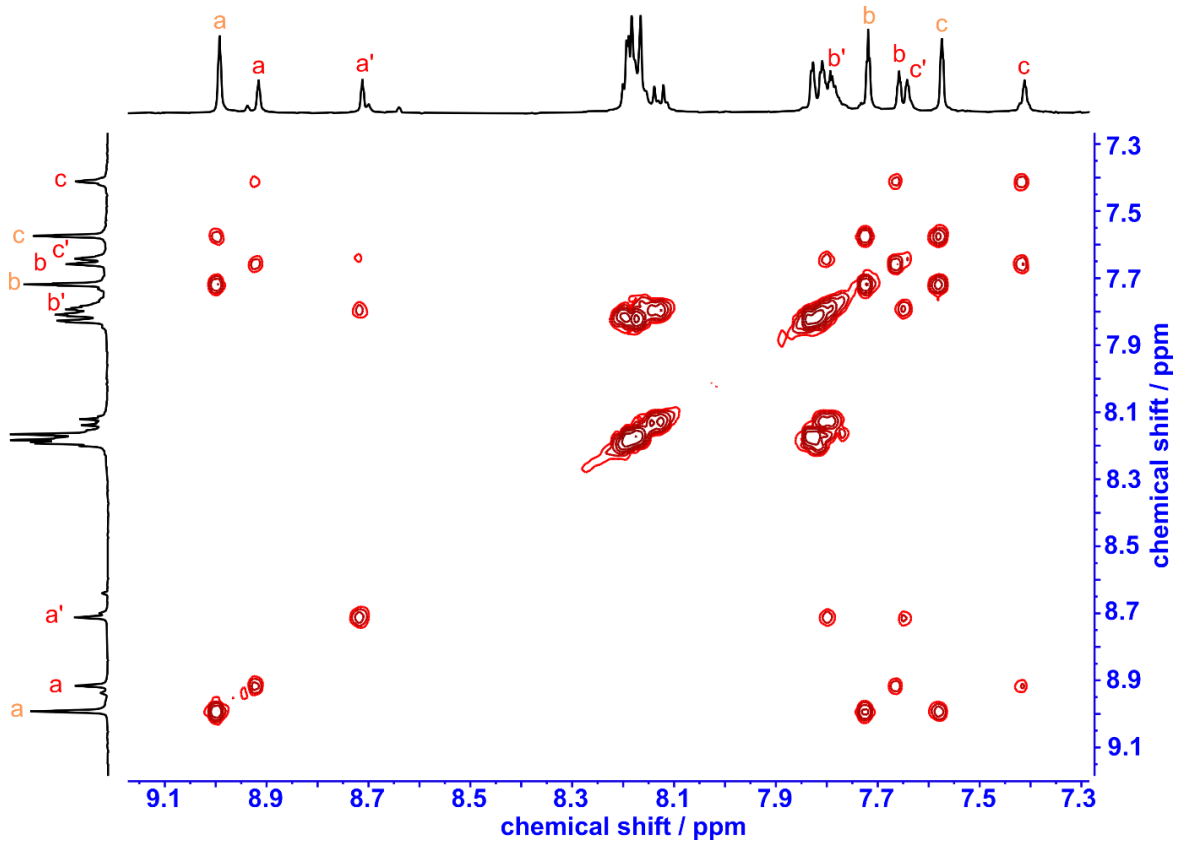

Figure S41: ^{1}H-^{1}H COSY spectrum of cages **4** and **4'**
(500 MHz, 298 K, CD_3CN)

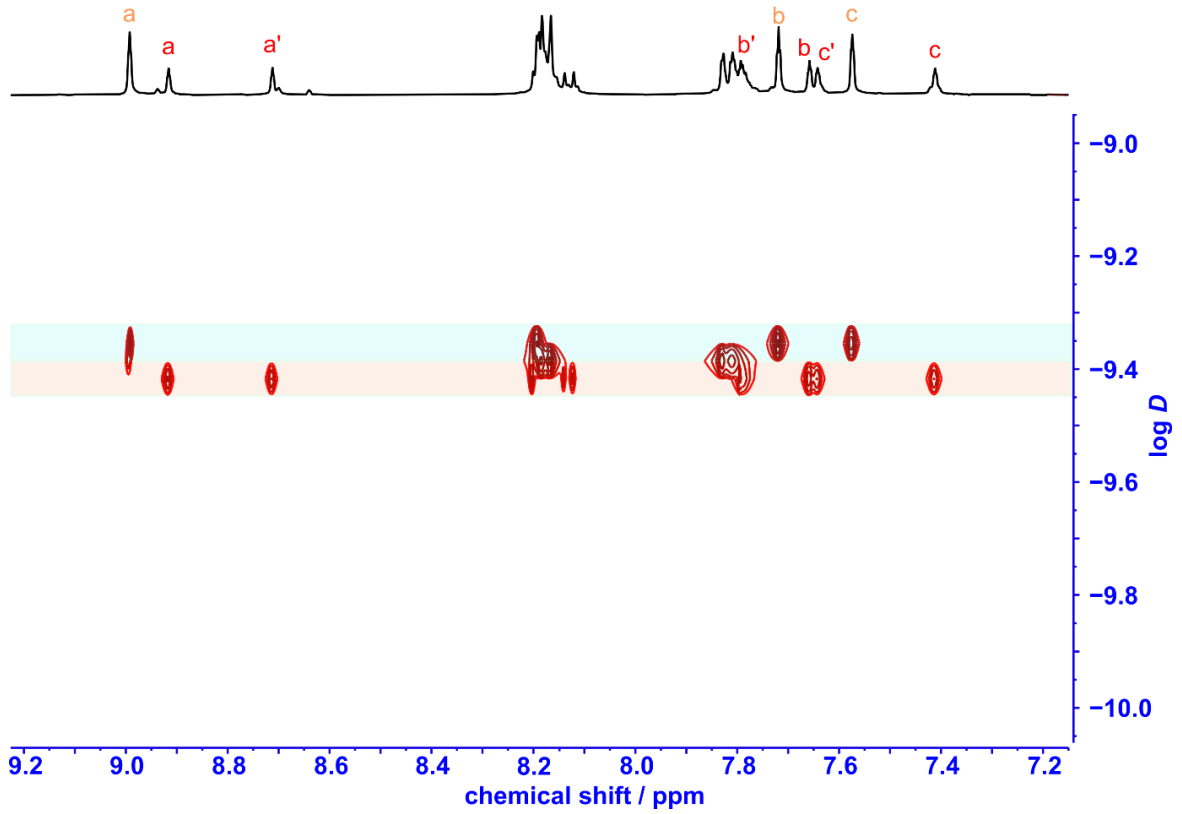

Figure S42: ^{1}H DOSY spectrum of cages **4** and **4'**
(500 MHz, 298 K, CD_3CN)

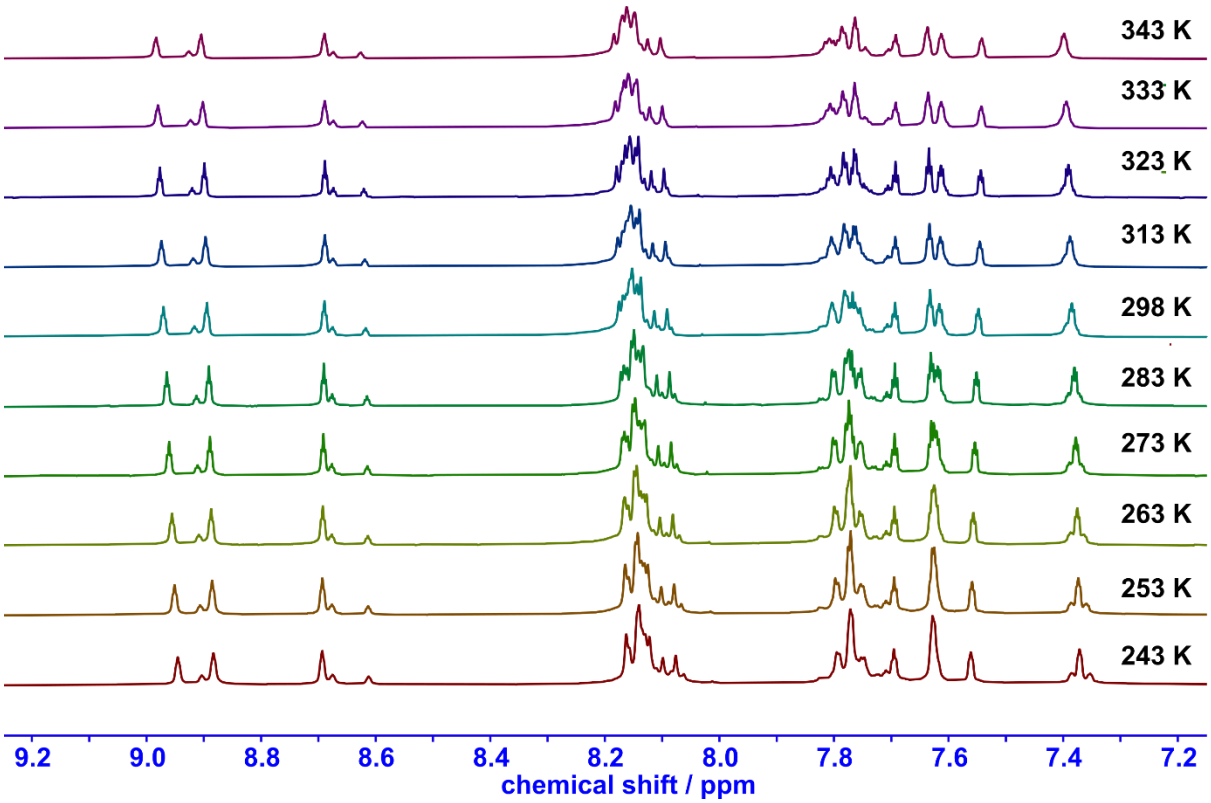

Figure S43: Variable temperature ^{1}H NMR spectra of a sample of cages **4** and **4'**, which had settled to an equilibrium composition after 21 days.
(400 MHz, 298 K, CD_3CN)

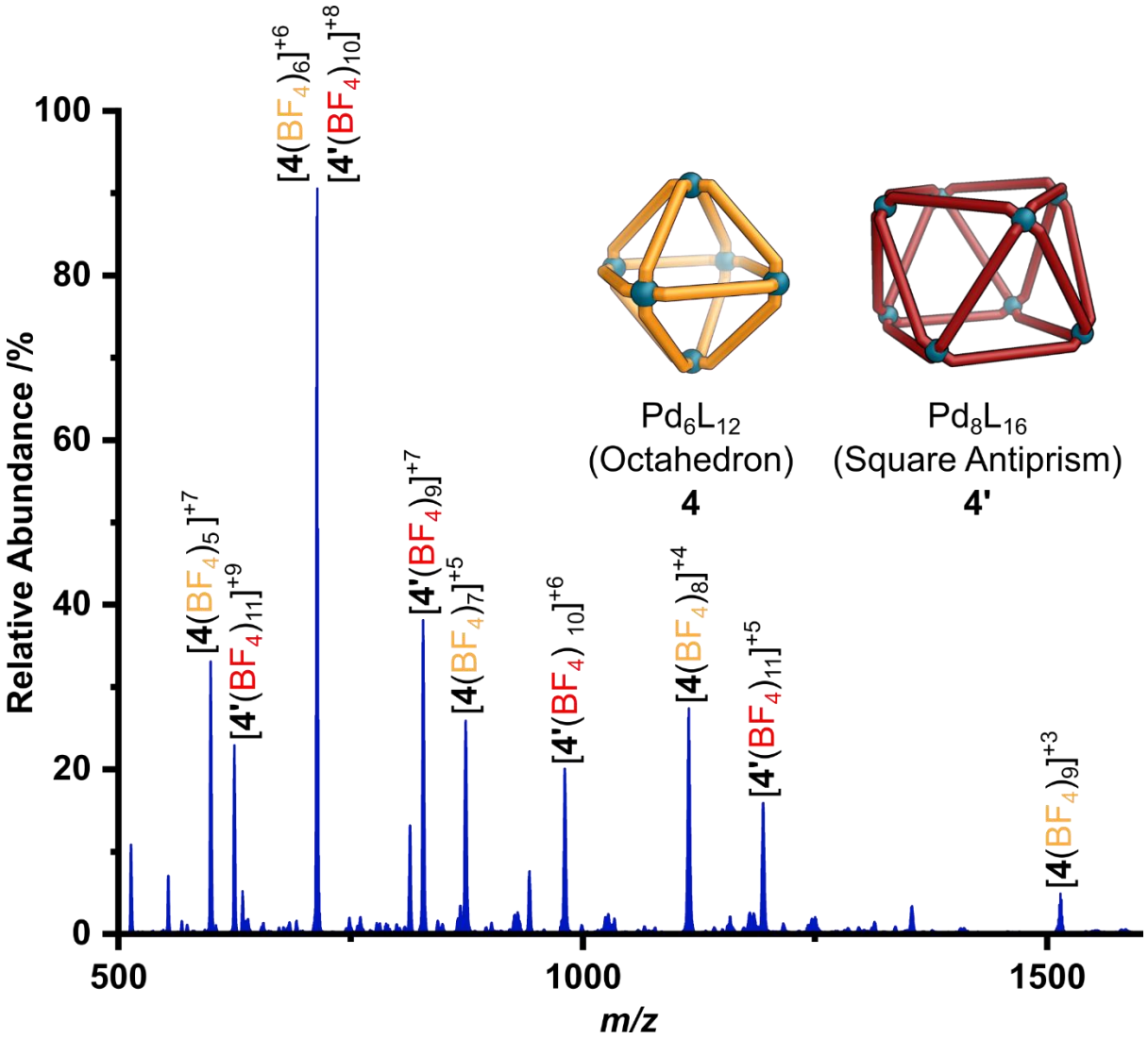

Figure S44: ESI-MS of cages **4** and **4'**

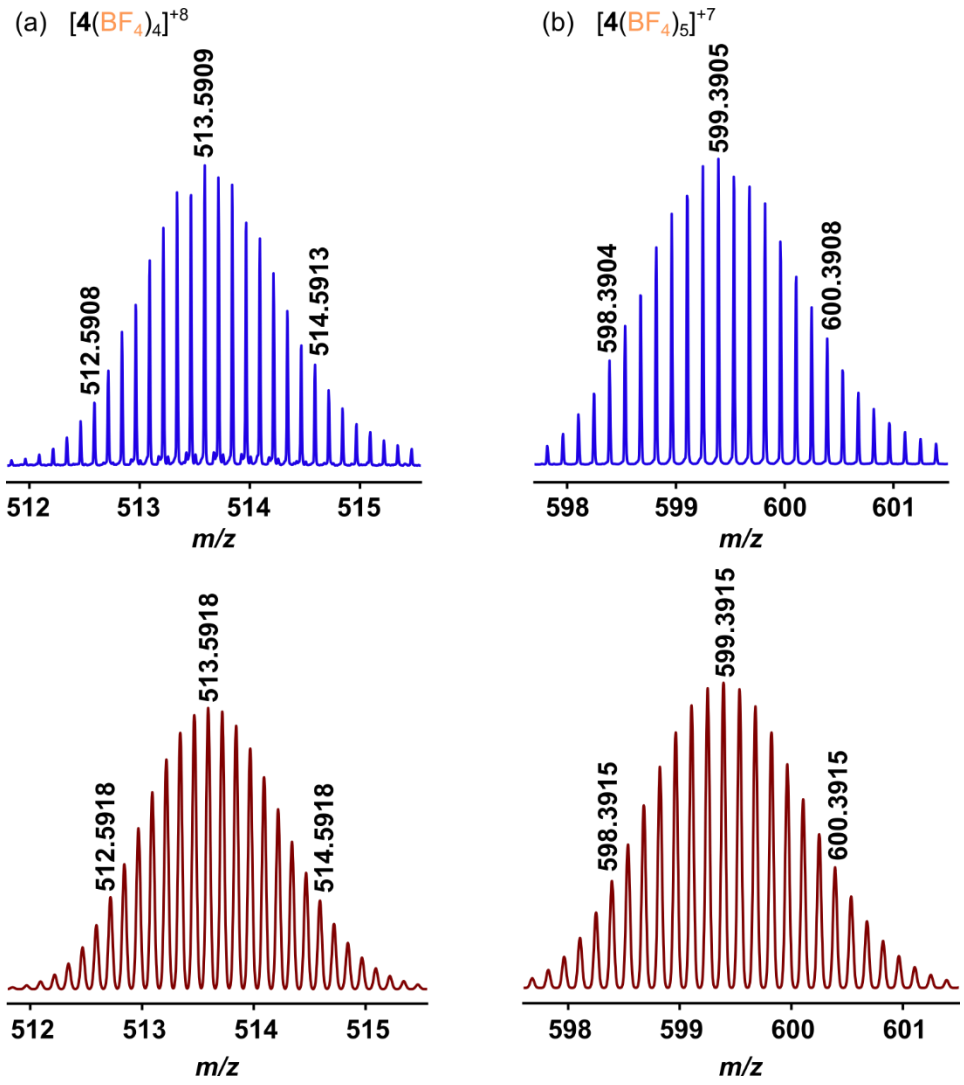

Figure S45: Isotopic distribution of selected peaks from cage **4** showing match between experimentally observed (blue) and predicted (red) patterns
(a) $[\mathbf{4}(BF_4)_4]^{+8}$, (b) $[\mathbf{4}(BF_4)_5]^{+7}$

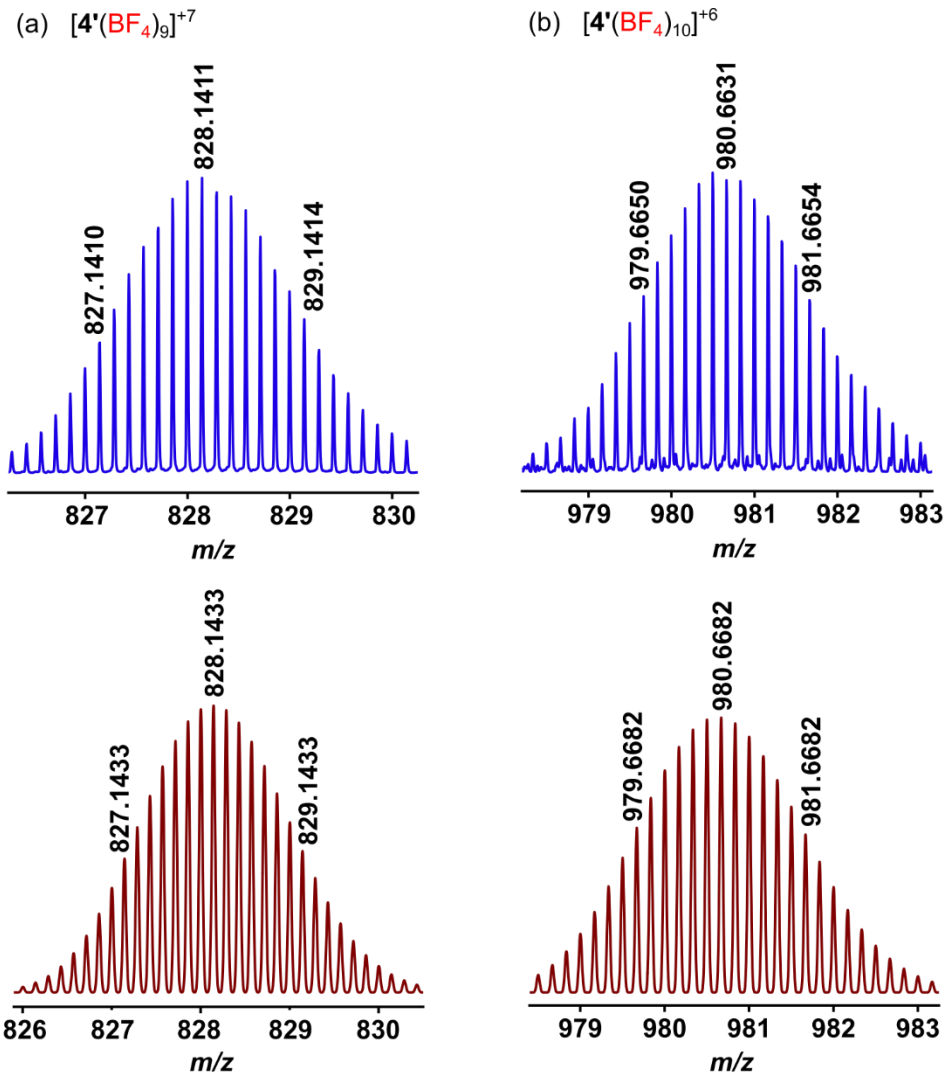

Figure S46: Isotopic distribution of selected peaks from cage **4'** showing match between experimentally observed (blue) and predicted (red) patterns $[\mathbf{4'}(BF_4)_9]^{+7}$, (b) $[\mathbf{4'}(BF_4)_{10}]^{+6}$

S5.5 Self-assembly of $Pd_8L^1_{16}$ square antiprism 5

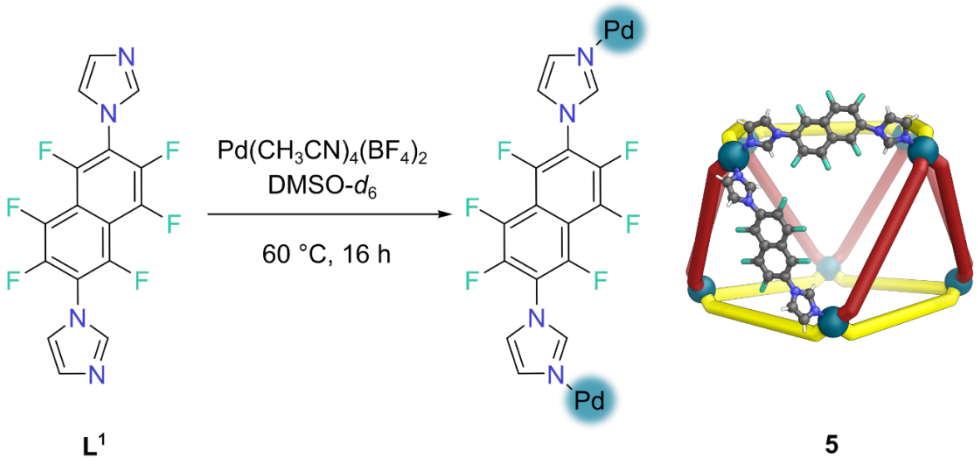

L^1 5

1,1'-(Perfluoronaphthalene-2,6-diyl)bis(1H-imidazole) $\mathbf{L^1}$ (5.00 mg, 0.0136 mmol) and $Pd(CH_3CN)_4(BF_4)_2$ (3.01 mg, 0.00679 mmol) were placed in a 1-dram (4.00 mL) vial and 0.60 mL DMSO-d_6 was added. This mixture was then heated at 60 °C for 16 h. The resulting reaction mixture was centrifuged (3000 rpm, 5 min) and the supernatant decanted to obtain a pale-yellow solution of cage **5**.

^{1}H NMR (500 MHz, DMSO-d_6) δ_H: 8.99 (s, 16H), 8.73 (s, 16H), 8.07 (s, 16H), 7.95 (s, 16H), 7.93 (s, 16H), 7.60 (s, 16H).

^{19}F NMR (376 MHz, DMSO-d_6) δ_F: −127.74 to −132.37 (m, 32F), −142.94 to −145.98 (m, 32F), −147.23 to −150.13 (m, 32F), −151.00 (br, 13F, $^{10}BF_4$), −151.05 (br, 51F, $^{11}BF_4$).

ESI-MS (ESI, DMSO), *m/z*: $[\mathbf{5}(BF_4)_{11}]^{5+}$ calculated 1539.6223, found 1539.6210; $[\mathbf{5}(BF_4)_{10}]^{6+}$ calculated 1268.5175, found 1268.5146; $[\mathbf{5}(BF_4)_9]^{7+}$ calculated 1074.8712, found 1074.8716; $[\mathbf{5}(BF_4)_8]^{8+}$ calculated 929.6365, found 929.6347; $[\mathbf{5}(BF_4)_7]^{9+}$ calculated 816.6761, found 816.6785.

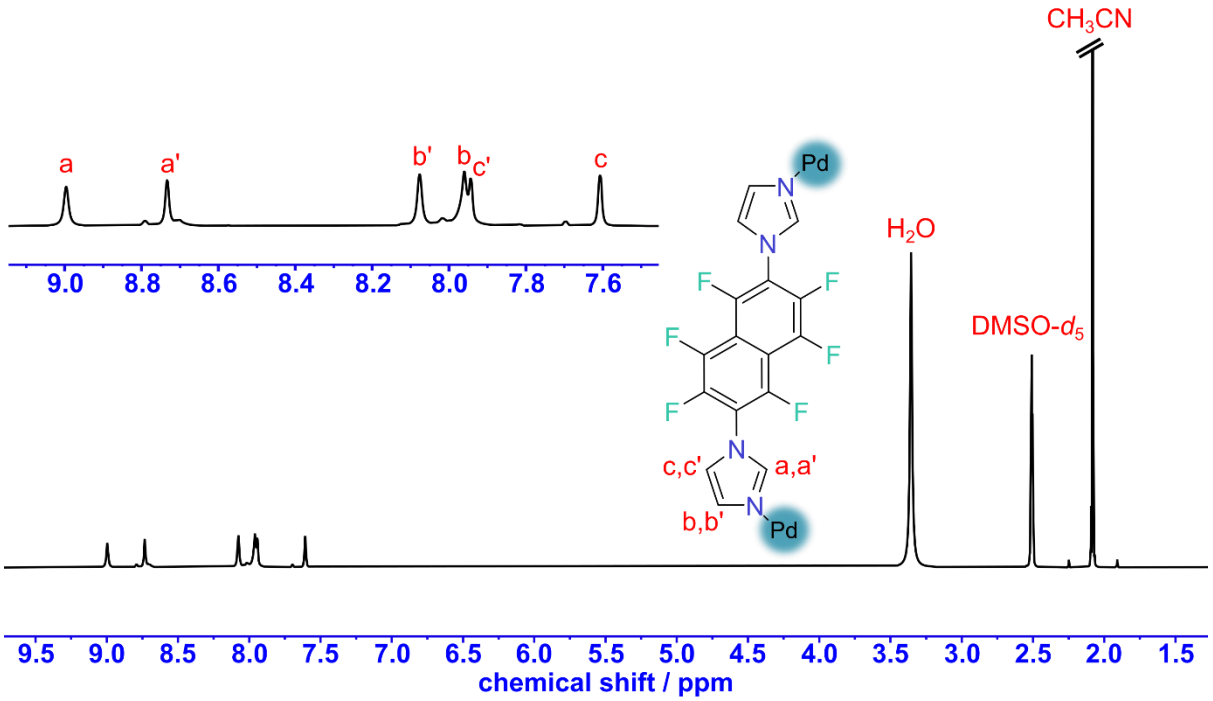

Figure S47: ^{1}H NMR spectrum of cage **5**
(400 MHz, 298 K, DMSO-d_6)

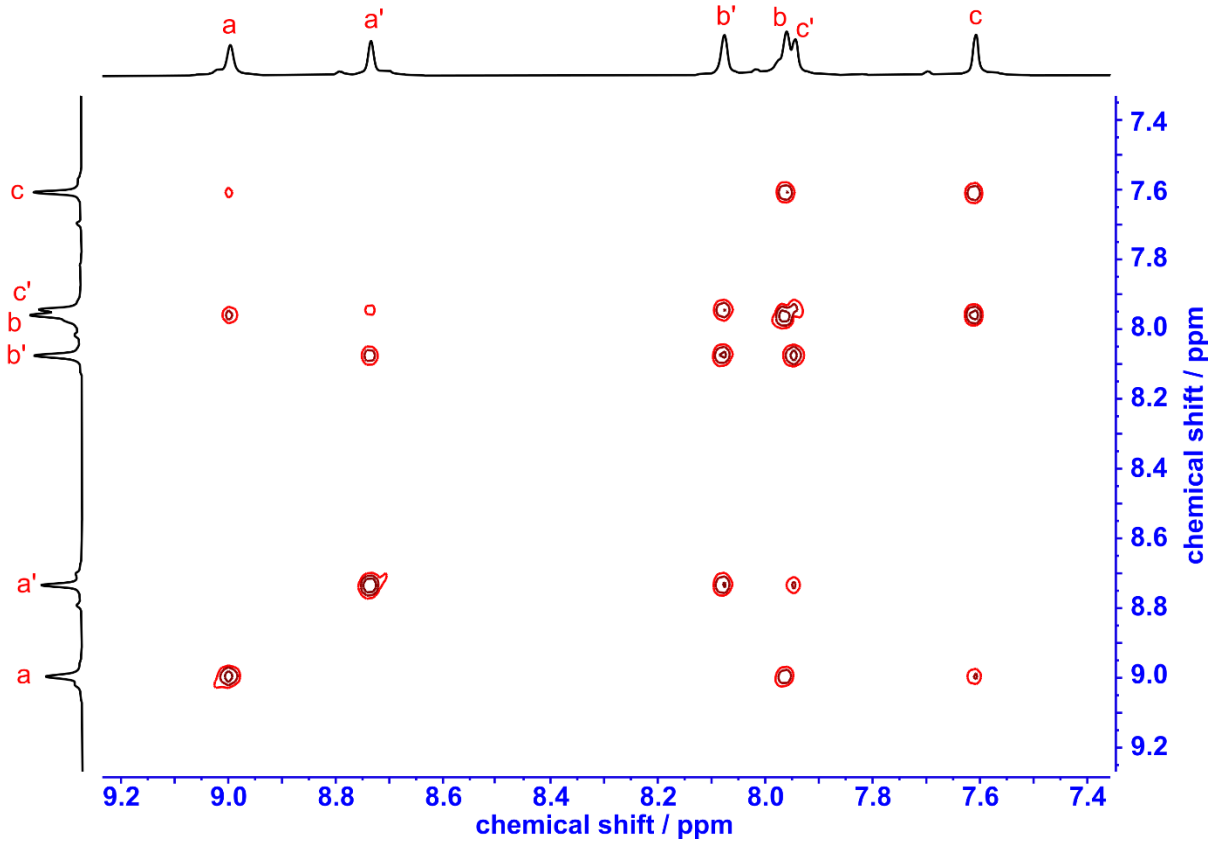

Figure S48: ^{1}H-^{1}H COSY spectrum of cage **5**
(400 MHz, 298 K, DMSO-d_6)

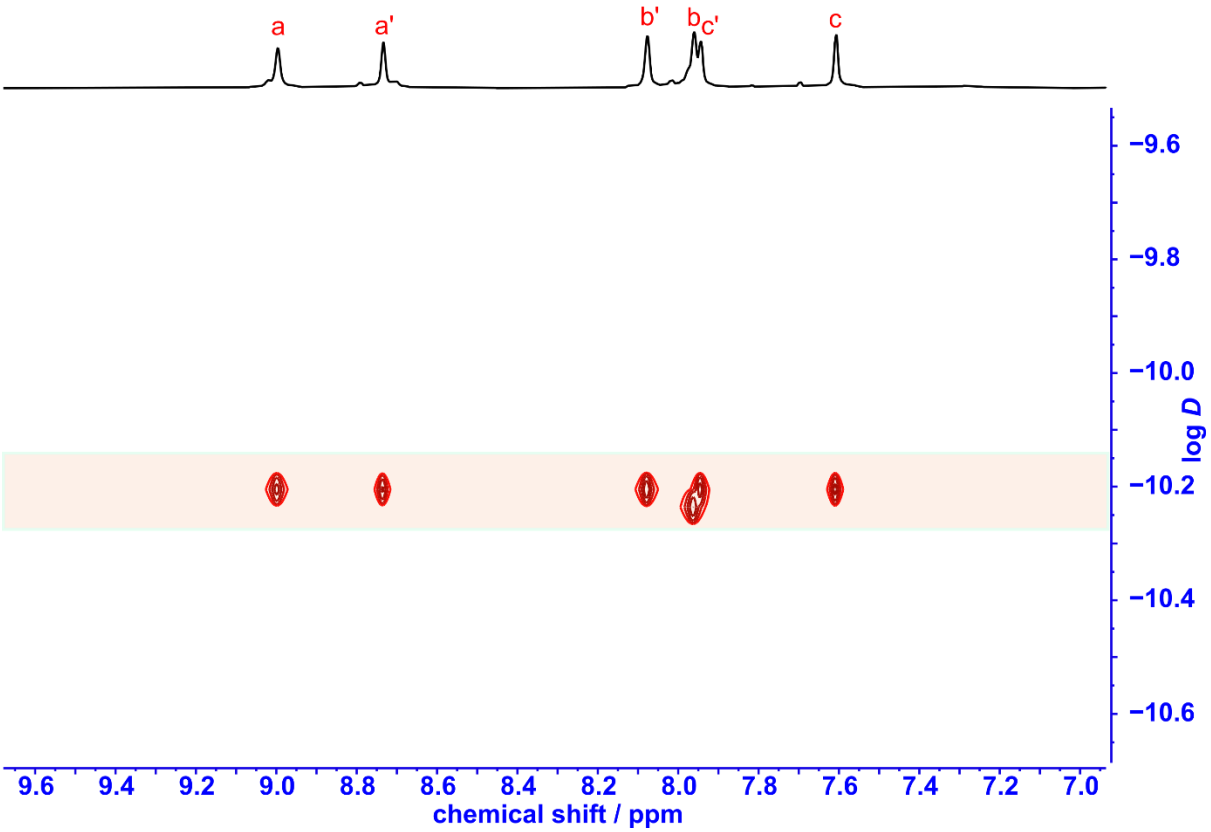

Figure S49: ^{1}H DOSY spectrum of cage **5**
(400 MHz, 298 K, DMSO-d_6)

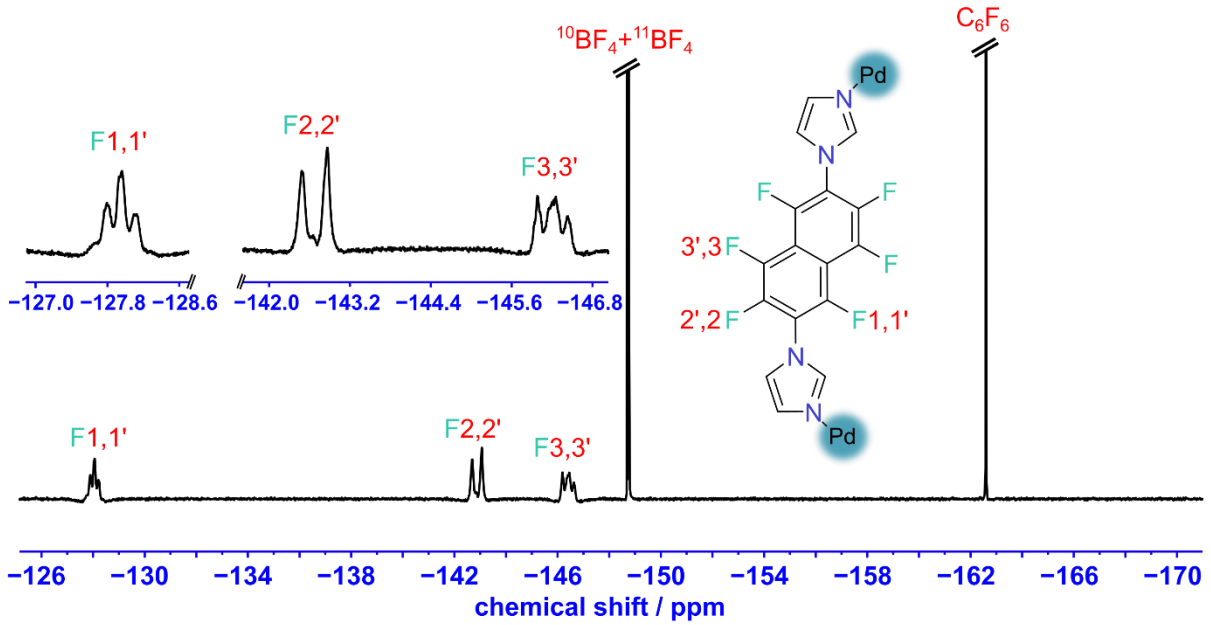

Figure S50: ^{19}F NMR spectrum of cage **5**
(376 MHz, 298 K, DMSO-d_6)

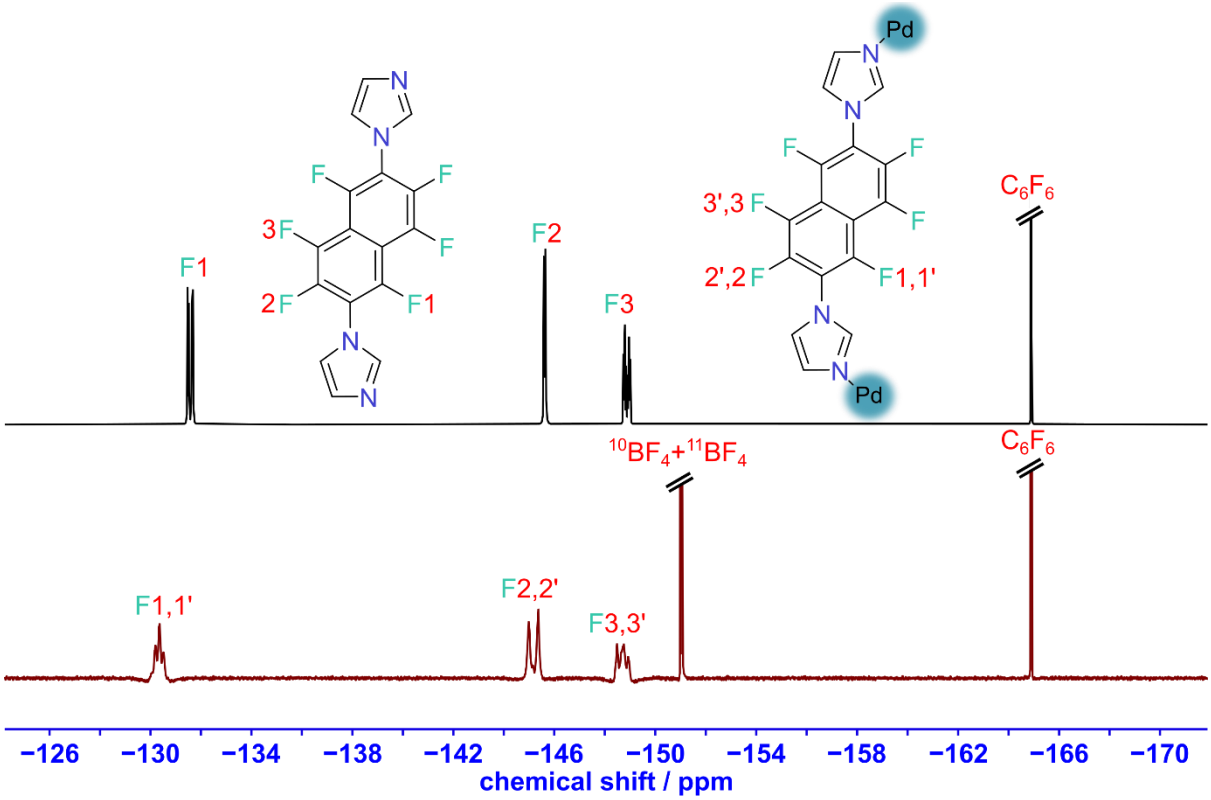

Figure S51: Stack plot of ^{19}F NMR spectra of ligand **L^1** (black) and cage **5** (maroon) (376 MHz, 298 K, DMSO-d_6)

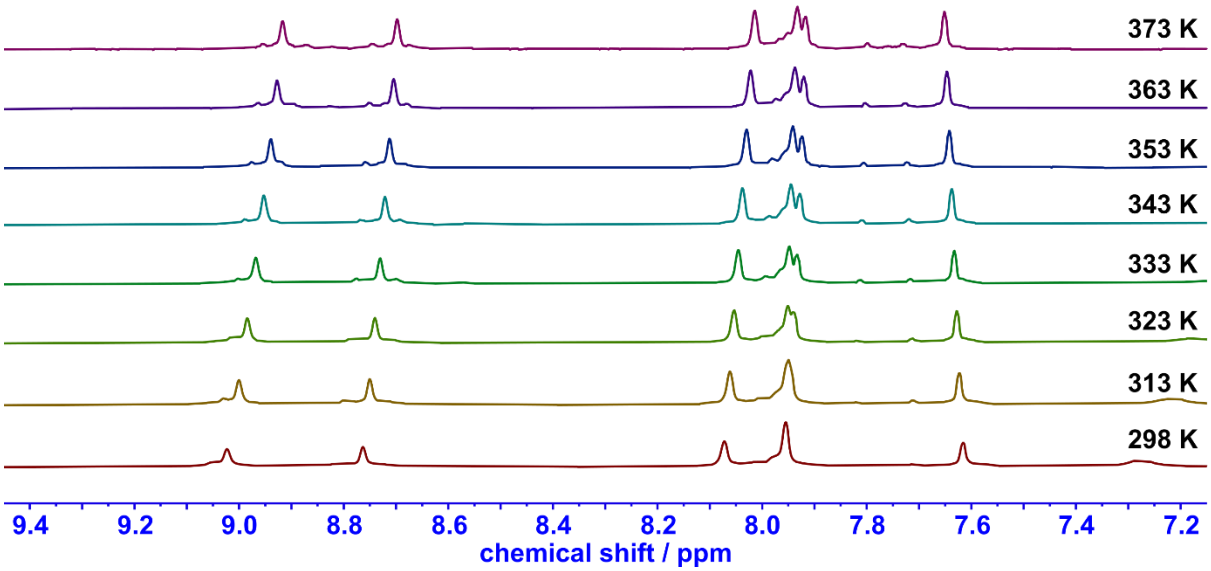

Figure S52: Variable temperature ^{1}H NMR spectra of a sample of cage **5** (400 MHz, 298 K, DMSO-d_6)

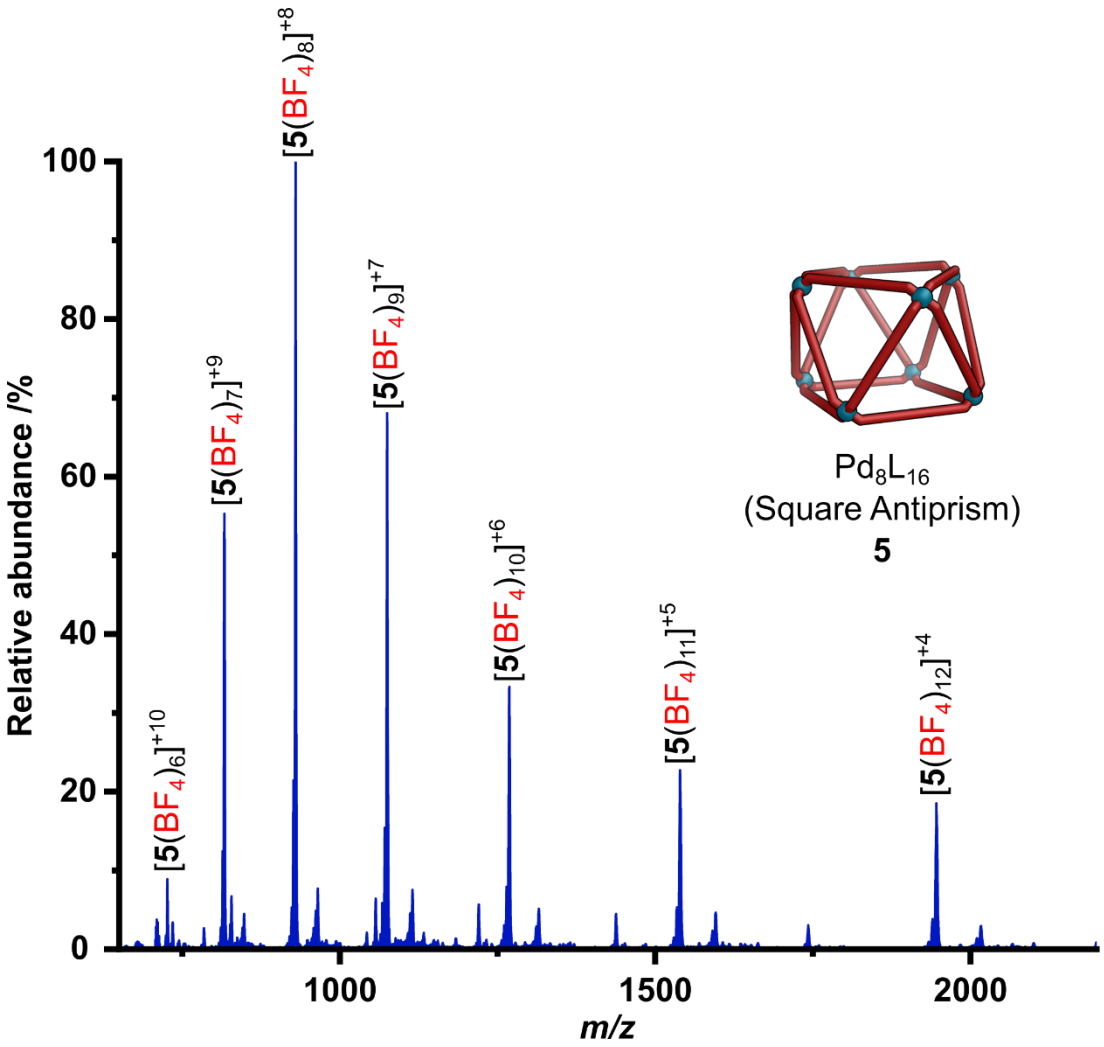

Figure S53: ESI-MS of cage **5**

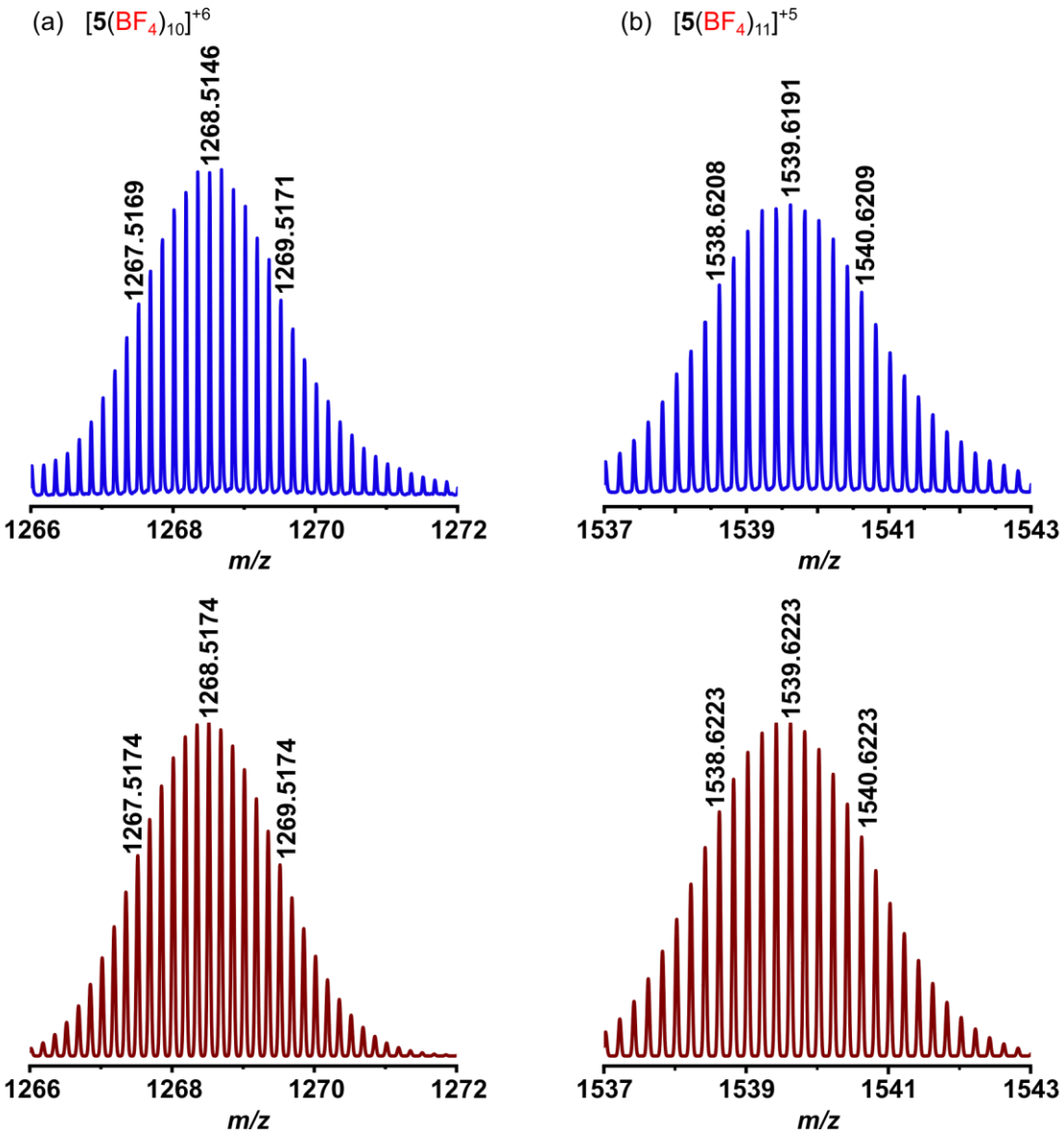

Figure S54: Isotopic distribution of selected peaks from cage **5** showing match between experimentally observed (blue) and predicted (red) patterns
(a) [**5**$(BF_4)_{10}]^{+6}$, (b) [**5**$(BF_4)_{11}]^{+5}$

S5.6 Self-assembly of $Pd_8L^1_{16}$ square antiprism 6

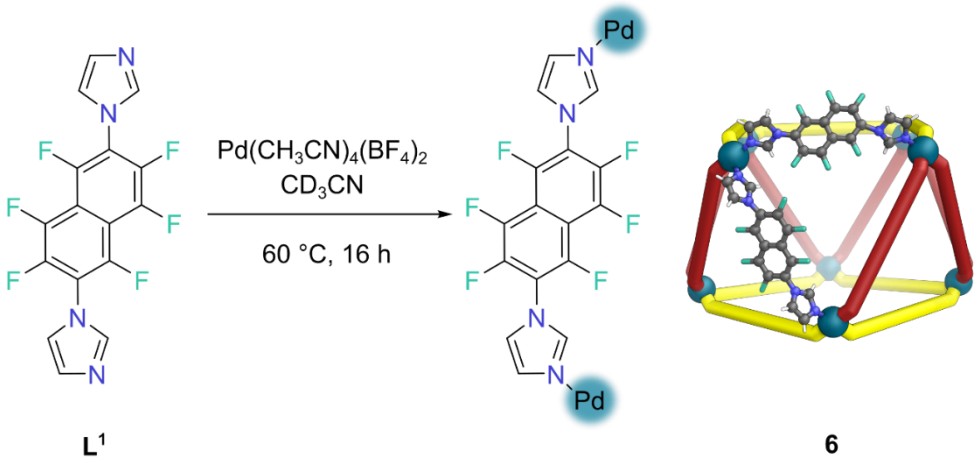

L^1 6

1,1'-(Perfluoronaphthalene-2,6-diyl)bis(1H-imidazole) **L^1** (5.00 mg, 0.0136 mmol) and $Pd(CH_3CN)_4(BF_4)_2$ (3.01 mg, 0.00679 mmol) were placed in a 1-dram (4.00 mL) vial and 0.60 mL CD_3CN was added. This mixture was then heated at 60 °C for 16 h. The resulting reaction mixture was centrifuged (3000 rpm, 5 min) and the supernatant decanted to obtain a pale-yellow solution of cage **6**.

^{1}H NMR (500 MHz, CD_3CN) δ_H: 8.60 (s, 16H), 8.40 (s, 16H), 7.74 (s, 16H), 7.65 (s, 16H), 7.57 (s, 16H), 7.51 (s, 16H).

^{19}F NMR (376 MHz, CD_3CN) δ_F: −128.43 to −128.88 (m, 32F), −144.25 to −145.39 (m, 32F), −146.31 to −146.91 (m, 32F), −151.78 (br, 13F, $^{10}BF_4$), −151.83 (br, 51F, $^{11}BF_4$).

ESI-MS (ESI, CH_3CN), *m/z*: [**6**$(BF_4)_{11}]^{5+}$ calculated 1539.6223, found 1539.6214; [**6**$(BF_4)_{10}]^{6+}$ calculated 1268.5175, found 1268.5175; [**6**$(BF_4)_9]^{7+}$ calculated 1074.8712, found 1074.8717; [**6**$(BF_4)_8]^{8+}$ calculated 929.6365, found 929.6373; [**6**$(BF_4)_7]^{9+}$ calculated 816.6761, found 816.6739.

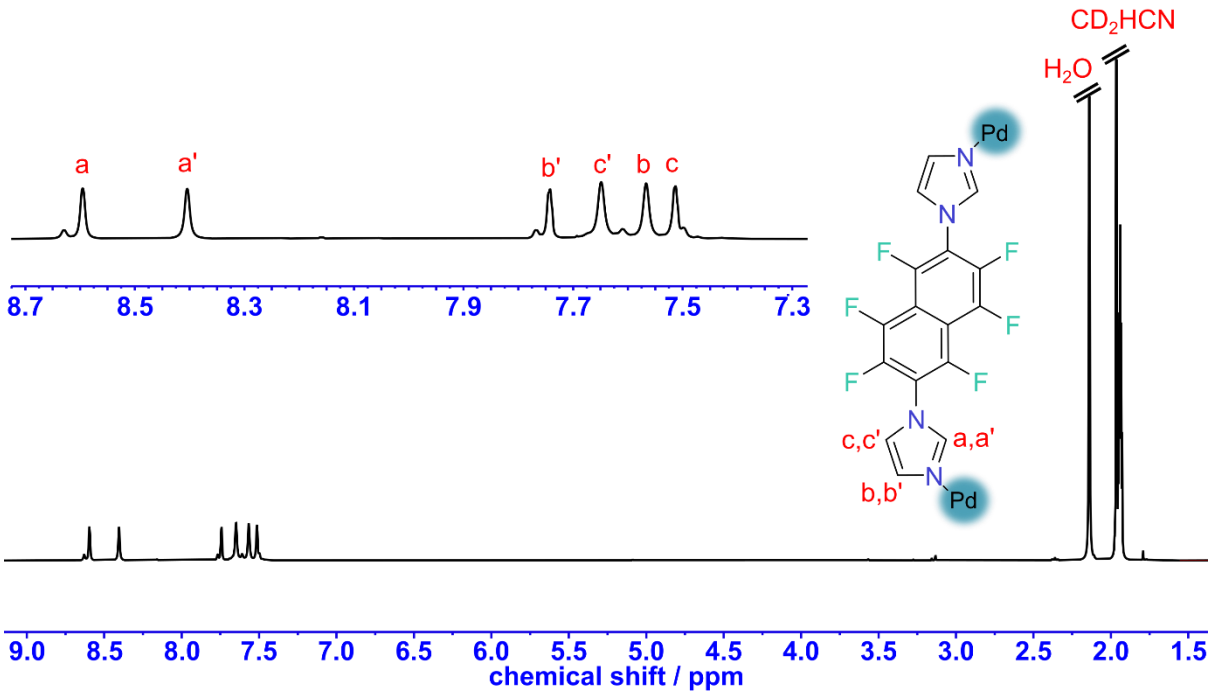

Figure S55: ^{1}H NMR spectrum of cage **6**
(400 MHz, 298 K, CD_3CN)

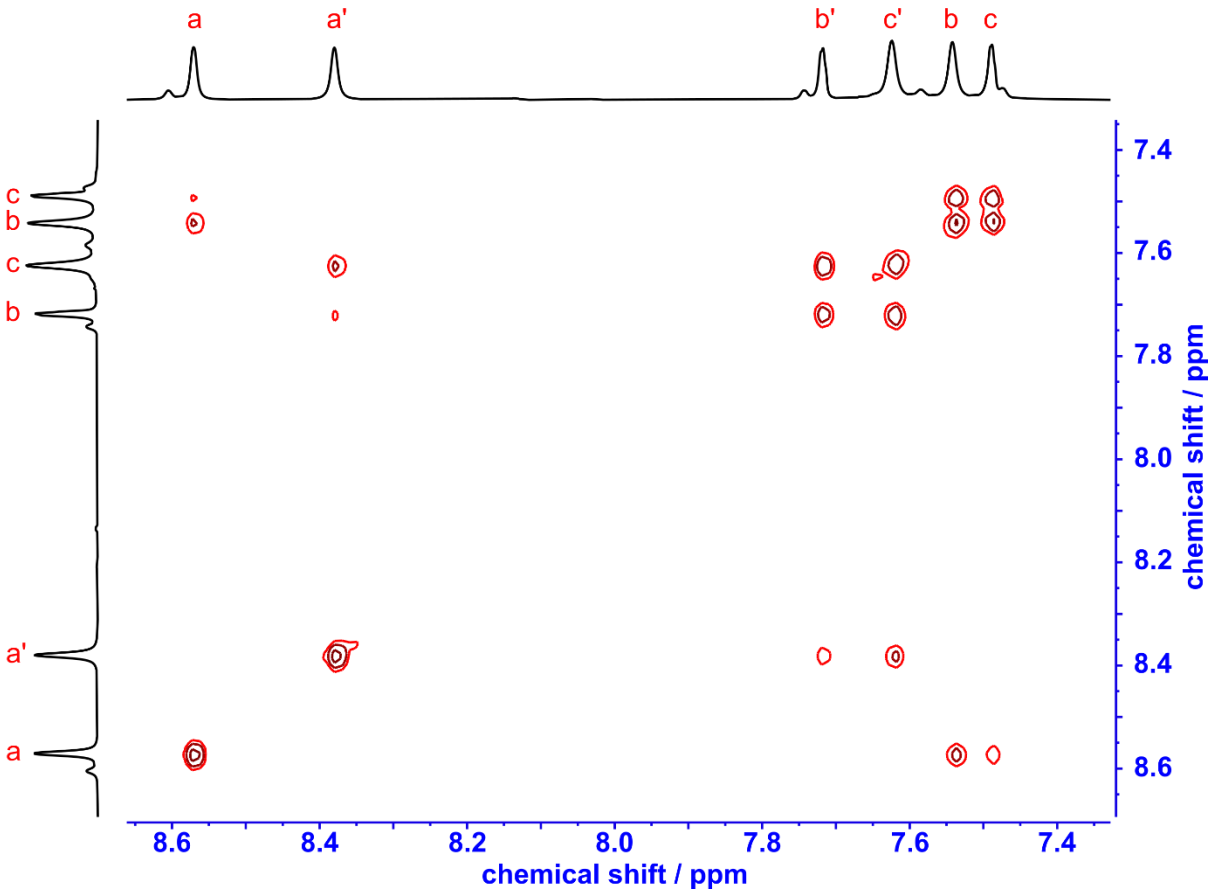

Figure S56: ^{1}H-^{1}H COSY spectrum of cage **6**
(400 MHz, 298 K, CD_3CN)

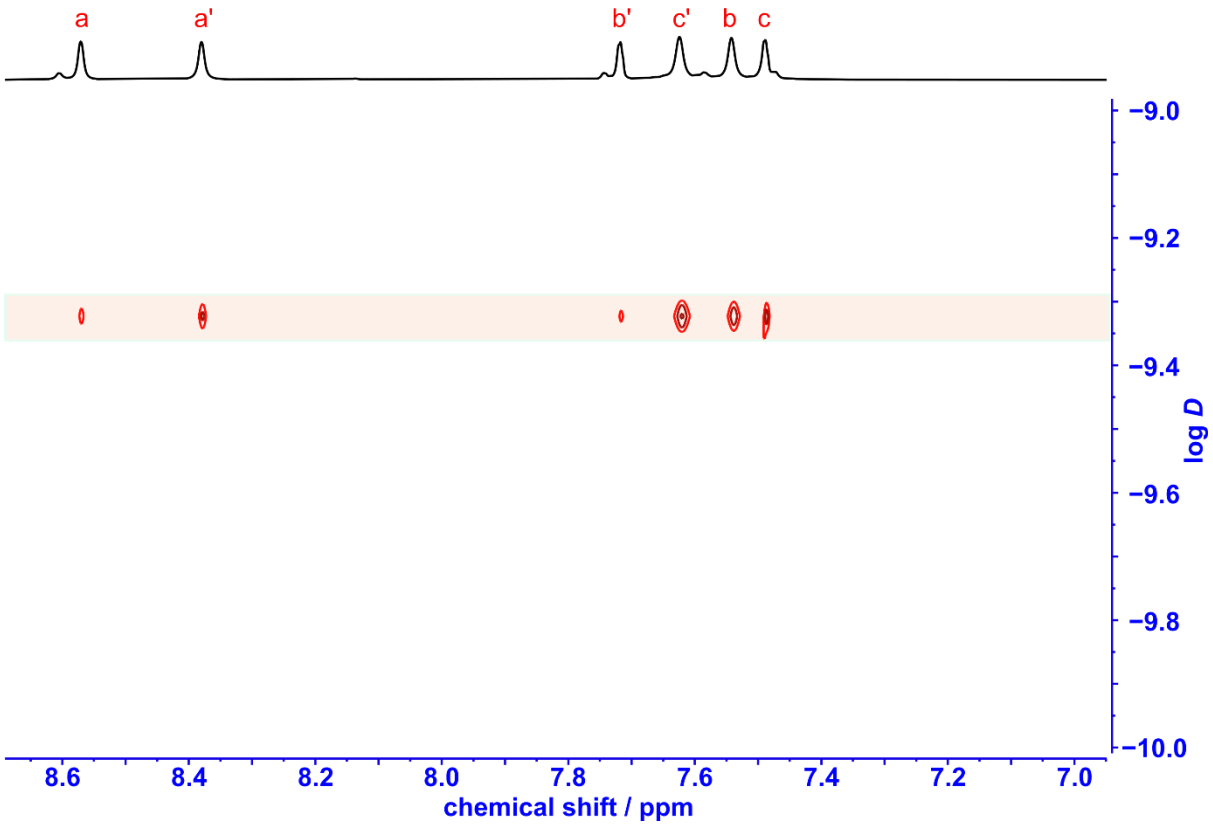

Figure S57: ^{1}H DOSY spectrum of cage **6**
(400 MHz, 298 K, CD_3CN)

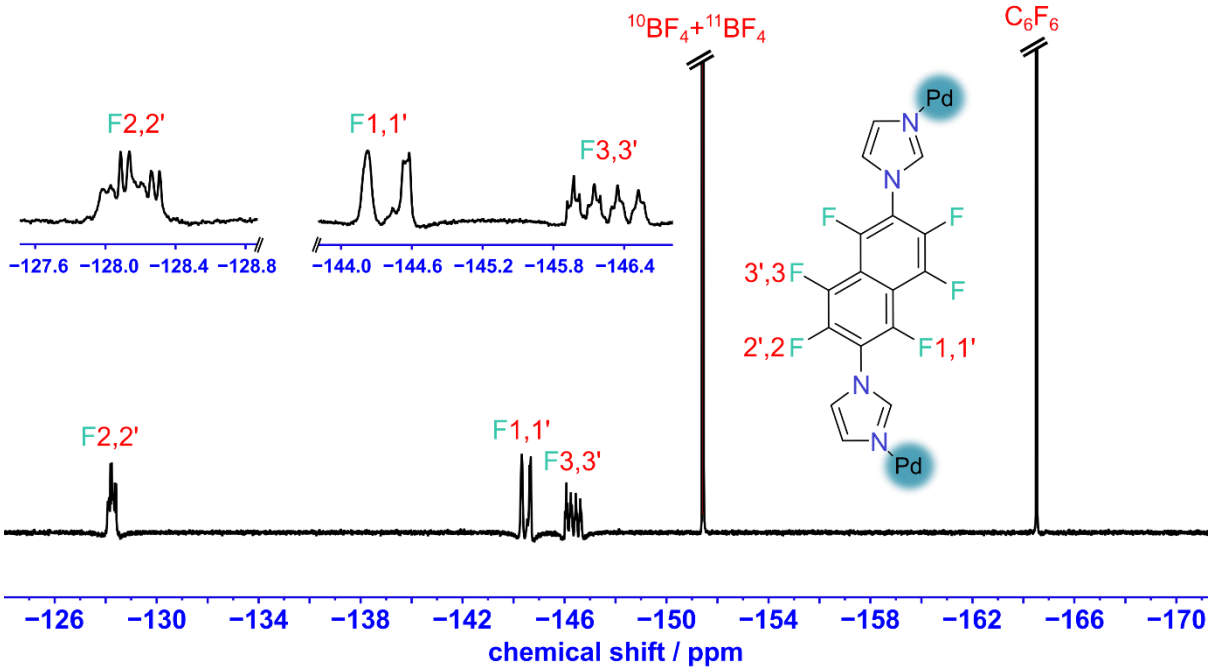

Figure S58: ^{19}F NMR spectrum of cage **6**
(376 MHz, 298 K, CD_3CN)

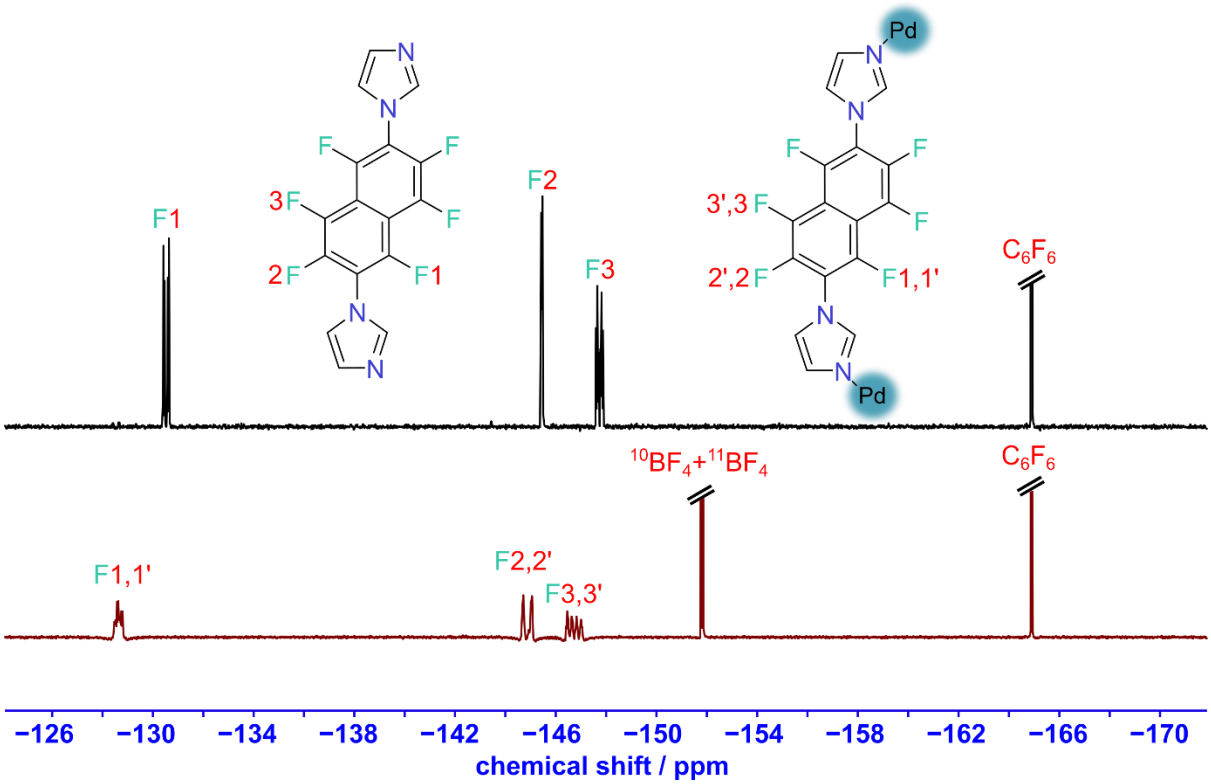

Figure S59: Stack plot of ^{19}F NMR spectra of ligand **L**^{1} (black) and cage **6** (maroon) (376 MHz, 298 K, CD_3CN)

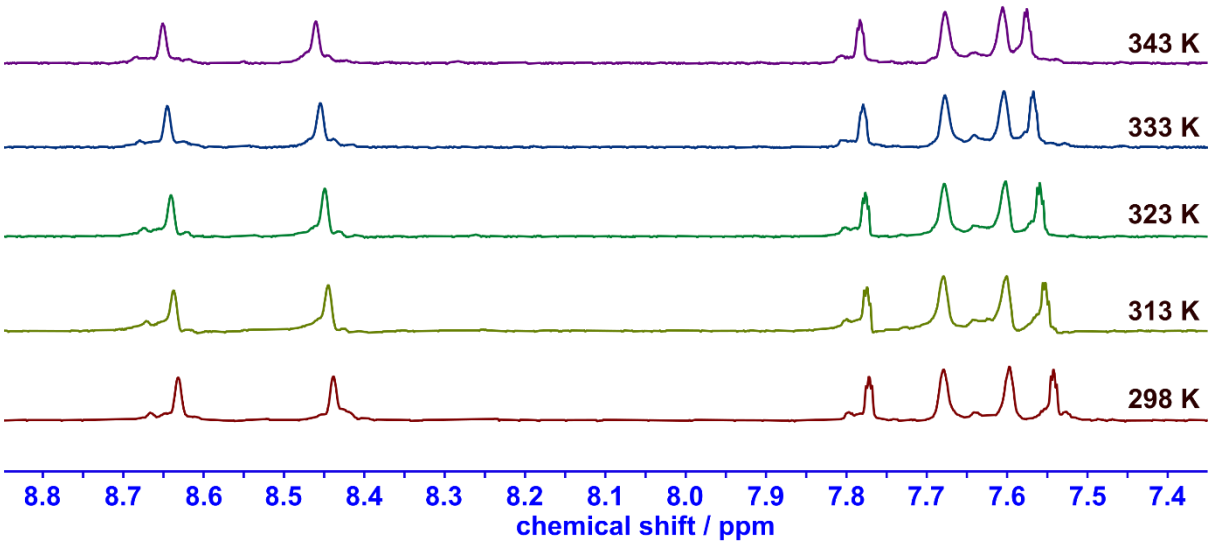

Figure S60: Variable temperature ^{1}H NMR spectra of a sample of cage **6** (400 MHz, 298 K, CD_3CN)

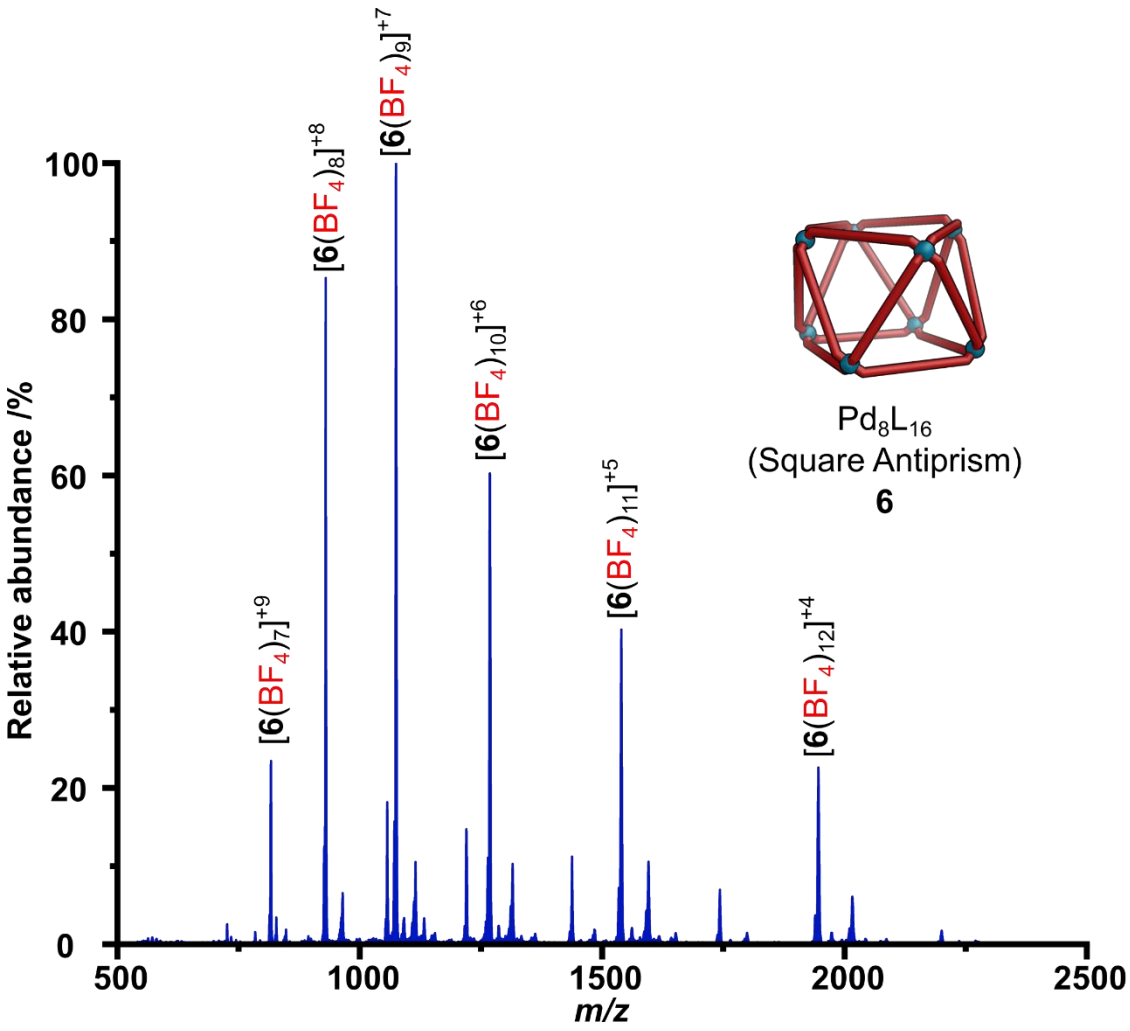

Figure S61: ESI-MS of cage **6**

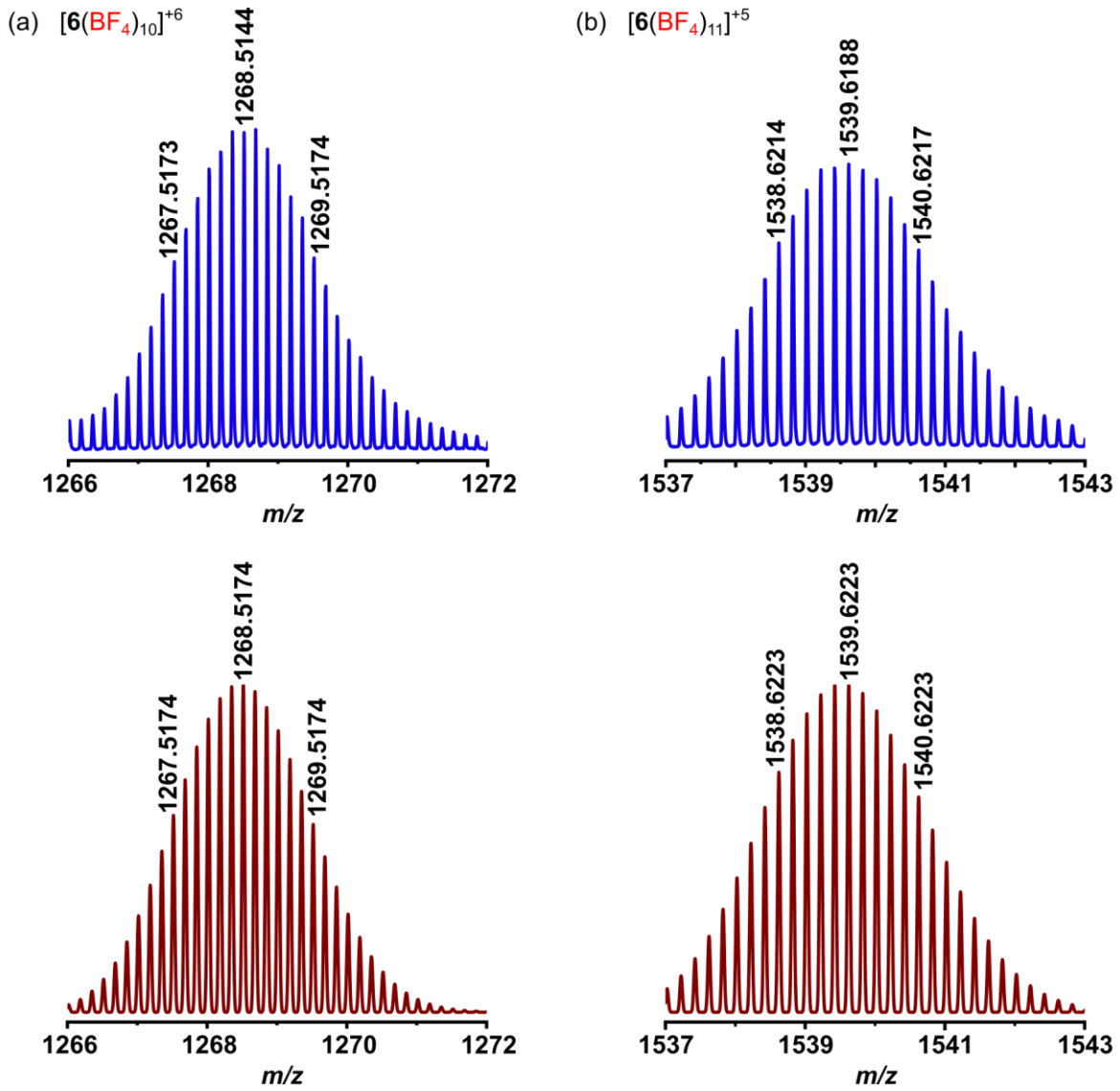

Figure S62: Isotopic distribution of selected peaks from cage **6** showing match between experimentally observed (blue) and predicted (red) patterns
(a) [**6**$(BF_4)_{10}]^{+6}$, (b) [**6**$(BF_4)_{11}]^{+5}$

S6 Stability studies of cage systems

S6.1 Cage 3 into CD_3CN

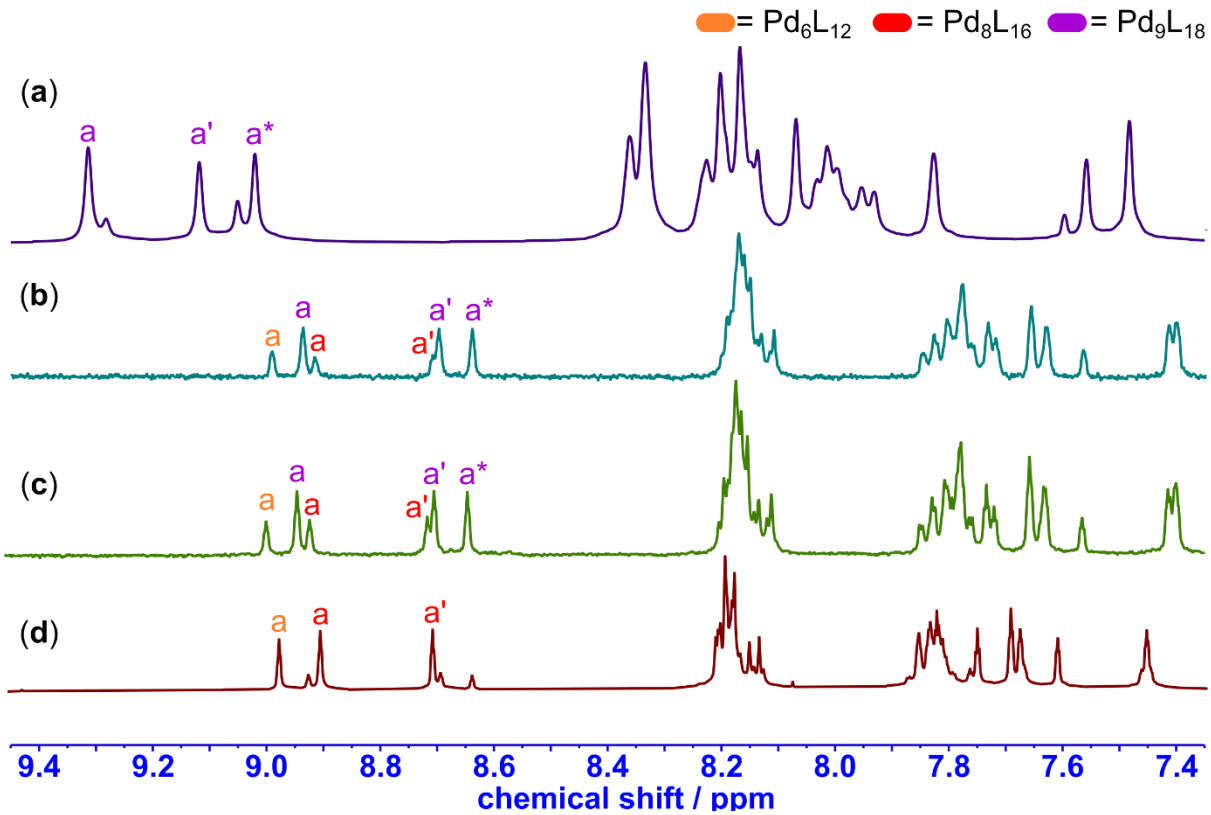

Figure S63: ^{1}H NMR analysis (400 MHz, 298 K) showing solvent effects on cage **3**. (a) spectrum of **3** in DMSO-d_6 (purple). (b) spectrum of **3** after being redissolved in CD_3CN (turquoise). (c) spectrum of **3** in CD_3CN after seven days (green). (d) spectrum of **4** and **4'** (directly synthesised in CD_3CN) (maroon).

S7 Geometric discussion

In the field of supramolecular chemistry, many authors have referred to 'symmetry' and 'imitation of nature' in the context of self-assembly, and the Tammes problem has been referenced in works such as micelle aggregation[1] and viral self-assembly.[2] The relevance of the Tammes problem to MOC self-assembly is along similar lines.

Quoting from Tammes' thesis *"[T]he symmetry of the pollen-grains arises from the closest possible arrangement… on that part of the surface where this formation is possible… [T]herefore … is not previously extant in the protoplasm, but arises only consequent on the junction of as great as possible a number of equivalent parts*". In other words, Tammes believed that symmetry was incidental to the arrangements of pollen tubes observed and did not result in them. An analogy, therefore, can be drawn to explain why Pd_nL_{2n} (n = 8 and 9) structures are described by lower symmetry point groups – that these structures too arise naturally as 'optimal arrangements'.

For the Tammes problem, the symmetry and edge lengths of the arrangement result from the optimisation process. Since there is no requirement for solutions to be tetravalent, larger numbers of n are rarely tetravalent. For Pd_nL_{2n} cages, there are additional requirements: each vertex must be tetravalent and edge lengths must be equal. This explains why the larger Pd cages diverge from the Tammes solutions.

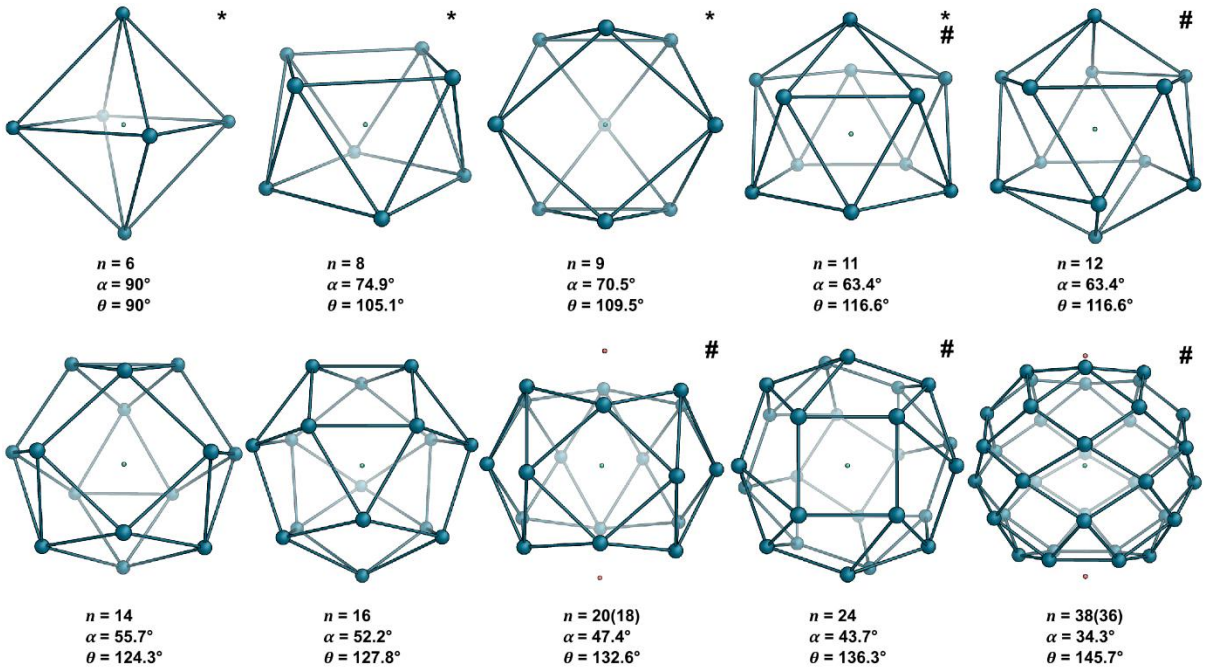

Figure S64: Tetravalent arrangements of points on a sphere that can be constructed from solutions to the Tammes Problem. * denotes solutions previously discussed in other work.[3] # denotes omission of edges or points from the Tammes solution are required to make a tetravalent arrangement.

Tables of solutions to the Tammes problem can be found online.[4-6] Solutions from which tetravalent arrangements can be constructed are given in **Figure S64**, including those that can be made by omitting edges and points. The most interesting solutions are n = 14, 16 which are both tetravalent. However, the corresponding MOCs would have to contain large numbers of unique environments, so achieving the requisite control over the self-assembly process to construct these structures will be a formidable challenge. Solutions n = 12, 24 are unique in that they can be made tetravalent by omitting edges. The resultant pseudo-icosahedron and pseudo-snubcube can be regarded as distortions of the cuboctahedron and rhombicuboctahedron respectively (and can be transformed into them, while preserving edge lengths and connectivity through twisting). Cages, topologically equivalent to the Tammes solutions n = 6, 9, 12 have also occurred in the related family of *cis*-protected $Pd_{3n}L_{2n}$ cages.[7]

S8 Derivation of Equation 3

Equation 3 can be derived using cylindrical polar coordinates, by considering two generic vectors. Consider first, two vectors in 2D polar coordinates, such that they are positioned symmetrically about the x-axis, such that γ is the angular separation between them (**Figure S65**).

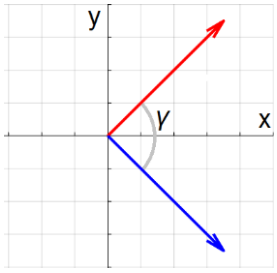

Figure S65: The angular separation, γ, between two vectors in a 2D plane

From the definition of 2D polar coordinates, it follows that:

$$x = r\cos\left(\frac{\gamma}{2}\right) \qquad (\mathbf{S1})$$

$$y = r\sin\left(\frac{\gamma}{2}\right) \qquad (\mathbf{S2})$$

Now consider an additional dimension by using 3D cylindrical polar coordinates; our two vectors $(\vec{A}, \vec{B})$ are now described by the z-axis as well (**Figure S66**).

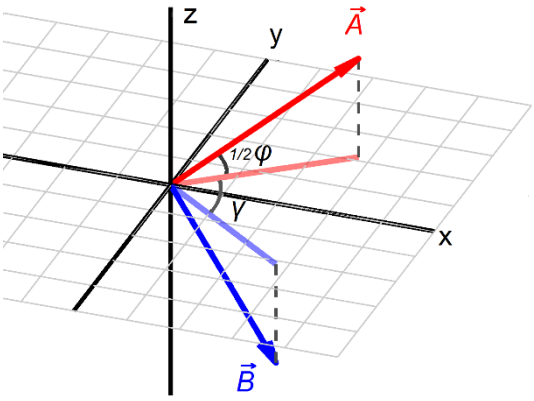

Figure S66: Addition of the third dimension describing two vectors $(\vec{A}, \vec{B})$

In cylindrical polar coordinates, the relationship between r and z is such that the following is true:

$$z = r\tan\left(\frac{\varphi}{2}\right) \qquad (\mathbf{S3})$$

Therefore, the general Cartesian coordinates of the two vectors are:

$$\vec{A} = \begin{pmatrix} r\,cos\left(\frac{\gamma}{2}\right) \\ r\,sin\left(\frac{\gamma}{2}\right) \\ z \end{pmatrix} \quad \text{and} \quad \vec{B} = \begin{pmatrix} r\,cos\left(\frac{\gamma}{2}\right) \\ -r\,sin\left(\frac{\gamma}{2}\right) \\ -z \end{pmatrix}$$

Next, an expression for θ can be found using the dot product,

$$cos(\theta) = \frac{\vec{\boldsymbol{A}} \cdot \vec{\boldsymbol{B}}}{\|\vec{\boldsymbol{A}}\|\|\vec{\boldsymbol{B}}\|}$$

Since the magnitude of a normalised vector is unity, it follows that:

$$\cos(\theta) = \vec{\boldsymbol{A}} \cdot \vec{\boldsymbol{B}}$$

Hence:

$$cos(\theta) = r^2 \cos^2\left(\frac{\gamma}{2}\right) - r^2 \sin^2\left(\frac{\gamma}{2}\right) - z^2 \qquad (\mathbf{S4})$$

Since $\vec{\boldsymbol{A}}$ and $\vec{\boldsymbol{B}}$ are normalised,

$$z^2 + r^2 = 1 \qquad (\mathbf{S5})$$

Using **Equations S3**, **S4**, and **S5**, the expression for θ in terms of γ and φ can be derived. Recall the identity,

$$cos^2(\alpha) - \sin^2(\alpha) = cos\ (2\alpha)$$

So, **Equation S4** becomes,

$$cos(\theta) = r^2 cos(\gamma) - z^2$$

Substitute in **Equation S5**,

$$cos(\theta) = r^2 cos(\gamma) - (1 - r^2)$$

Hence:

$$cos(\theta) = r^2(cos(\gamma) + 1) - 1 \qquad (\mathbf{S6})$$

Next, express r in terms of φ, by substituting **Equation S3** into **Equation S5**,

$$r^2 tan^2\left(\frac{\varphi}{2}\right) + r^2 = 1$$

$$r^2\left(tan^2\left(\frac{\varphi}{2}\right) + 1\right) = 1$$

Recalling the identity:

$$1 + \tan^2(\alpha) = sec^2\ (\alpha)$$

$$r^2 = \frac{1}{sec^2\left(\frac{\varphi}{2}\right)} = cos^2\left(\frac{\varphi}{2}\right) \qquad (\mathbf{S7})$$

Substituting **Equation S7** into **Equation S6** gives the desired **Equation 3**:

$$cos(\theta) = cos^2\left(\frac{\varphi}{2}\right)(cos(\gamma) + 1) - 1 \qquad \textbf{Equation 3}$$

Using the cosine half-angle formula, we can rearrange into the illustrative form below:

$$\theta(\gamma, \varphi) = arccos\left(\frac{(1 + cos(\gamma))(1 + cos(\varphi))}{2} - 1\right) \qquad (\mathbf{S8})$$

S9 Angular deconvolution discussion

$$\theta = \arccos\left(\frac{\overrightarrow{Pd_AN_B}\cdot\overrightarrow{Pd_DN_C}}{\left\|\overrightarrow{Pd_AN_B}\right\|\left\|\overrightarrow{Pd_DN_C}\right\|}\right) \qquad (\mathbf{1})$$

$$\varphi = \arccos\left(\frac{\overrightarrow{n_1}\cdot\overrightarrow{n_2}}{\|\overrightarrow{n_1}\|\cdot\|\overrightarrow{n_2}\|}\right) \qquad (\mathbf{2})$$

$$\theta(\gamma,\varphi) = \arccos\left(\cos^2\left(\frac{\varphi}{2}\right)(\cos(\gamma)+1)-1\right) \qquad (\mathbf{3})$$

$$\theta(\gamma,\varphi) = arccos\left(\frac{(1+cos(\gamma))(1+cos(\varphi))}{2}-1\right) \qquad (\mathbf{S8})$$

As shown by **Equation S8**, θ is symmetric with respect to exchange of γ and φ, *i.e.*,

$$\theta(\gamma,\varphi) = \theta(\varphi,\gamma)$$

for any pair of γ and φ angles. Therefore, mathematically the choice of how to define either variable is arbitrary. For example, (γ = 90°, φ = 0°) is the same as (φ = 0°, γ = 90°). Additionally, there are an infinite number of ways to deconvolute a given angle into two perpendicular 'component' angles, depending on what axes the planes are defined to be in. This complicates performing automatic deconvolution.

For the deconvolution to be chemically meaningful, these planes should correspond to features of the ligand/cage; this requires a method of identifying a 'marker' present/conserved in all crystal structures to make the deconvolution non-arbitrary. This led to the development of our method.

Conceptually when coordination vectors are discussed, we think of them with a directionality of N→Pd. This follows the convention of how a dative covalent bond is drawn and represents the direction of donation of the pair of electrons. However, for this treatment the inverse, defined in the Pd→N direction, is more mathematically intuitive. **Equation 3** can be used to describe MOCs if the Pd→N coordination vectors converge at the same point in 3D space (**Figure 2C**). This is effectively true for most ligands in the literature, but not always so for 3-pyridine (3-Py) and *N*-linked imidazole (Imd) ligands, because they can modulate their coordination angle by dihedral twisting (**Figure 2D**). For these ligands, any dihedral twisting will prevent the vectors from meeting in 3D space.

Therefore, we chose to equate the dot product of the Pd→N vectors (**Equation 1**) with θ, the 'ideal' angle required for each structure (90° for octahedron, 105.1° for square antiprism, 109.5° for tricapped triangular prism etc.). The dot product gives the angle between two vectors irrespective if they meet in 3D space. This allows φ to be defined as the dihedral angle between Pd-N-N-Pd vector (**Figure S67a**). Since each Pd→N vector will be approximately co-planar with the donor ring (3-Py/Imd), this approximates the dihedral angle between the donor

rings as well. Consequently, this means γ, the angle in the plane perpendicular to φ, corresponds to the coordination angle of the ligand if you rotated the donor rings to both be in the same plane (**Figure S67b**).

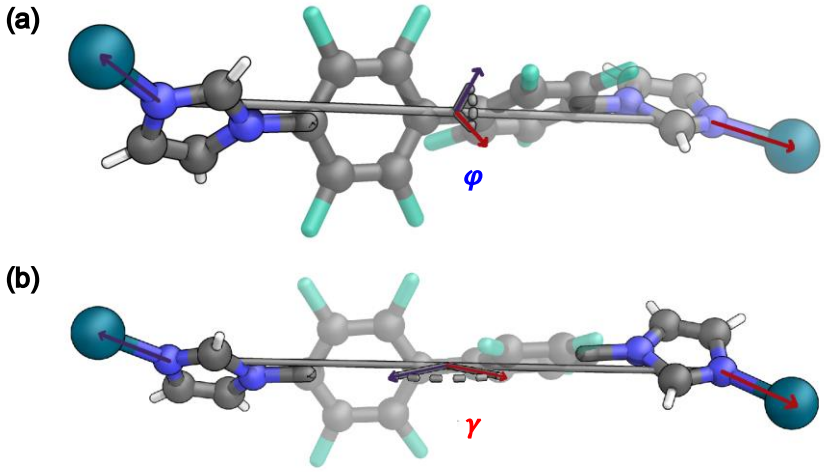

Figure S67: Illustration of: (a) the dihedral twist angle, φ. (b) the in-plane divergence angle, γ.

This approach allows the script to calculate, for most Pd_nL_{2n} cages, the mean values of θ and φ (and hence γ using **Equation 3**) from Pd and N atomic coordinates alone, using a consistent way to define the planes which γ and φ reside in. This has the additional benefit that for low quality crystal structures there is often far more certainty over the position of these atoms (due to the high scattering factor of Pd) than on many other atoms in the structure.

This approach implies the dihedral angle between Pd-N-N-Pd vectors will be near zero for planar ligands. Another advantage to this method is that a non-zero value of φ now describes distortion of the ligand away from planarity; this distortion is often present to some degree even for 'flat' aromatic ligands that are not based on 3-Py or Imd donors. For ligands containing a 3-Py/Imd-like rotatable donor group, φ just represents the dihedral angle between the donor rings.

Ligands that can vary the angle through a different mechanism are considered 'planar' under this treatment (for example, this unusual ferrocene ligand from the literature will have a near-zero φ irrespective of the degree of rotation).[8] Note that any non-zero value of φ will necessitate a rotation of adjacent Pd coordination geometries in opposite directions (**Figure S68a-c**). This is the case for all Pd_nL_{2n} cages for any value of n (**Figure S68d-e**). This would in theory alter the ideal θ value of the structure as φ changes. For example, a lantern with a non-zero dihedral twist will have an ideal angle of $\theta > 0°$. For the sake of simplicity, we have just used a fixed 'ideal' θ for each structure. The black lines in **Figure 2B** show the various combinations of the φ and γ angles that combine to give the 'ideal' value for that structure

based on the mathematical shape. A more mathematically nuanced treatment for these more specialised cases will be pursued as part of further work.

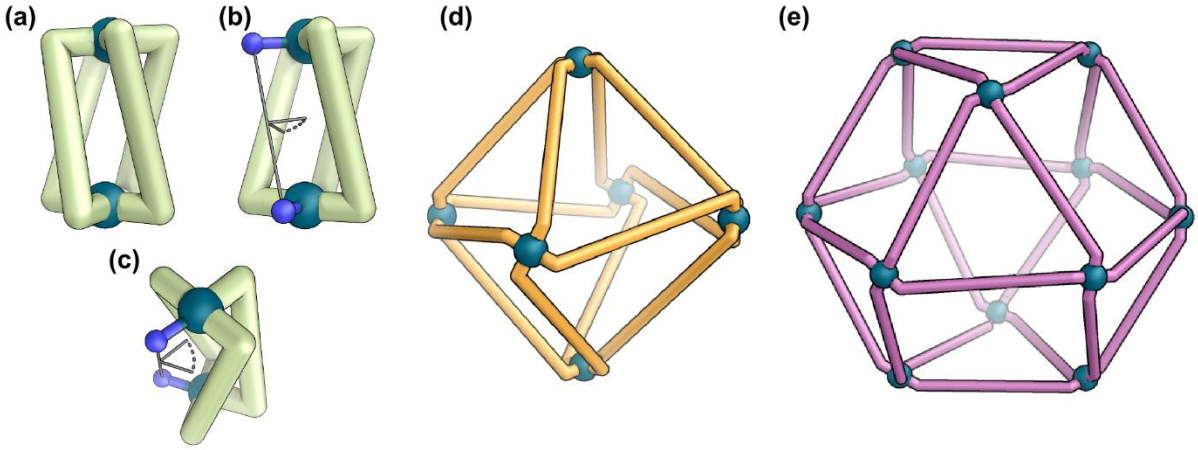

Figure S68: Cartoons illustrating the effects of dihedral twisting on the geometry of the cage. (a) Cartoon of a lantern with dihedral twisting. (b) Twist visualised with one ligand missing from a side on view. (c) Aerial view illustrating how φ is the dihedral angle between Pd-N-N-Pd. (d) Cartoon of a twisted octahedron. (e) Cartoon of a twisted cuboctahedron.

Asymmetric ligands lead to a distortion. Here, we define an asymmetric ligand as one where there is an 'offset' between the donor atoms. This is often the case for ligands with different donor groups (4-Py/3-Py/Imd) on each end. However, ligands **L**^{1} and **L**^{2}, which have asymmetric linkers, also fall under this category. Such a ligand imposes an intrinsic geometric restraint on the cage. The offset can cause a slight counter rotation of the Pd→N vectors for each adjacent Pd atom (even if the donor groups themselves are non-rotatable). This forces the dihedral angle between Pd→N vectors to be increased (**Figure S69**). Notably this dihedral twist can occur without an increase of θ.

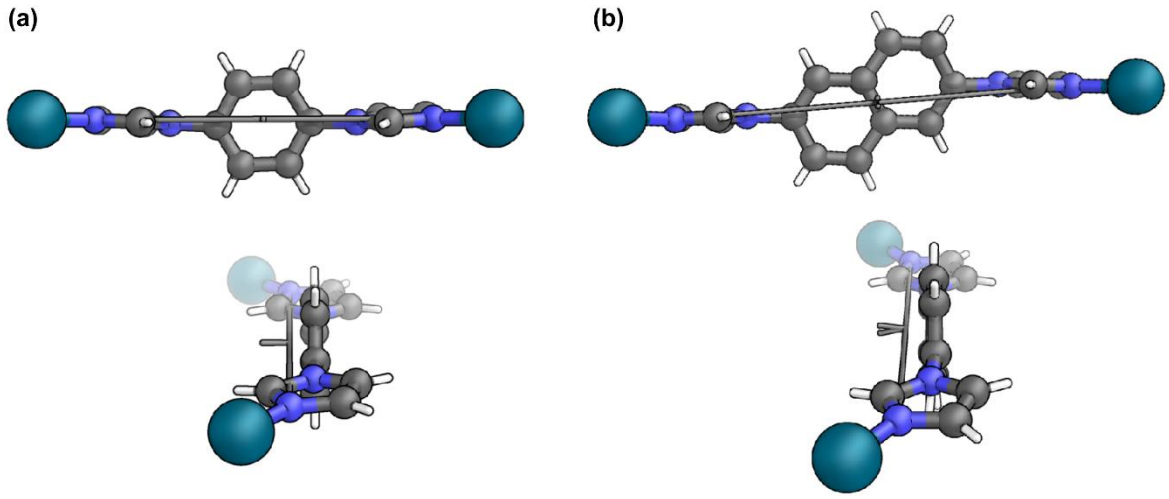

Figure S69: Models illustrating the effects of the geometric offset of a naphthalene ligand
(a) A phenyl bis-imidazole ligand with the imidazoles in a coplanar arrangement
(b) A naphthyl bis-imidazole ligand with the imidazoles in a coplanar arrangement. The offset inflates φ despite imidazoles remaining in the same plane.

S10 Plot of Structures

S10.1 Plot details

To perform the *meta*-analysis of existing Pd_nL_{2n} structures, a MATLAB script was written (see separate file of the SI for this script). Using this script requires a .cif from the SCXRD structure of the cage. To use the following MATLAB script, a MATLAB installation is required. An account can be made at https://www.mathworks.com. Many universities pay for a license, in which case an account can be made with your university email. If this is not the case, you can use the online version, which is free.

First open a .cif (or other file format) using Olex2 and remove disorder components such that each Pd atom only has four coordinating N atoms. This can usually be done with the PARTs toggle or by manual deletion. If your file name is “Test1”, use Olex2 to generate a .xyz file by typing "file Test1.xyz" into the console, then drag your file into the MATLAB folder (left of screen 'current folder').

Modify the settings below to use the name of your .xyz file and copy and paste the entire script (*e.g.*, Ctrl + A, Ctrl + C, and Ctrl + V on Windows) into the MATLAB command line and press Enter to run the script.

The script will print the angle deconvolution of your cage into the command line, then display the data on three figures. You should use these figures to check the script has detected the coordination connectivity correctly.

If the logic fails to construct connectivity correctly, manually input the connectivity below. **Figure 2D** displays the Pd and N labels for this purpose. Note: The logic typically fails when used on helicate lanterns (Pd_2L_4) with a large twist. So, these require manual input.

If you wish to access the tabulated data of each ligand on MATLAB, navigate to the “Workspace” tab on the bottom left of the screen. Then scroll down the list until you see “PdN_N_PdN_Table”. Double click on the row and the table of values will load up on screen. This table can be copied and pasted into Microsoft Excel.

S10.2 MATLAB plot output

Example outputs for this script for cages in this work can be seen in **Section S11**.

To visualise the data, values of θ, φ, and γ were plotted in 3D Cartesian coordinates. On this same plot was overlayed the surface defined by **Equation 3** (**Figure S70**). For the points to reside on this surface, θ, φ, and γ values must obey **Equation 3**. For this reason, γ_{calc} was introduced. Since deconvolutions were performed for individual ligands, and the mean values θ_{av}, φ_{av}, and γ_{av} were calculated by averaging all the ligands, the mathematical relation described by **Equation 3** is no longer exactly obeyed. γ_{calc} was therefore calculated directly from θ_{av} and φ_{av} using **Equation 3**.

Figure 2A was made by plotting θ_{av}, φ_{av}, and γ_{calc} on the surface defined by **Equation 3**, using colour-shading to denote the values of θ_{av} at that point. This was also performed in MATLAB.

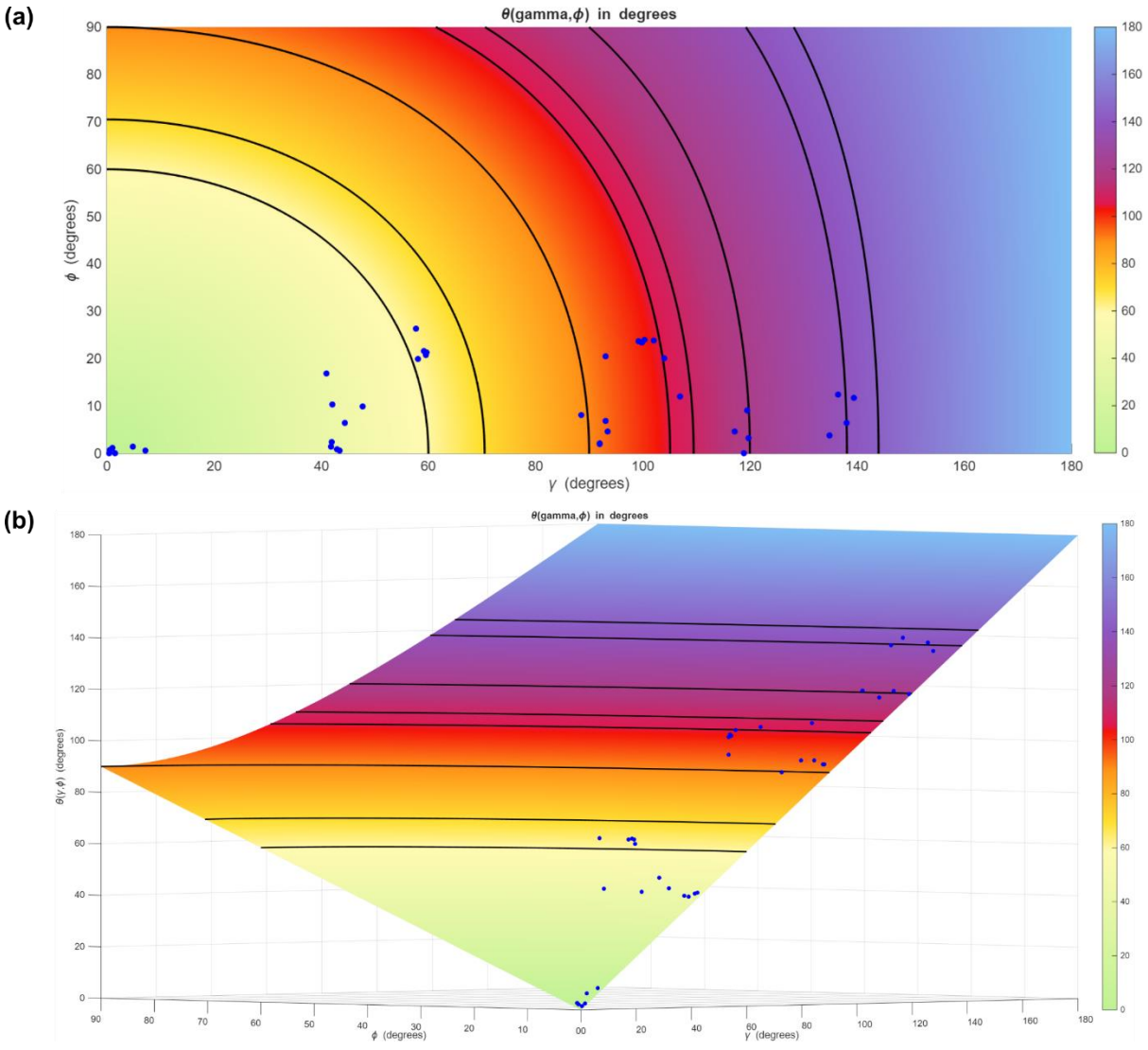

Figure S70: (a) Unannotated version of **Figure 2A** (b) 3D view of the surface described by **Equation 3**

S10.3 Data selection

During analysis of SCXRD data from the literature, there were occasions when certain parts of the data needed to be selected or excluded. For cages with disordered sections present, sensible omissions of PARTs were made. When there were multiple cages in the asymmetric unit, for larger cages, only one was chosen, whereas for smaller cages a mean was taken. For the $Pd_{30}L_{60}$ cage, due to the structure's low-resolution, conformationally unlikely ligands were manually omitted. For calculation of the cages in this work, see **Section S11**.

S10.4 Structures used in plot

Table S1: Angles for structures in plot

Structure	Donor moiety	Metal-ligand coordination angle, θ_{av}	Dihedral twist angle, φ_{av}	In-plane divergence angle, γ_{av}	In-plane divergence angle, γ_{calc}	CCDC number and ref.
Pd_2L_4	3-Pyridine	0.4°	0.0°	0.4°	0.4°	1526407 [9]
Pd_2L_4	3-Pyridine	1.0°	0.8°	0.6°	0.6°	1541717 [10]
Pd_2L_4	3-Pyridine	1.5°	0.0°	1.5°	1.5°	2256445 [11]
Pd_2L_4	3-Pyridine	1.6°	1.2°	0.9°	1.1°	1541718 [10]
Pd_2L_4	3-Pyridine	5.2°	1.4°	4.9°	5.0°	2359667 [12]
Pd_2L_4	3-Pyridine	7.2°	1.0°	7.1°	7.1°	2314589 [12]
Pd_3L_6	4-Pyridine	41.9°	1.4°	41.8°	41.9°	1817579 [13]
Pd_3L_6	Imidazole	42.1°	2.4°	42.0°	42.0°	989473 [14]
Pd_3L_6	Imidazole	43.0°	0.9°	43.0°	43.0°	1454095 [15]
Pd_3L_6	3-Pyridine	43.3°	10.4°	41.9°	42.1°	2298305 [16]
Pd_3L_6	Imidazole	43.4°	0.6°	43.4°	43.4°	1454094 [15]
Pd_3L_6	4-Pyridine	44.2°	16.9°	40.8°	41.0°	2055203 [17]
Pd_3L_6	3-Pyridine	44.8°	6.5°	44.3°	44.4°	2061340 [18]
Pd_3L_6	Benzimidazole	48.7°	10.0°	47.6°	47.7°	1529252 [19]
Pd_4L_8	3-Pyridine	61.1°	19.9°	56.4°	58.1°	297695 [20]
Pd_4L_8	3-Pyridine	62.7°	20.8°	57.4°	59.5°	2314588 [12]
Pd_4L_8	3-Pyridine	62.7°	21.7°	57.6°	59.2°	2314590 [12]
Pd_4L_8	3-Pyridine	63.0°	21.3°	57.5°	59.6°	2314587 [12]
Pd_4L_8	3-Pyridine	63.0°	26.4°	57.1°	57.7°	297117 [20]
Pd_6L_{12}	4-Pyridine	88.8°	8.2°	88.2°	88.5°	712181 [21]
Pd_6L_{12}	Benzimidazole	92.0°	2.2°	92.0°	92.0°	1829793 [22]
Pd_6L_{12}	Imidazole	92.0°	2.0°	92.0°	92.0°	2450738 [23]
Pd_6L_{12}	Imidazole	93.3°	6.9°	93.1°	93.1°	2450737 [23]
Pd_6L_{12}	Imidazole	93.5°	4.6°	93.4°	93.4°	1813498 [22]
Pd_8L_{16}	Imidazole	101.3°	23.7°	97.7°	99.2°	2487788 [24]
Pd_8L_{16}	Imidazole	104.0°	23.8°	101.0°	102.0°	2450736 [23]
Pd_9L_{18}	4-Pyridine	107.3°	12.0°	106.6°	106.8°	1022486 [3]
$Pd_{12}L_{24}$	4-Pyridine	117.2°	4.7°	117.1°	117.1°	1022433 [3]
$Pd_{12}L_{24}$	4-Pyridine	118.9°	0.0°	118.9°	118.9°	238399 [25]
$Pd_{12}L_{24}$	4-Pyridine	119.7°	9.1°	119.3°	119.5°	927643 [26]
$Pd_{12}L_{24}$	4-Pyridine	119.8°	3.3°	119.7°	119.8°	927642 [26]
$Pd_{24}L_{48}$	4-Pyridine	134.9°	3.8°	134.9°	134.9°	1033067 [27]
$Pd_{24}L_{48}$	4-Pyridine	136.8°	12.5°	136.4°	136.5°	765717 [28]
$Pd_{24}L_{48}$	4-Pyridine	138.1°	6.4°	137.9°	138.0°	860617 [29]
$Pd_{30}L_{60}$	4-Pyridine	139.6°	11.8°	139.3°	139.4°	1482268 [30]
Pd_8L_{16}	Imidazole	101.8°	23.6°	98.9°	99.8°	2512716
Pd_8L_{16}	Imidazole	102.4°	24.0°	99.4°	100.3°	2512717
Pd_9L_{18}	Imidazole	105.3°	20.1°	102.5°	103.9°	2512719
Pd_6L_{12}	Imidazole	94.8°	20.5°	92.8°	93.1°	2512718

S11 Structure angle calculations

S11.1 Cage 1

Cage **1** PART 0

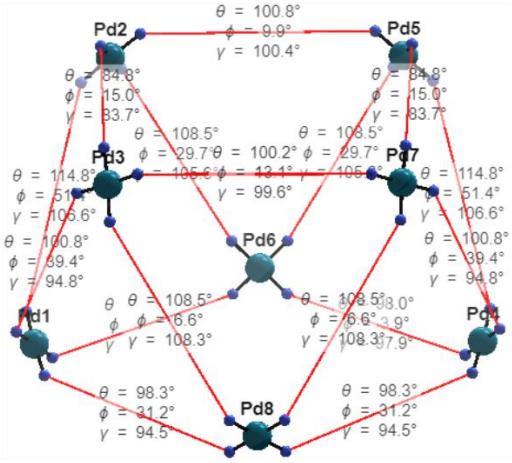

Figure S71: Output from script for Cage **1**

Table S2: Ligand angles for Cage 1

Pd-N-N-Pd edge	Metal-ligand coordination angle, θ_{av}	Dihedral twist angle, φ_{av}	In-plane divergence angle, γ_{av}
Pd2-N10-N12-Pd6	108.5°	29.7°	105.6°
Pd2-N14-N16-Pd3	84.8°	15.0°	83.7°
Pd3-N18-N20-Pd1	100.8°	39.4°	94.8°
Pd8-N22-N24-Pd1	98.3°	31.2°	94.5°
Pd3-N26-N28-Pd8	108.5°	6.6°	108.3°
Pd6-N2-N4-Pd1	98.0°	3.9°	97.9°
Pd6-N30-N32-Pd4	98.0°	3.9°	97.9°
Pd4-N34-N36-Pd5	114.8°	51.4°	106.6°
Pd5-N38-N40-Pd6	108.5°	29.7°	105.6°
Pd5-N42-N44-Pd7	84.8°	15.0°	83.7°
Pd7-N46-N48-Pd4	100.8°	39.4°	94.8°
Pd8-N50-N52-Pd4	98.3°	31.2°	94.5°
Pd7-N54-N56-Pd8	108.5°	6.6°	108.3°
Pd5-N58-N60-Pd2	100.8°	9.9°	100.4°
Pd3-N62-N64-Pd7	100.2°	13.1°	99.6°
Pd1-N6-N8-Pd2	114.8°	51.4°	106.6°

Table S3: Summary angles for Cage 1

	Metal-ligand coordination angle, θ_{av}	Dihedral twist angle, φ_{av}	In plane divergence angle, γ_{av}	Angular Separation, α_{av}
Overall mean of square/triangle edge	95.4°	15.4°	94.0°	74.3°
Standard deviation	± 6.2°	± 10.0°	± 6.3°	± 1.2°
Overall mean of triangle/triangle edge	108.2°	31.8°	103.8°	76.0°
Standard deviation	± 0.5°	± 3.5°	± 0.5°	± 3.2°
Overall mean	**101.8°**	**23.6°**	**98.9°**	**75.1°**
Standard deviation	± 8.5°	± 15.9°	± 7.6°	± 2.6°

The angles for cage **1** were calculated for an individual disorder component of the cage, since the disorder is across a symmetry element. The counterpart structure will necessarily be identical.

S11.2 Cage 2

Cage **2** PART 1 Cage **2** PART 2

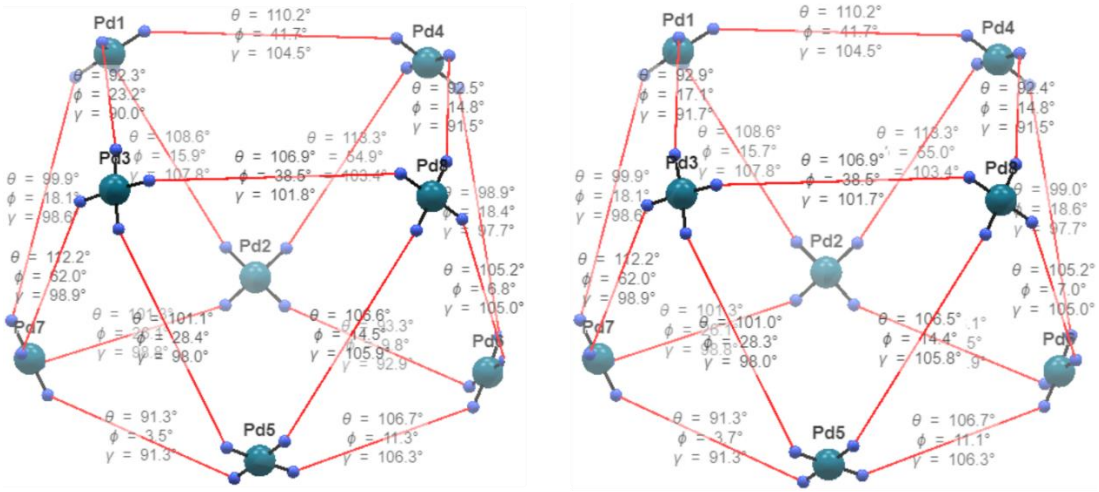

Figure S72: Output of PART 1 and PART 2 from script for Cage **2**

Table S4: Ligand angles for Cage 2 PART 1

Pd-N-N-Pd edge	Metal-ligand coordination angle, θ_{av}	Dihedral twist angle, φ_{av}	In-plane divergence angle, γ_{av}
Pd8-N11-N9-Pd4	92.5°	14.8°	91.5°
Pd8-N13-N15-Pd3	106.9°	38.5°	101.8°
Pd7-N17-N19-Pd2	101.3°	26.1°	98.8°
Pd3-N1-N3-Pd1	92.3°	23.2°	90.0°
Pd2-N21-N23-Pd6	93.3°	9.8°	92.9°
Pd6-N25-N27-Pd5	106.7°	11.3°	106.3°
Pd5-N29-N31-Pd7	91.3°	3.5°	91.3°
Pd3-N33-N35-Pd7	112.2°	62.0°	98.9°
Pd1-N37-N39-Pd7	99.9°	18.1°	98.6°
Pd1-N41-N43-Pd2	108.6°	15.9°	107.8°
Pd4-N45-N47-Pd2	113.3°	54.9°	103.4°
Pd4-N49-N51-Pd6	98.9°	18.4°	97.7°
Pd8-N53-N55-Pd6	105.2°	6.8°	105.0°
Pd8-N57-N59-Pd5	106.6°	14.5°	105.9°
Pd1-N5-N7-Pd4	110.2°	41.7°	104.5°
Pd3-N61-N63-Pd5	101.1°	28.4°	98.0°
Mean of square/triangle edge	99.3°	21.1°	97.1°
Standard deviation	± 7.3°	± 12.9°	± 6.1°
Mean of triangle/triangle edge	105.7°	27.4°	101.9°
Standard deviation	± 5.1°	± 18.9°	± 3.8°
Overall mean	**102.5°**	**24.2°**	**99.5°**
Standard deviation	± 7.1°	± 16.5°	± 5.6°

Table S5: Ligand angles for Cage 2 PART 2

Pd-N-N-Pd edge	Metal-ligand coordination angle, θ_{av}	Dihedral twist angle, φ_{av}	In-plane divergence angle, γ_{av}
Pd3-N11-N9-Pd8	106.9°	38.5°	101.7°
Pd7-N13-N15-Pd2	101.3°	26.1°	98.8°
Pd6-N17-N19-Pd5	106.7°	11.1°	106.3°
Pd1-N1-N3-Pd4	110.2°	41.7°	104.5°
Pd5-N2-1N23-Pd7	91.3°	3.7°	91.3°
Pd3-N25-N27-Pd7	112.2°	62.0°	98.9°
Pd1-N29-N31-Pd7	99.9°	18.1°	98.6°
Pd1-N33-N35-Pd2	108.6°	15.7°	107.8°
Pd4-N37-N39-Pd2	113.3°	55.0°	103.4°
Pd4-N41-N43-Pd6	99.0°	18.6°	97.7°
Pd8-N45-N47-Pd6	105.2°	7.0°	105.0°
Pd8-N49-N51-Pd5	106.5°	14.4°	105.8°
Pd3-N53-N55-Pd5	101.0°	28.3°	98.0°
Pd3-N57-N59-Pd1	92.9°	17.1°	91.7°
Pd4-N5-N7-Pd8	92.4°	14.8°	91.5°
Pd2-N61-N63-Pd6	88.1°	6.5°	87.9°
Mean of square/triangle edge	98.7°	19.9°	96.7°
Standard deviation	± 8.0°	± 13.3°	± 6.5°
Mean of triangle/triangle edge	105.7°	27.4°	101.9°
Standard deviation	± 5.1°	±18.9°	±3.8°
Overall mean	**102.2°**	**23.7°**	**99.3°**
Standard deviation	± 7.6°	± 16.7°	± 5.9°

Table S6: Summary angles for Cage 2 PART 1 and PART 2

	Metal-ligand coordination angle, θ_{av}	Dihedral twist angle, φ_{av}	In-plane divergence angle, γ_{av}	Angular separation, α_{av}
Overall mean of square/triangle edge	99.0°	20.5°	96.9°	74.5°
Standard deviation	± 7.7°	± 13.1°	± 6.3°	± 1.2°
Overall mean of triangle/triangle edge	105.7°	27.4°	101.9°	75.5°
Standard deviation	± 5.1°	± 18.9°	± 3.8°	± 1.5°
Overall mean	**102.4°**	**24.0°**	**99.4°**	**75.0°**
Standard deviation	± 7.3°	± 16.6°	± 5.8°	± 1.5°

For Cage **2**, the average value of each of the angles was calculated based on PART 1 and PART 2 of the structures due to the disordered components of PART 1 to PART 2 being 54% and 46% occupancy respectively.

S11.3 Cage 3

Cage **3** PART 1

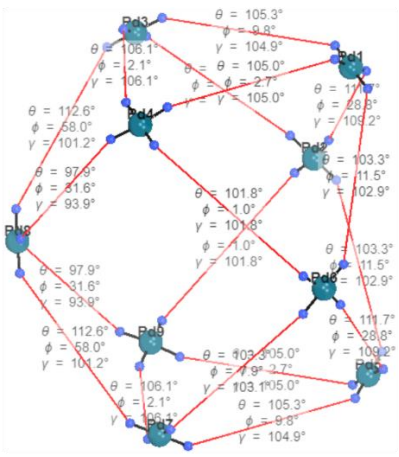

Cage **3** PART 2

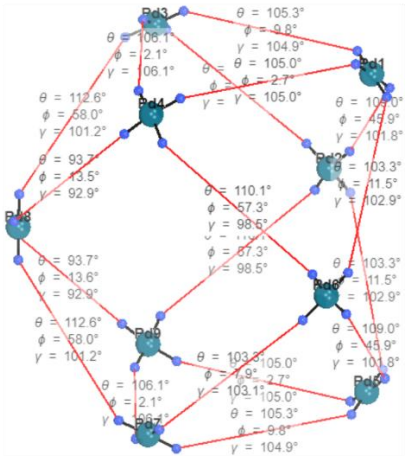

Figure S73: Output of PART 1 and PART 2 from script for Cage **3**

Table S7: Ligand angles for Cage 3 PART 1

Pd-N-N-Pd edge	Metal-ligand coordination angle, θ_{av}	Dihedral twist angle, φ_{av}	In-plane divergence angle, γ_{av}
Pd-1N11-N9-Pd4	105.0°	2.7°	105.0°
Pd6-N13-N15-Pd1	103.3°	11.5°	102.9°
Pd3-N17-N19-Pd1	105.3°	9.8°	104.9°
Pd8-N1-N3-Pd3	112.6°	58.0°	101.2°
Pd2-N21-N23-Pd3	103.3°	7.9°	103.1°
Pd4-N25-N27-Pd6	101.8°	1.0°	101.8°
Pd4-N29-N32-Pd8	97.9°	31.6°	93.9°
Pd1-N33-N36-Pd2	111.7°	28.8°	109.2°
Pd8-N37-N39-Pd7	112.6°	58.0°	101.2°
Pd7-N41-N43-Pd9	106.1°	2.1°	106.1°
Pd9-N45-N47-Pd5	105.0°	2.7°	105.0°
Pd2-N49-N51-Pd5	103.3°	11.5°	102.9°
Pd7-N53-N55-Pd5	105.3°	9.8°	104.9°
Pd6-N57-N59-Pd7	103.3°	7.9°	103.1°
Pd3-N5-N7-Pd4	106.1°	2.1°	106.1°
Pd9-N61-N63-Pd2	101.8°	1.0°	101.8°
Pd9-N65-N68-Pd8	97.9°	31.6°	93.9°
Pd5-N69-N72-Pd6	111.7°	28.8°	109.2°
Mean of bridging edge	105.1°	23.1°	102.0°
Standard deviation	± 5.3°	± 19.0°	± 4.5°
Mean of antipodal triangle edge	105.5°	4.9°	105.3°
Standard deviation	± 0.5°	± 3.5°	± 0.5°
Overall mean	**105.2°**	**17.0°**	**103.1°**
Standard deviation	± 4.4°	± 17.9°	± 4.0°

Table S8: Ligand angles for Cage 3 PART 2

Pd-N-N-Pd edge	Metal-ligand coordination angle, θ_{av}	Dihedral twist angle, φ_{av}	In-plane divergence angle, γ_{av}
Pd1-N11-N9-Pd4	105.0°	2.7°	105.0°
Pd6-N13-N15-Pd1	103.3°	11.5°	102.9°
Pd3-N17-N19-Pd1	105.3°	9.8°	104.9°
Pd8-N1-N3-Pd3	112.6°	58.0°	101.2°
Pd2-N21-N23-Pd3	103.3°	7.9°	103.1°
Pd4-N25-N27-Pd6	110.1°	57.3°	98.5°
Pd4-N29-N32-Pd8	93.7°	13.5°	92.9°
Pd1-N33-N36-Pd2	109.0°	45.9°	101.8°
Pd8-N37-N39-Pd7	112.6°	58.0°	101.2°
Pd7-N41-N43-Pd9	106.1°	2.1°	106.1°
Pd9-N45-N47-Pd5	105.0°	2.7°	105.0°
Pd2-N49-N51-Pd5	103.3°	11.5°	102.9°
Pd7-N53-N55-Pd5	105.3°	9.8°	104.9°
Pd6-N57-N59-Pd7	103.3°	7.9°	103.1°
Pd3-N5-N7-Pd4	106.1°	2.1°	106.1°
Pd9-N61-N63-Pd2	110.1°	57.3°	98.5°
Pd9-N65-N68-Pd8	93.7°	13.6°	92.9°
Pd5-N69-N72-Pd6	109.0°	45.9°	101.8°
Mean of bridging edge	105.3°	32.4°	100.1°
Standard deviation	± 6.2°	± 21.8°	± 3.5°
Mean of antipodal triangle edge	105.5°	4.9°	105.3°
Standard deviation	± 0.5°	± 3.5°	± 0.5°
Overall mean	**105.4°**	**23.2°**	**101.8°**
Standard deviation	± 5.1°	± 22.1°	± 3.8°

Table S9: Summary angles for Cage 3 PART 1 and PART 2

	Metal-ligand coordination angle, θ_{av}	Dihedral twist angle, φ_{av}	In-plane divergence angle, γ_{av}	Angular Separation, α_{av}
Overall mean of bridging edge	105.2°	27.7°	101.0°	71.0°
Standard deviation	± 5.8°	± 21.0°	± 4.2°	± 0.3°
Overall mean of antipodal triangle edge	105.5°	4.9°	105.3°	68.6°
Standard deviation	± 0.5°	± 3.5°	± 0.5°	± 0.2°
Overall mean	**105.3°**	**20.1°**	**102.5°**	**70.2°**
Standard deviation	± 4.7°	± 20.3°	± 4.0°	± 1.1°

For Cage **3,** the average value of each of the angles was calculated based on PART 1 and PART 2 of the structures due to the disordered components of PART 1 to PART 2 being 50%.

S11.4 Cage 4

Cage **4** PART 1

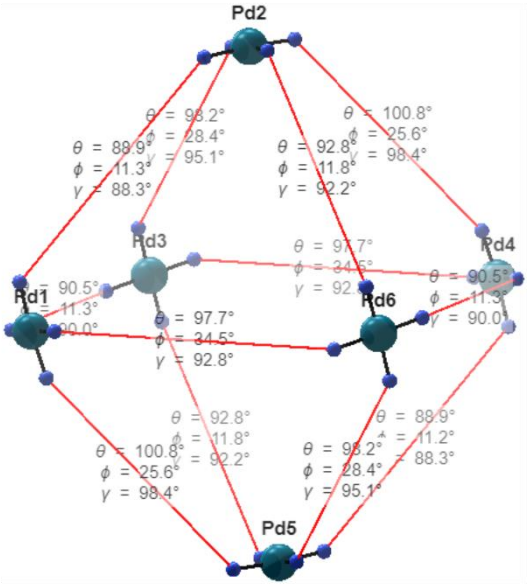

Figure S74: Output from script of Cage **4**

Table S10: Ligand angles for Cage 4

Pd-N-N-Pd edge	Metal-ligand coordination angle, θ_{av}	Dihedral twist angle, φ_{av}	In-plane divergence angle, γ_{av}
Pd2-N11-N9-Pd3	98.2°	28.4°	95.1°
Pd3-N13-N15-Pd4	97.7°	34.5°	92.8°
Pd1-N17-N19-Pd2	88.9°	11.3°	88.3°
Pd3-N1-N3-Pd5	92.8°	11.8°	92.2°
Pd2-N21-N23-Pd4	100.8°	25.6°	98.4°
Pd6-N25-N27-Pd2	92.8°	11.8°	92.2°
Pd6-N29-N31-Pd4	90.5°	11.3°	90.0°
Pd6-N33-N35-Pd5	98.2°	28.4°	95.1°
Pd6-N37-N39-Pd1	97.7°	34.5°	92.8°
Pd4-N41-N43-Pd5	88.9°	11.2°	88.3°
Pd5-N45-N47-Pd1	100.8°	25.6°	98.4°
Pd3-N5-N7-Pd1	90.5°	11.3°	90.0°

Table S11: Summary angles for Cage 4

	Metal-ligand coordination angle, θ_{av}	Dihedral twist angle, φ_{av}	In-plane divergence angle, γ_{av}	Angular Separation, α_{av}
Overall mean	**94.8°**	**20.5°**	**92.8°**	**90.0°**
Standard deviation	± 4.3°	± 9.4°	± 3.3°	± 0.8°

The angles for Cage **4** were calculated on the clear major component (PART 1) of the crystal structure. This was because the disordered components in PART 1 had an occupancy of 63% compared to an occupancy of 37% in PART 2 of the structure.

S11.5 Summary

Table S12: Summary of angles for Cages 1-4

	Metal-ligand coordination angle, θ_{av}	Dihedral twist angle, φ_{av}	In-plane divergence angle, γ_{av}	Calculated in-plane divergence angle, γ_{calc}	Angular separation, α_{av}	Calculated angular separation, α_{calc}
Cage 1	101.8° ± 8.5°	23.6°± 15.9°	98.9° ± 7.6°	99.8°	75.1° ± 2.6°	78.2°
Cage 2	102.4° ± 7.3°	24.0° ± 16.6°	99.4° ± 5.8°	100.3°	75.0°± 1.5°	77.6°
Cage 3	105.3° ± 4.7°	20.1° ± 20.3°	102.5°± 4.0°	103.9°	70.2° ± 1.1°	74.7°
Cage 4	94.8° ± 4.3°	20.5° ± 9.4°	92.8° ± 3.3°	93.1°	90.0° ± 0.8°	85.2°

γ_{calc} was calculated from θ_{av} and φ_{av} using **Equation 3**:

$$\theta_{av} = \arccos\left(\cos^2\left(\frac{\varphi_{av}}{2}\right)(\cos(\gamma_{calc}) + 1) - 1\right) \qquad (3)$$

α_{calc} was calculated from θ_{av} using the relationship:

$$\alpha_{calc} = 180 - \theta_{av}$$

Ideal α values are shown in **Figure S64**. Larger deviations of α_{calc} from α_{av} or from the 'ideal' α values can indicate distortion of the cage.

S12 Cavity modelling

Single crystal structures of the cages were used to calculate the solvent accessible void and electrostatic potential (ESP) surfaces of the cage cavities using CageCavityCalc (*C*3) tool developed by the Duarte group.[31]

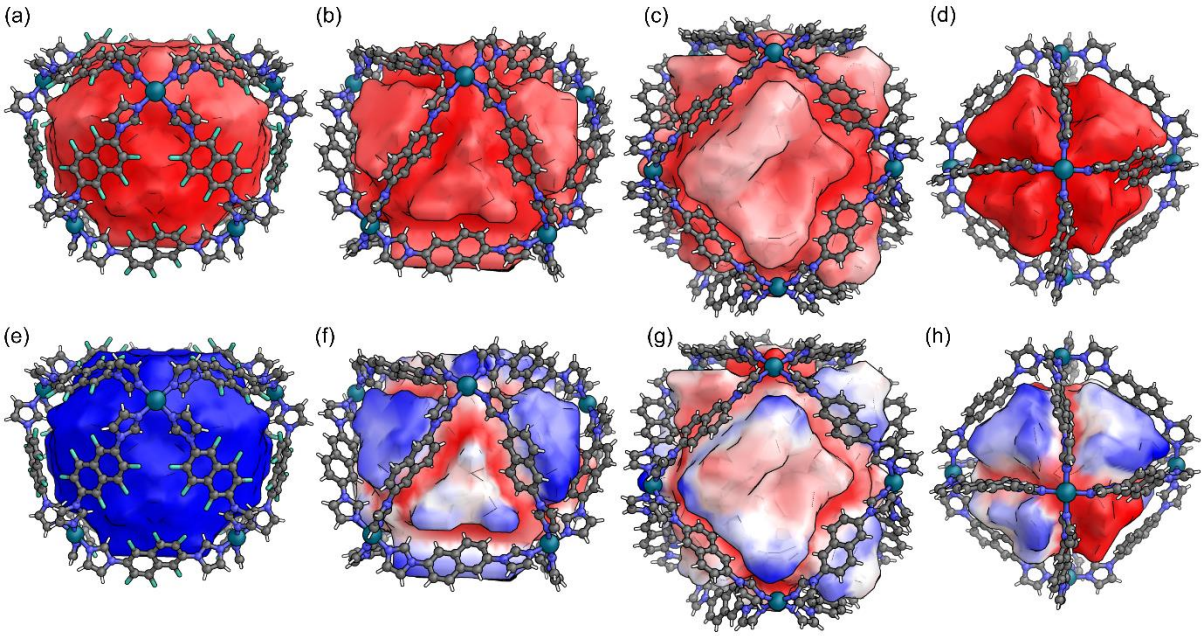

Figure S75: Computed cavity volumes for the cages: (a) cage **1**; (b) cage **2**; (c) cage **3**; and (d) cage **4**. Electrostatic potential (ESP) mapped on the cage cavities: (e) cage **1**; (f) cage **2**; (g) cage **3**; and (h) cage **4**. For the ESP figures red = positive and blue = negative.

Table S13: Computed cavity diameters and volumes of cages

Cage	Diameter / Å	Volume / Å^3
1	19.6	3954
2	19.3	3746
3	20.8	4962
4	15.1	1819

S13 X-ray crystallography

Single crystals were selected and mounted using Fomblin® (YR-1800 perfluoropolyether oil) on a polymer-tipped MiTeGen MicroMountTM. Crystals **2**, **L¹**, and **L²** were cooled rapidly to 120 K in a stream of cold N_2 using an Oxford Cryosystems open flow cryostat.[32] Crystals **1**, **3**, and **4** were rapidly cooled in liquid nitrogen for shipping to Diamond Light Source and were cooled to 100 K in a stream of cold nitrogen during data acquisition using an Oxford Cryosystems open flow cryostat. Single crystal X-ray diffraction data for **2** was collected on an XtaLAB PRO MM007 (PILATUS3 R 200K Hybrid Pixel Array detector, mirror-monochromated Cu-K_α radiation source; λ = 1.54184 Å, ω scans). Single crystal X-ray diffraction data for **L¹** and **L²** were collected on an Oxford Diffraction GV1000 (TitanS2 CCD area detector, mirror-monochromated Cu-K_α radiation source; λ = 1.54184 Å, ω scans). Cell parameters were refined from the observed positions of all strong reflections and absorption corrections were applied using a Gaussian numerical method with beam profile correction (CrysAlisPro).[33] X-ray diffraction data for **1, 3**, and **4** were collected in Experiment Hutch 1 (EH1) of Beamline I19, at Diamond Light Source.[34] The data were collected at a wavelength of 0.6889 Å on a Fluid Film Devices 3-circle fixed-chi diffractometer using a Dectris Pilatus 2M detector. The collected frames were integrated using XIA26 software.[35]

Structures were solved within Olex2[36] by dual space iterative methods (SHELXT)[37] and all non-hydrogen atoms refined by full-matrix least-squares on all unique F^2 values with anisotropic displacement parameters (SHELXL).[38] Hydrogen atoms were refined with constrained riding geometries and thermal parameters linked to U_{iso} of their parent atoms. Hydrogen atoms were refined both freely (see specific crystal structure and refinement details section for each crystal) and with constrained riding geometries and thermal parameters linked to U_{iso} of their parent atoms. Structures were checked with checkCIF.[39] CCDC 2512716 (cage **1**); CCDC 2512717 (cage **2**); CCDC 2512719 (cage **3**); CCDC 2512718 (cage **4**); CCDC 2512720 (ligand **L¹**); and 2512721 (ligand **L²**) contain the supplementary data for these compounds. These data can be obtained free of charge from The Cambridge Crystallographic Data Centre via www.ccdc.cam.ac.uk/data_request/cif.

Table S14. Experimental details for cages **1**, **2**, **3** and **4**, and ligands **L**[1] and **L**[2]

	1	**2**	**3**	**4**	**L**[1]	**L**[2]
Chemical formula	$C_{256}H_{96}F_{96}N_{64}Pd_8 \cdot 5(C_2H_6OS) \cdot 4(NO_3) \cdot 16[NO_3] \cdot 60[C_2H_6SO] \cdot 20[H_2O]$	$C_{256}H_{192}N_{64}Pd_8 \cdot 4(NO_3) \cdot 12[NO_3] \cdot 50[C_2H_6SO] \cdot 30[H_2O]$	$C_{288}H_{216}N_{72}Pd_9 \cdot 6(BF_4) \cdot 12[BF_4] \cdot 50[C_2H_6SO] \cdot 50[C_2H_3N] \cdot 30[H_2O]$	$C_{192}H_{144}N_{48}Pd_6 \cdot 12.016(BF_4) \cdot 7.5(C_2H_3N) \cdot 4(C_2N) \cdot 30[C_2H_3N]$	$C_{16}H_6F_6N_4$	$C_{16}H_{12}N_4$
M_r	13421.98	10454.94	13705.04	6496.73	368.25	260.30
Crystal system, space group	Monoclinic, $C2/m$	Triclinic, $P\bar{1}$	Monoclinic, $C2/c$	Monoclinic, $P2_1/c$	Monoclinic, $P2_1/n$	Triclinic, $P\bar{1}$
Temperature / K	100	120	100	100	120	120
a, b, c / Å	36.9973 (4), 47.4613 (4), 32.3889 (4)	28.3016 (5), 29.7763 (5), 37.7725 (6)	45.8439 (6), 46.5554 (7), 30.9406 (4)	19.8168 (2), 24.7689 (3), 32.4170 (4)	9.0753 (2), 7.8379 (2), 9.8556 (2)	9.5138 (5), 10.9853 (6), 13.3209 (7)
α, β, γ / °	90, 91.359 (1), 90	96.045 (1), 107.518 (2), 109.872 (2)	90, 90.243 (1), 90	90, 95.1105 (11), 90	90, 106.111 (2), 90	74.016 (5), 83.910 (4), 65.911 (5)
V / Å^3	56857.0 (10)	27772.1 (9)	66035.3 (16)	15848.3 (2)	673.51 (3)	1221.78 (12)
Z	4	2	4	2	2	4
Radiation type	Synchrotron, 0.6889 Å	Cu K_α	Synchrotron, 0.6889 Å	Synchrotron, 0.6889 Å	Cu K_α	Cu K_α
μ / mm^{-1}	0.56	4.43	0.55	0.40	1.52	0.70
Crystal size / mm	0.17 × 0.14 × 0.06	0.21 × 0.19 × 0.09	0.14 × 0.08 × 0.08	0.14 × 0.14 × 0.14	0.16 × 0.1 × 0.04	0.13 × 0.06 × 0.03
Diffractometer	Fluid Film Devices	XtalLAB PRO *MM007*, PILATUS3 R 200K	Fluid Film Devices	Fluid Film Devices	SuperNova, Titan S2	SuperNova, Titan S2
T_{min}, T_{max}	0.872, 1.0	0.473, 1.000	0.869, 1.000	0.827, 1.000	0.792, 1.000	0.855, 1.000
No. of measured, independent and observed [$I > 2\sigma(I)$] reflections	166519, 19899, 11612	248924, 43590, 26500	136864, 15705, 10847	270490, 48316, 26217	9366, 1321, 1205	18935, 4749, 3964
R_{int}	0.064	0.070	0.045	0.044	0.025	0.029
(sin $\theta/\lambda)_{max}$ / Å^{-1}	0.435	0.455	0.385	0.714	0.618	0.618
$R[F^2 > 2s(F^2)]$, $wR(F^2)$, S	0.116, 0.349, 1.26	0.125, 0.385, 1.45	0.132, 0.394, 1.66	0.077, 0.235, 0.96	0.030, 0.086, 1.06	0.035, 0.094, 1.03
No. of reflections	19899	43590	15705	48316	1321	4749
No. of parameters	2271	3079	1852	1650	118	361
No. of restraints	4770	10559	4230	3348	0	0
$\Delta\rho_{max}$, $\Delta\rho_{min}$ / e Å^{-3}	0.77, −0.56	1.46, −0.83	1.31, −0.62	2.42, −0.94	0.25, −0.18	0.26, −0.21
CCDC	2512716	2512717	2512719	2512718	2512720	2512721

S13.1 Single crystal structure of $Pd_8L^1_{16}$ square antiprism 1

Single crystals of cage **1** were grown *via* slow vapour diffusion of EtOAc into DMSO. A suitable crystal was selected and mounted using Fomblin (YR-1800 perfluoropolyether oil) on a Fluid Film Devices diffractometer. The crystal was kept at 100(2) K during data collection.

S13.1.1 Specific crystal structure and refinement details for 1

The crystal of a large, porous supramolecular metal-ligand coordination cage diffracted moderately well at low resolution; however, the diffraction intensity decreased markedly at higher resolutions, with a diffraction limit of 1.15 Å despite the use of synchrotron radiation and multiple collections from several crystallisation attempts. Consequently, the data used for refinement were truncated to this resolution limit. Due to the limited resolution, the data-to-parameter ratio in the refinement was 8.76, and extensive restraints were applied to obtain a chemically sensible model.

Rigid bond and similarity restraints were applied to all isotropic and anisotropic displacement parameters in the structure (RIGU, SIMU). All ligands in the structure were restrained to have idealised geometries with target values generated by Grade2 (Global Phasing Limited)[40] (DFIX, DANG, FLAT). The geometries of the dimethylsulfoxide solvent residues were restrained to have target values taken from the Olex2 FragmentDB too (DFIX). The geometries of the nitrate anions were restrained to be similar, symmetrical, and planar (SADI, FLAT). Ligands I and J are each conformationally disordered over a mirror plane symmetry element and are necessarily modelled at half-occupancy for each component.

Large regions of the structure both inside and outside the cage molecule contained diffuse electron density for which chemically sensible models could not be developed, hence, the Olex2 Solvent Mask routine was applied to the data. The contents of the masked regions were estimated to firstly contain the eight nitrate anions per asymmetric unit necessary to balance the charge of the structure and secondly a mixture of the crystallisation solvent dimethylsulfoxide and water sufficient to match the estimated electron count and void volume.

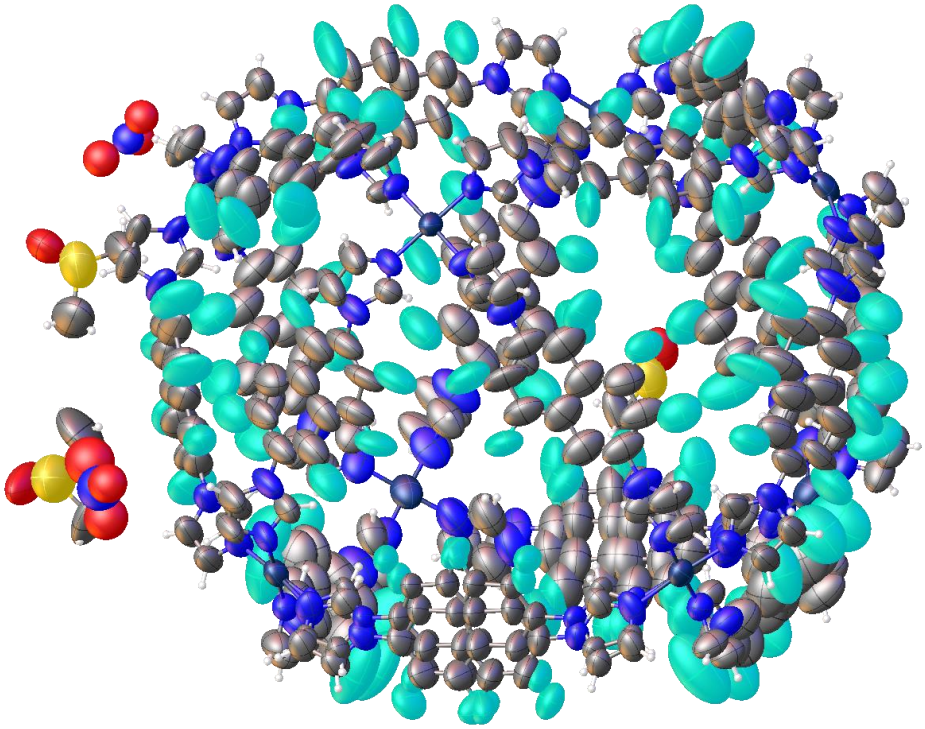

Figure S76: Image of **1** at 50% ellipsoids

S13.2 Single crystal structure of $Pd_8L^2_{16}$ square antiprism 2

Single crystals of cage **2** were grown *via* slow vapour diffusion of EtOAc into DMSO. A suitable crystal was selected and mounted using Fomblin (YR-1800 perfluoropolyether oil) on a XtalLAB PRO MM007, PILATUS3 R 200K diffractometer. The crystal was kept at 120(2) K during data collection.

S13.2.1 Specific crystal structure and refinement details for 2

The crystal of a large, porous supramolecular metal-ligand coordination cage diffracted well at low resolution; however, the diffraction intensity decreased markedly at higher resolutions, with a diffraction limit of 1.10 Å. Consequently, the data used for refinement were truncated at this high-resolution limit. Due to the limited resolution, the data-to-parameter ratio in the refinement was 14.2, and extensive restraints were applied to obtain a chemically sensible model. Attempts to collect higher-quality, higher-resolution data using synchrotron radiation were unsuccessful; therefore, the data presented here represent the best obtained.

Rigid bond and similarity restraints were applied to all isotropic and anisotropic displacement parameters in the structure (RIGU, SIMU). Atoms of nitrate anions and ligand naphthyl moieties that were disordered (ligands A/X and F/Y) or poorly defined in the electron density map (ligands O and P) were refined with isotropic displacement parameters. The anisotropic displacement parameters of carbon atoms C24N and C25N were restrained to have more isotropic character (ISOR).

The geometries of all imidazole moieties in the structure were restrained to be similar (SAME). All naphthyl ligands in the structure were restrained to have idealised geometries with target values generated by Grade2 (Global Phasing Limited) (DFIX, DANG, FLAT). Conformational disorder was modelled for ligands A and F where in each case the orientations of the 2,6-substituted naphthyl moieties are flipped with respect to the pendent imidazole rings. The occupancies of the respective disorder component pairs were refined and constrained to sum to unity resulting in values of 0.54(1) and 0.58(1) for the respective major components. The geometries of the disordered ligands were restrained to idealised geometries with target values generated by Grade2 (Global Phasing Limited) (DFIX, DANG, FLAT). The disordered naphthyl- and imidazolyl-moieties of ligands F and Y were restrained to be co-planar (FLAT). The geometries of the nitrate anions were restrained to be similar, symmetrical, and FLAT (SAME, FLAT).

Inspection of the Fcalc map for the final refined structure reveals variable correlations between the models and map distributions for some of the central portions of ligand naphthyl moieties. In particular, disordered ligands A and F, and ligands O and P show sub-atomic resolution correlations in these regions. It is possible that the poorer correlations in these parts of the

structure are a consequence of deficiencies in the modelling of the disorder, or absence of disorder models where disorder may be present. The heavily restrained models in these regions of the structure have been carefully examined to ensure that they represent the most chemically plausible ligand conformations considering knowledge of the composition and overall connectivity of the supermolecule gleaned from synthetic knowledge and other analytical methods. Despite the ambiguity in the electron density map in these specific regions of the structure, the overall composition, topology, and geometry around metal centres can be very confidently concluded. For the ligands with poor atomic resolution mentioned above, detailed geometries of the naphthyl moieties including torsion angles and bonds distances are not sufficiently well defined enough to be analysed.

Large regions of the structure both inside and outside the cage molecule contained diffuse electron density for which chemically sensible models could not be developed, hence, the Olex2 Solvent Mask routine was applied to the data. The contents of the masked regions were estimated to firstly contain the 12 nitrate anions necessary to balance the charge of the structure and secondly a mixture of the crystallisation solvents dimethylsulfoxide and water sufficient to match the estimated electron count and void volume.

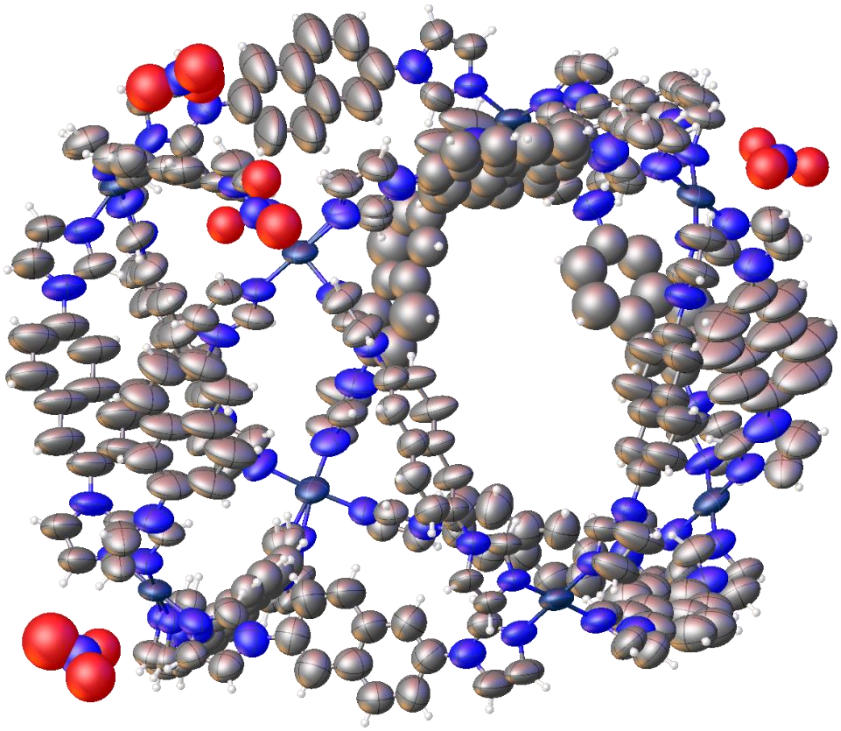

Figure S77: Image of **2** at 50% ellipsoids

S13.3 Single crystal structure of $Pd_9L^2_{18}$ tricapped trigonal prism 3

Single crystals of cage **3** were grown *via* slow vapour diffusion of *i*Pr_2O into a DMSO/CH_3CN (1:8) solution. A suitable crystal was selected and mounted using Fomblin (YR-1800 perfluoropolyether oil) on a Fluid Film Devices diffractometer. The crystal was kept at 100(2) K during data collection.

S13.3.1 Specific crystal structure and refinement details for 3

The crystal of a large, porous supramolecular metal-ligand coordination cage diffracted well at low resolution; however, the diffraction intensity decreased markedly at higher resolutions, with a diffraction limit of 1.30 Å despite the use of synchrotron data and multiple collections from several crystallisation attempts. Consequently, the data used for refinement were truncated at this high-resolution limit. Due to the limited resolution, the data-to-parameter ratio in the refinement was 8.50, and extensive restraints were applied to obtain a chemically sensible model.

Rigid bond and similarity restraints were applied to all isotropic and anisotropic displacement parameters in the structure (RIGU, SIMU). Atoms of tetrafluoroborate anions and ligand naphthyl moieties that were disordered (ligands N/O, P/Q, and R/S) were refined with isotropic displacement parameters. The imidazole atoms of disordered ligands O/P were modelled with isotropic displacement parameters.

All ligands in the structure were restrained to have idealised geometries with target values generated by Grade2 (Global Phasing Limited) (DFIX, DANG, FLAT). Conformational disorder was modelled for ligands N/O, P/Q, and R/S where in each case the orientations of the 2,6-substituted naphthyl moieties are flipped with respect to the pendent imidazole rings. The occupancies of the respective disorder components were fixed at values of 0.5 respectively in each case. The naphthyl moiety and naphthyl-imidazole moiety pair of ligand O were additionally restrained to have planar geometries (FLAT) to aid refinement of a sensible model.

The geometries of the tetrafluoroborate anions were restrained to have idealised 1,2 and 1,3-bond distances taken from the provided geometry from the Olex2 FragmentDB (DFIX).

Inspection of the Fcalc map for the final refined structure reveals variable correlations between the models and map distributions for some of the central portions of ligand naphthyl moieties. In particular, disordered ligands N/O and P/Q, and ligand D show sub-atomic resolution correlations in these regions. It is possible that the poorer correlations in these parts of the structure are a consequence of deficiencies in the modelling of the disorder, or absence of disorder models where disorder may be present. The heavily restrained models in these regions of the structure have been carefully examined to ensure that they represent the most chemically plausible ligand conformations considering knowledge of the composition and

overall connectivity of the supermolecule gleaned from synthetic knowledge and other analytical methods. Despite the ambiguity in the electron density map in these specific regions of the structure, the overall composition, topology, and geometry around metal centres can be very confidently concluded. For the ligands with poor atomic resolution mentioned above, detailed geometries of the naphthyl moieties including torsion angles and bonds distances are not sufficiently well-defined enough to be analysed.

Large regions of the structure both inside and outside the cage molecule contained diffuse electron density for which chemically sensible models could not be developed, hence, the Olex2 Solvent Mask routine was applied to the data. The contents of the masked regions were estimated to firstly contain the six tetrafluoroborate anions per symmetric unit necessary to balance the charge of the structure and secondly a mixture of the crystallisation solvents acetonitrile, dimethylsulfoxide and water sufficient to match the estimated electron count and void volume.

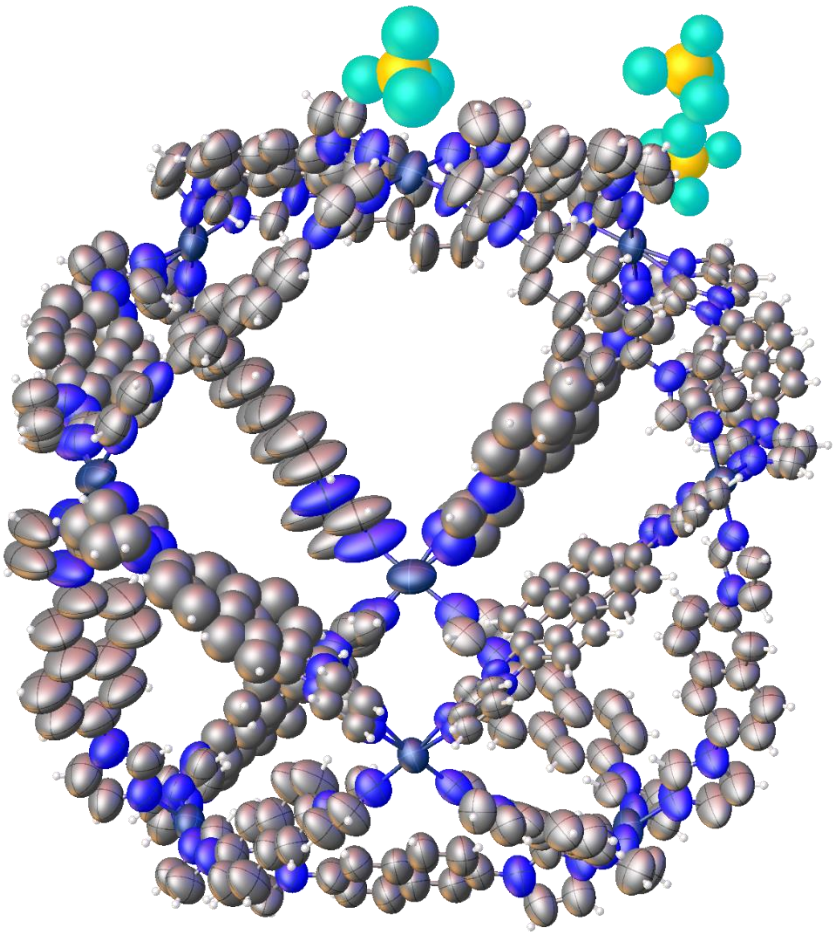

Figure S78: Image of **3** at 50% ellipsoids

S13.4 Single crystal structure of $Pd_6L^2_{12}$ octahedron 4

Single crystals of cage **4** were grown *via* slow vapour diffusion of *i*Pr_2O into a CD_3CN solution. A suitable crystal was selected and mounted using Fomblin (YR-1800 perfluoropolyether oil) on a Fluid Film Devices diffractometer. The crystal was kept at 100(2) K during data collection.

S13.4.1 Specific crystal structure and refinement details for 4

The crystal of a large supramolecular metal-organic cage complex diffracted moderately well. The synchrotron data used in the refinement was truncated to a diffraction resolution limit of 0.70 Å. This gave the refinement a data-parameter ratio of 29.3. Despite this high ratio, the large asymmetric unit required a large number of restraints and constraints to aid convergence of a chemically sensible model.

The geometries of all ligands were restrained to be similar (SAME). All tetrafluoroborate anions and acetonitrile solvent residues R, U, and W were restrained to have idealised target geometries using values from the Olex2 fragment database (DFIX). Rigid bond and similarity restraints were applied to the anisotropic displacement parameters of all atoms in the structure (RIGU, SIMU). The anisotropic displacement parameters of acetonitrile solvent residues R and W were restrained to have more isotropic character (ISOR).

Tetrafluoroborate anions I, L, and R were modelled with conformational disorder over two overlapping orientations respectively. The occupancies of the respective disorder components were refined and constrained to sum to unity giving values of 0.52(1), 0.52(1) and 0.55(1) respectively. The geometries of all the disordered tetrafluoroborate anions were refined with rigid idealised geometries with coordinates taken from the Olex2 FragmentDB tool (AFIX 6). All disordered tetrafluoroborate anions were refined with isotropic displacement parameters. The isotropic displacement parameters tetrafluoroborate anions I and Y were constrained to refine to a single variable value of 0.184 shared for all atoms. The occupancies of tetrafluoroborate anions J and M were refined resulting in values of 0.63(1) and 0.20(1) respectively.

Coordination cage ligand A was modelled with conformational disorder over two substantially overlapping orientations with the naphthyl ring moieties in different orientations. The occupancies of the conformations were refined and constrained to sum to unity resulting in a value of 0.63(5) for the major component. The anisotropic displacement parameters of the overlapping metal-coordinating nitrogen atoms N11A/X and N21A/X were constrained to be identical (EADP).

Hydrogen atoms were geometrically placed and refined with a riding model. The methyl hydrogen atoms for acetonitrile residues R and W could not be refined to convergence, likely

because of the large atomic displacement parameters of these atoms, and hence were not included in the model.

The large void regions were treated with the Olex2 solvent mask routine as no sensible models for the remaining electron density could be developed. The assumed contents of the masked region were assigned to contain 15 acetonitrile solvent residues per asymmetric unit as indicated by the electron count and void volume.

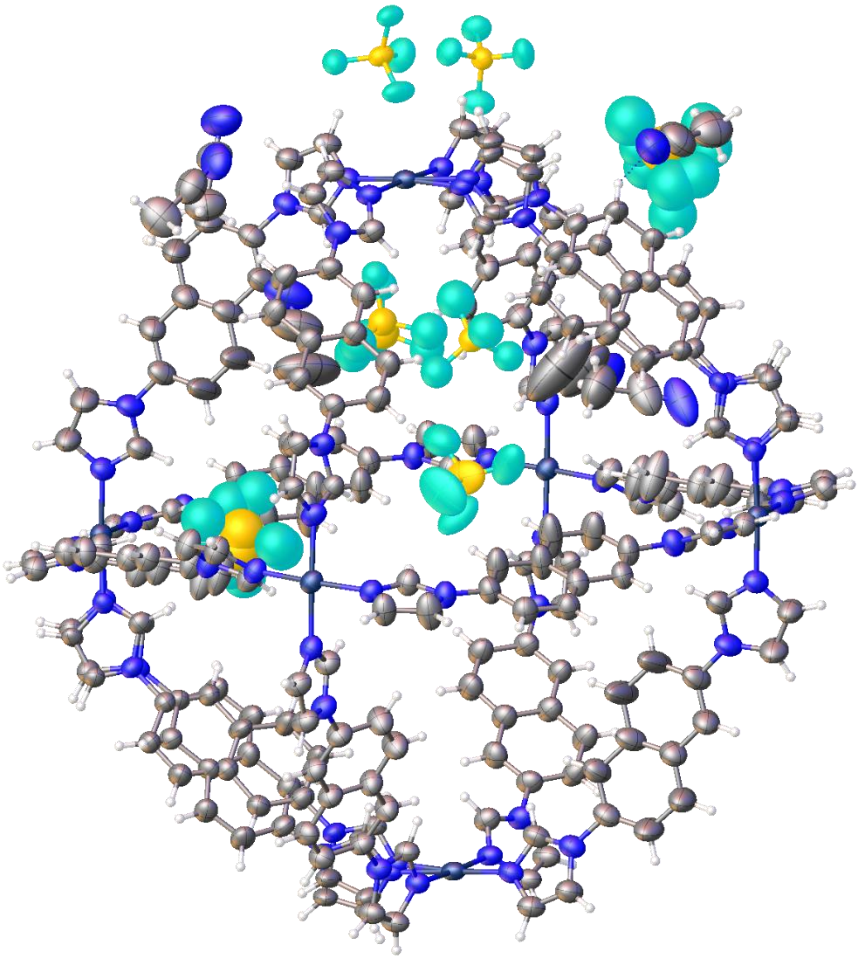

Figure S79: Image of **4** at 50% ellipsoids

S13.5 Single crystal structure of ligand L^1

Single crystals of ligand $\mathbf{L^1}$ were grown *via* vapour diffusion of hexane into CH_2Cl_2. A suitable crystal was selected and mounted using Fomblin (YR-1800 perfluoropolyether oil) on an Oxford Diffraction GV1000 (TitanS2 CCD area detector, mirror-monochromated Cu-K_α radiation source; λ = 1.54184 Å, ω scans). The crystal was kept at 120(2) K during data collection.

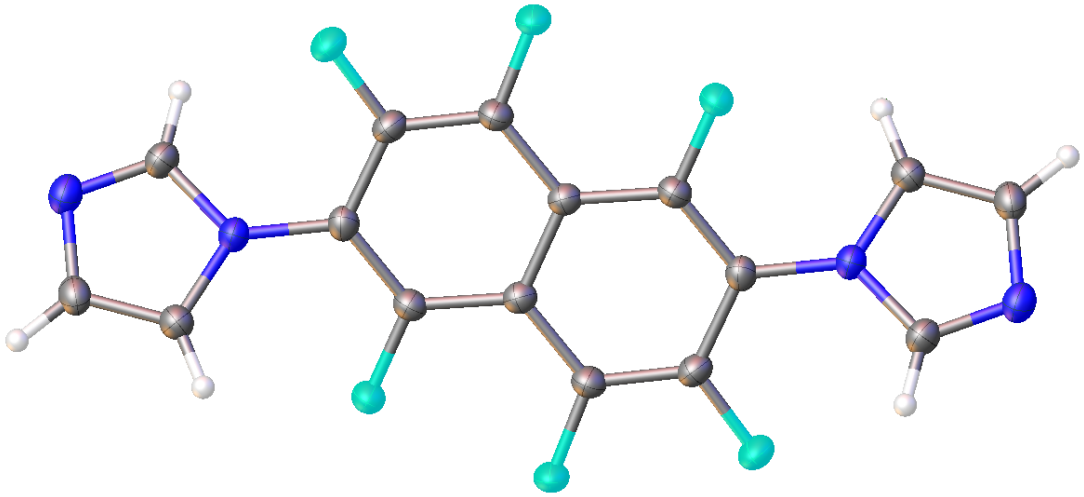

Figure S80: Image of $\mathbf{L^1}$ at 50% ellipsoids

S13.6 Single crystal structure of ligand L^2

Single crystals of ligand **L^2** were grown *via* cooling from hot CH_3CN solution. A suitable crystal was selected and mounted using Fomblin (YR-1800 perfluoropolyether oil) on an Oxford Diffraction GV1000 (TitanS2 CCD area detector, mirror-monochromated Cu-K_α radiation source; λ = 1.54184 Å, ω scans). The crystal was kept at 120(2) K during data collection.

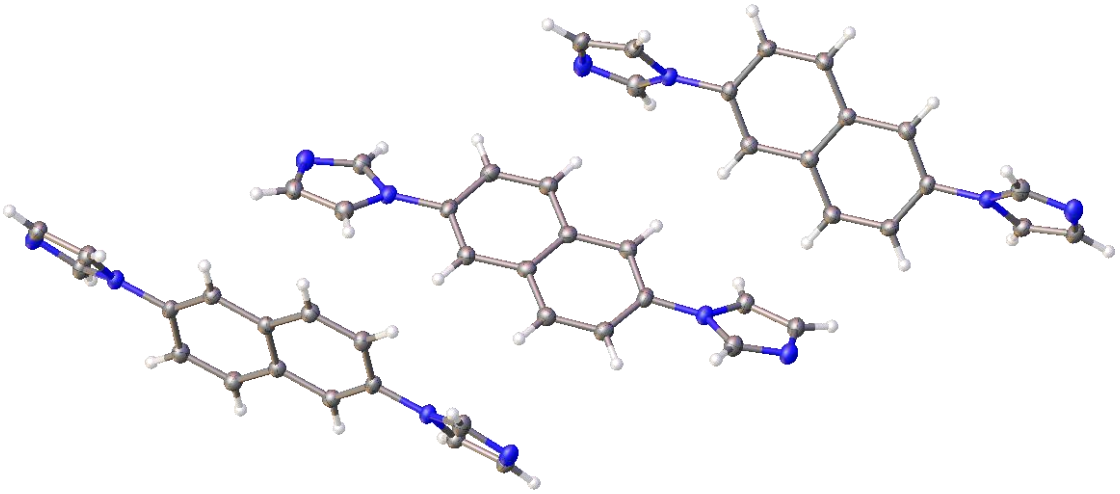

Figure S81: Image of **L^2** at 50% ellipsoids

S14 References

1 Fujii, S., Yamada, S., Matsumoto, S., Kubo, G., Yoshida, K., Tabata, E., Miyake, R., Sanada, Y., Akiba, I. & Okobira, T. Platonic micelles: monodisperse micelles with discrete aggregation numbers corresponding to regular polyhedra. *Sci. Rep.* **7**, 44494 (2017).

2 Bruinsma, R. F., Gelbart, W. M., Reguera, D., Rudnick, J. & Zandi, R. Viral self-assembly as a thermodynamic process. *Phys. Rev. Lett.* **90**, 248101 (2003).

3 Fujita, D., Yokoyama, H., Ueda, Y., Sato, S. & Fujita, M. Geometrically Restricted Intermediates in the Self-Assembly of an M12L24 Cuboctahedral Complex. *Angew. Chem.* **127**, 157-160 (2015).

4 Cohn, H. *Small spherical and projective codes*. Available at https://hdl.handle.net/1721.1/142661 (2022).

5 Hars, L. *Numerical solutions of the Tammes problem for up to 60 points*. Draft (2020). Available at https://www.hars.us/Papers/Numerical_Tammes.pdf (accessed 11 December 2025).

6 Sloane, N. J. A. *et al. Tables of Spherical Codes*. Available at http://neilsloane.com/packings/ (accessed 11 December 2025).

7 Abe, T., Takeuchi, K., Higashi, M., Sato, H. & Hiraoka, S. Rational design of metal–organic cages to increase the number of components via dihedral angle control. *Nat. Commun.* **15**, 7630 (2024).

8 Vasdev, R. A., Findlay, J. A., Turner, D. R. & Crowley, J. D. Self-Assembly of a Redox Active, Metallosupramolecular [Pd3L6] 6+ Complex Using a Rotationally Flexible Ferrocene Ligand. *Chem. Asian J.* **16**, 39-43 (2021).

9 Preston, D., Lewis, J. E. M. & Crowley, J. D. Multicavity [PdnL4]2n+ Cages with Controlled Segregated Binding of Different Guests. *J. Am. Chem. Soc.* **139**, 2379-2386 (2017).

10 Preston, D., White, K. F., Lewis, J. E., Vasdev, R. A., Abrahams, B. F. & Crowley, J. D. Solid-State Gas Adsorption Studies with Discrete Palladium (II)[Pd2 (L) 4] 4+ Cages. *Chem. Eur. J.* **23**, 10559-10567 (2017).

11 Walther, A., Regeni, I., Holstein, J. J. & Clever, G. H. Guest-Induced Reversible Transformation between an Azulene-Based Pd2L4 Lantern-Shaped Cage and a Pd4L8 Tetrahedron. *J. Am. Chem. Soc.* **145**, 25365-25371 (2023).

12 Black, M. R., Bhattacharyya, S., Argent, S. P. & Pilgrim, B. S. Structural Transformations of Metal–Organic Cages through Tetrazine-Alkene Reactivity. *J. Am. Chem. Soc.* **146**, 28233-28241 (2024).

13 Ganta, S. & Chand, D. K. Molecular Recombination Phenomena in Palladium(II)-Based Self-Assembled Complexes. *Inorg. Chem.* **57**, 5145-5158 (2018).

14 Samanta, D. & Mukherjee, P. S. Component Selection in the Self-Assembly of Palladium (II) Nanocages and Cage-to-Cage Transformations. *Chem. Eur. J.* **20**, 12483-12492 (2014).

15 Samanta, D., Chowdhury, A. & Mukherjee, P. S. Covalent Postassembly Modification and Water Adsorption of Pd3 Self-Assembled Trinuclear Barrels. *Inorg. Chem.* **55**, 1562-1568 (2016).

16 Wu, M.-X., Hong, Q.-Y., Li, M., Jiang, W.-L., Huang, B., Lu, S., Wang, H., Yang, H.-B., Zhao, X.-L. & Shi, X. Self-assembly of conformation-adaptive dihydrophenazine-based coordination cages. *Chem. Commun.* **60**, 1184-1187 (2024).

17 Chu, D., Gong, W., Jiang, H., Tang, X., Cui, Y. & Liu, Y. Boosting enantioselectivity of chiral molecular catalysts with supramolecular metal–organic cages. *CCS Chem.* **4**, 1180-1189 (2022).

18 Tessarolo, J., Lee, H., Sakuda, E., Umakoshi, K. & Clever, G. H. Integrative Assembly of Heteroleptic Tetrahedra Controlled by Backbone Steric Bulk. *J. Am. Chem. Soc.* **143**, 6339-6344 (2021).

19 Zhang, T., Zhou, L.-P., Guo, X.-Q., Cai, L.-X. & Sun, Q.-F. Adaptive self-assembly and induced-fit transformations of anion-binding metal-organic macrocycles. *Nat. Commun.* **8**, 15898 (2017).
20 Chand, D. K., Biradha, K., Kawano, M., Sakamoto, S., Yamaguchi, K. & Fujita, M. Dynamic Self-Assembly of an M3L6 Molecular Triangle and an M4L8 Tetrahedron from Naked PdII Ions and Bis(3-pyridyl)-Substituted Arenes. *Chem. Asian J.* **1**, 82-90 (2006).
21 Suzuki, K., Tominaga, M., Kawano, M. & Fujita, M. Self-assembly of an M6L12 coordination cube. *Chem. Commun.*, 1638-1640 (2009).
22 Saha, R., Ghosh, A. K., Samajdar, R. N. & Mukherjee, P. S. Self-Assembled PdII6 Molecular Spheroids and Their Proton Conduction Property. *Inorg. Chem.* **57**, 6540-6548 (2018).
23 Bhattacharyya, S., Argent, S. P. & Pilgrim, B. S. Fluorinated Twists: A Pathway to a Stable Pd8L16 Square Antiprism. *J. Am. Chem. Soc.* **147**, 30296-30303 (2025).
24 de Montmollin, J., Fadaei-Tirani, F. & Severin, K. Wide variability in the stability of Pd 6 L x-type coordination cages. *Dalton Trans.* **54**, 15773-15779 (2025).
25 Tominaga, M., Suzuki, K., Kawano, M., Kusukawa, T., Ozeki, T., Sakamoto, S., Yamaguchi, K. & Fujita, M. Finite, spherical coordination networks that self-organize from 36 small components. *Angew Chem. Int. Ed.* **43**, 5621-5625 (2004).
26 Harris, K., Sun, Q.-F., Sato, S. & Fujita, M. M12L24 Spheres with Endo and Exo Coordination Sites: Scaffolds for Non-Covalent Functionalization. *J. Am. Chem. Soc.* **135**, 12497-12499 (2013).
27 Yokoyama, H., Ueda, Y., Fujita, D., Sato, S. & Fujita, M. Finely Resolved Threshold for the Sharp M12L24/M24L48 Structural Switch in Multi-Component MnL2n Polyhedral Assemblies: X-ray, MS, NMR, and Ultracentrifugation Analyses. *Chem. Asian J.* **10**, 2292-2295 (2015).
28 Sun, Q.-F., Iwasa, J., Ogawa, D., Ishido, Y., Sato, S., Ozeki, T., Sei, Y., Yamaguchi, K. & Fujita, M. Self-assembled M24L48 polyhedra and their sharp structural switch upon subtle ligand variation. *Science* **328**, 1144-1147 (2010).
29 Bunzen, J., Iwasa, J., Bonakdarzadeh, P., Numata, E., Rissanen, K., Sato, S. & Fujita, M. Self-assembly of M24L48 polyhedra based on empirical prediction. *Angew Chem. Int. Ed.* **51**, 3161-3163 (2012).
30 Fujita, D., Ueda, Y., Sato, S., Yokoyama, H., Mizuno, N., Kumasaka, T. & Fujita, M. Self-Assembly of $M_{30}L_{60}$ Icosidodecahedron. *Chem.* **1**, 91-101 (2016).
31 Martí-Centelles, V., Piskorz, T. K. & Duarte, F. CageCavityCalc (C 3): a computational tool for calculating and visualizing cavities in molecular cages. *J. Chem. Inf. Model.* **64**, 5604-5616 (2024).
32 Cosier, J. t. & Glazer, A. A nitrogen-gas-stream cryostat for general X-ray diffraction studies. *J. Appl. Crystallogr.* **19**, 105-107 (1986).
33 Rigaku Corporation. *CrysAlisPro* software system, version 1.171.40.45a. Available at https://rigaku.com/products/crystallography/x-ray-diffraction/crysalispro (2021).
34 Allan, D. R., Nowell, H., Barnett, S. A., Warren, M. R., Wilcox, A., Christensen, J., Saunders, L. K., Peach, A., Hooper, M. T. & Zaja, L. A novel dual air-bearing fixed-χ diffractometer for small-molecule single-crystal X-ray diffraction on beamline I19 at Diamond Light Source. *Crystals* **7**, 336 (2017).
35 Winter, G. xia2: an expert system for macromolecular crystallography data reduction. *J. Appl. Crystallogr.* **43**, 186-190 (2010).
36 Dolomanov, O. V., Bourhis, L. J., Gildea, R. J., Howard, J. A. & Puschmann, H. OLEX2: a complete structure solution, refinement and analysis program. *J. Appl. Crystallogr.* **42**, 339-341 (2009).
37 Sheldrick, G. SHELXT - Integrated space-group and crystal-structure determination. *Acta Cryst. A* **71**, 3-8 (2015).
38 Sheldrick, G. Crystal structure refinement with SHELXL. *Acta Cryst. C* **71**, 3-8 (2015).
39 International Union of Crystallography. *checkCIF*. Available at https://checkcif.iucr.org/

40 Global Phasing Ltd. *Grade2* version 1.7.1 (2021). Available at https://www.globalphasing.com/grade/